

# **Synthetic jet with piezoelectric flaps mechanism for enhancement of heat transfer performance and energy harvesting**

**M. Tech. Thesis**

By  
**Dinesh**



**DEPARTMENT OF MECHANICAL ENGINEERING  
INDIAN INSTITUTE OF TECHNOLOGY INDORE  
MAY 2024**



# **Synthetic jet with piezoelectric flaps mechanism for enhancement of heat transfer performance and energy harvesting**

**A THESIS**

*Submitted in partial fulfillment of the  
requirements for the award of the degree  
of  
Master of Technology*

*by*

**Dinesh**



**DEPARTMENT OF MECHANICAL ENGINEERING  
INDIAN INSTITUTE OF TECHNOLOGY INDORE  
MAY 2024**



# INDIAN INSTITUTE OF TECHNOLOGY INDORE

## CANDIDATE'S DECLARATION

I hereby certify that the work which is being presented in the thesis entitled **Synthetic jet with piezoelectric flaps mechanism for enhancement of heat transfer performance and energy harvesting** in the partial fulfilment of the requirements for the award of the degree of **MASTER OF TECHNOLOGY** in **Thermal Energy System** and submitted in the **DEPARTMENT OF MECHANICAL ENGINEERING Indian Institute of Technology Indore** is an authentic record of my own work carried out during the time period from July 2022 to May 2024 under the supervision of Dr. Harekrishna Yadav, Assistance Professor, and Dr. Satyanarayan Patel, Associate Professor, Department of Mechanical Engineering, IIT Indore.

The matter presented in this thesis has not been submitted by me for the award of any other degree of this or any other institute.

Signature of the student with date

**Dinesh, (04/06/2024)**

-----  
This is to certify that the above statement made by the candidate is correct to the best of my/our knowledge.

Signature of the Supervisor of  
M.Tech. thesis #1 (with date)

**(Dr. Harekrishna Yadav)**

04/06/2024

Signature of the Supervisor of  
M.Tech. thesis #2 (with date)

**(Dr. Satyanarayan Patel)**

04/06/2024

-----  
**Dinesh** has successfully given his/her M.Tech. Oral Examination held on **<Date of M.Tech. Oral Examination>**.

Signature(s) of Supervisor(s) of M.Tech. thesis

Date: 04/06/2024

Signature(s) of Supervisor(s) of M.Tech. thesis

Date: 04/06/2024

Convener, DPGC

Date: 05/06/2024

## ACKNOWLEDGEMENT

I want to express my deepest gratitude to my supervisor **Dr. Harekrishna Yadav** and co-supervisor **Dr. Satyanarayan Patel**, Department of Mechanical Engineering, Indian Institute of Technology (IIT) Indore, for their invaluable guidance, encouragement, and unwavering support throughout the entire project process. I have been fortunate to have supervisors who cared about my work and promptly responded to questions and queries. Their expertise and insightful suggestions have been instrumental in shaping this thesis.

My heartfelt gratitude to my seniors, lab mates, and colleague researchers, especially **Mr. Dnyanesh Mirikar, Mr. Nishchay Saurabh, Mr. Rajat Kumar, Mr. Nitin, Mr. Zen Kapadiya, Mr. Arbaz Sheikh, Mr. Chakradhar Reddy** for their cooperation and stay to make M.Tech. project journey happy and joyful.

I am indebted to my family for their constant love, understanding, and encouragement. Their unwavering belief in my abilities has been my greatest motivation.

Finally, I am thankful to all who directly or indirectly contributed, helped, and supported me.

**Dinesh**

## ABSTRACT

The conventional synthetic jet's inferior thermal performance limits its applicability in confined space thermal management. The present study proposes a novel design incorporating external mechanisms that contain stainless steel flaps over which piezoelectric discs are pasted. These vibrate through flow motion piezoelectric flaps opposite each other in addition to the acoustically actuated synthetic jet. Placing piezoelectric (PZT) material on stainless steel flaps allows energy harvesting from the impinging synthetic jet's flow-induced vibrations. The synthetic jet operates at a frequency of 31 Hz and amplitude of 10 V, corresponding to a Reynolds number of 13000 and a stroke length of 16.2. The effect on the heat transfer characteristics is analyzed for placement of the flaps at different locations along and away from the jet centreline. Results reveal up to a 46% enhancement in the area-averaged Nusselt number. Optimal heat transfer conditions are observed at lower orifice-to-surface ( $z/d$ ) and flap-to-surface ( $s/d$ ) values. This enhancement is attributed to improved mixing between the flaps and the heated surface, boosting convective heat transfer and reducing recirculated heated air toward the orifice. Notably, higher heat transfer enhancements are observed when  $s/d$  values are lower ( $<2$ ). Moreover, piezoelectric flaps enable energy harvesting from flow-induced vibrations, with a maximum power conversion of 195 mW per flap, equivalent to 2.20 % of the power supplied to actuate the synthetic jet. Therefore, the proposed synthetic jet design improves thermal performance and conserves energy induced by the synthetic jet, making it an effective thermal management technique.

**Keywords:** Synthetic jet, thermal management, piezoelectric, PZT, energy harvesting

# TABLE OF CONTENT

	Page No.
<b>ACKNOWLEDGEMENT</b>	iii
<b>ABSTRACT</b>	iv
<b>TABLE OF CONTENT</b>	v
<b>LIST OF FIGURES</b>	vii
<b>LIST OF TABLES</b>	x
<b>NOMENCLATURE &amp; ABBREVIATIONS</b>	xi
<b>Chapter 1 Introduction</b>	1
1.1 Electronic cooling	1
1.1.1. Synthetic jet impingement.	1
1.1.2. Synthetic jet parameters.	3
1.1.3. Applications of synthetic jet.	4
1.2. Introduction of aeroelastic energy harvesting	6
1.2.1. Piezoelectric materials	8
1.2.2. Applications of Piezoelectric materials.	8
<b>Chapter 2 Literature review and problem formulation</b>	11
2.1. Literature review of synthetic jet impingement.	11
2.2. Literature review of aeroelastic energy harvesting.	15
2.3. Gaps in literature and problem formulation.	19
<b>Chapter 3 Experimental Methodology</b>	21
3.1 Experimental setup	21
3.2. Validation of the measurement techniques	25
<b>Chapter 4 Result and Discussions</b>	27
4.1. Heat transfer performance.	27
4.1.1. The conventional synthetic jet.	27
4.1.2. The synthetic jet with two piezoelectric flaps.	29
4.1.3 The synthetic jet with four piezoelectric flaps	39
4.1.4. Nu contours.	41
4.2. Energy harvesting using synthetic jet with piezoelectric flaps.	46
4.2.1 Effect of the resistance for the voltage ( $V_{rms}$ ) measurement.	46
4.2.2 Effect of the orifice-to-flap spacing ( $h/d$ ) on the voltage ( $V_{rms}$ ) measurement.	47

4.2.3 Effect of the radial location (R) on the voltage ( $V_{rms}$ ) measurement	48
4.2.4. Effect of the supplied voltage to the synthetic jet actuator on the voltage ( $V_{rms}$ ) measurement	50
<b>5. Conclusions and Scope for Future Work</b>	<b>53</b>
5.1 Conclusions	53
5.2 Scope for Future Work	54
<b>References</b>	<b>55</b>

## LIST OF FIGURES

<b>Fig. No.</b>	<b>Figure Captions</b>	<b>Page No</b>
1.1	Block diagram of SJ	3
1.2	SJ parameters [8-10]	4
1.3	Use of SJ in de-icing over an aerofoil.[11]	5
1.4	Application of SJ for flow separation control [12]	5
1.5	Application of SJ in electronic cooling [13]	6
1.6	Block Diagram of Aeroelastic Energy Harvesting	7
1.7	Mechanism of Aeroelastic Energy	7
1.8	A piezoelectric sensor detects the vibrations of the train wheel [17]	9
1.9	(a) Simultaneous measurement using a flexible sensor and ultrasonic probe, (b) Blood pressure measurement overview.[18]	9
1.10	Aeroelastic energy harvesting from D-section structure [19]	10
1.11	Piezoelectric energy harvesting from the human heart.[20]	10
2.1	Variation of Nu to the dimensionless ratio of the distance of the heated surface from orifice-to-orifice diameter [27]	11
2.2	Variation in heat transfer coefficient to (a) cavity height and (b) orifice thickness [30]	12
2.3	Variation in Nu with axial distance number for different shapes of orifice [33]	13
2.4	Variation of average Nu with axial distance for a multiple orifice [34]	14
2.5	Fluid flow behavior of coaxial SJ orifice [40]	15
2.6	Aeroelastic energy harvesting by using vibration generated by aerofoil (flutter) [43]	16
2.7	Aeroelastic energy harvesting from HVAC duct.[44]	16
2.8	Piezoelectric energy harvesting from raindrops [30]	17
2.9	Mechanism and application of aeroelastic energy harvesting [53]	18
2.1	Jet cooling	19
2.11	Aeroelastic Energy harvesting	20
3.1	Experimental setup.	21
3.2	(a) Front, (b) Top and (c) 3D Experimental setup visualization with two flaps.	22
3.3	(a) Front and (b) 3D Experimental setup visualization with four strips.	23
3.4	Three different types of flaps were used in the experiments.	23

3.5	Validation of heat transfer measurement technique in the present experimental setup spacings for steady jet impingement with Lee and Lee (a) average Nu and (b) local Nu at $r/d=6$ [60]	24
3.6	Validation of heat transfer measurement technique in the present experimental setup spacings for synthetic jet impingement with Greco <i>et al.</i> [57]	24
4.1	Conventional SJ area-averaged heat transfer over different surface areas at various axial distances.	28
4.2	Heat transfer performance (wide area cooling, $r/d=4$ ) of the steady jet vs. SJ at various $z/d$ values	28
4.3	Heat transfer rates of the SJ with piezoelectric flaps at different combinations of $z/d$ and $h/d$ value for W8 two strips at radial location R5 (a) $Nu_{avg}$ at spot cooling circle of 40mm dia. ( $r/d-1$ ), (b) % enhancement in $Nu_{avg}$ at ( $r/d-1$ ) as compared to conventional SJ, (c) $Nu_{avg}$ at wide area cooling circle 160 mm dia. ( $r/d-4$ ), (d) % enhancement in $Nu_{avg}$ at ( $r/d-4$ ) compared to conventional SJ	30
4.4	Heat transfer rates of the SJ with piezoelectric flaps at different combinations of $z/d$ and $h/d$ value for W8 two strips at radial location R3.5 (a) $Nu_{avg}$ at spot cooling circle of 40mm dia. ( $r/d-1$ ), (b) % enhancement in $Nu_{avg}$ at ( $r/d-1$ ) as compared to conventional SJ, (c) $Nu_{avg}$ at wide area cooling circle 160 mm dia. ( $r/d-4$ ), (d) % enhancement in $Nu_{avg}$ at ( $r/d-4$ ) compared to conventional SJ	32
4.5	Heat transfer rates of the SJ with piezoelectric flaps at different combinations of $z/d$ and $h/d$ value for W8 two strips at radial location R3.5 (a) $Nu_{avg}$ at spot cooling circle of 40mm dia. ( $r/d-1$ ), (b) % enhancement in $Nu_{avg}$ at ( $r/d-1$ ) as compared to conventional SJ, (c) $Nu_{avg}$ at wide area cooling circle 160 mm dia. ( $r/d-4$ ), (d) % enhancement in $Nu_{avg}$ at ( $r/d-4$ ) compared to conventional SJ	33
4.6	Heat transfer rates of the SJ with piezoelectric flaps at different combinations of $z/d$ and $h/d$ value for W4 two strips at radial location R2 (a) $Nu_{avg}$ at spot cooling circle of 40mm dia. ( $r/d-1$ ), (b) % enhancement in $Nu_{avg}$ at ( $r/d-1$ ) as compared to conventional SJ, (c) $Nu_{avg}$ at wide area cooling circle 160 mm dia. ( $r/d-4$ ), (d) % enhancement in $Nu_{avg}$ at ( $r/d-4$ ) compared to conventional SJ	35
4.7	Heat transfer rates of the SJ with piezoelectric flaps at different combinations of $z/d$ and $h/d$ value for W4 two strips at radial location R5 (a) $Nu_{avg}$ at spot cooling circle of 40mm dia. ( $r/d-1$ ), (b) % enhancement in $Nu_{avg}$ at ( $r/d-1$ ) as compared to conventional SJ, (c) $Nu_{avg}$ at wide area cooling circle 160 mm dia. ( $r/d-4$ ), (d) % enhancement in $Nu_{avg}$ at ( $r/d-4$ ) compared to conventional SJ	36
4.8	Heat transfer rates of the SJ with piezoelectric flaps at different combinations of $z/d$ and $h/d$ value for W12 two strips at radial location R5 (a) $Nu_{avg}$ at spot cooling circle of 40mm dia. ( $r/d-1$ ), (b) %	37

	enhancement in $Nu_{avg}$ at (r/d-1) as compared to conventional SJ, (c) $Nu_{avg}$ at wide area cooling circle 160 mm dia. (r/d-4), (d) % enhancement in $Nu_{avg}$ at (r/d-4) compared to conventional SJ	
4.9	Heat transfer rates of the SJ with piezoelectric flaps at different combinations of z/d and h/d value for W12 two strips at radial location R2 (a) $Nu_{avg}$ at spot cooling circle of 40mm dia. (r/d-1), (b) % enhancement in $Nu_{avg}$ at (r/d-1) as compared to conventional SJ, (c) $Nu_{avg}$ at wide area cooling circle 160 mm dia. (r/d-4), (d) % enhancement in $Nu_{avg}$ at (r/d-4) compared to conventional SJ	38
4.10	Heat transfer rates of the SJ with piezoelectric flaps at different combinations of z/d and h/d value for W8 four strips at radial location R5 (a) $Nu_{avg}$ at spot cooling circle of 40mm dia. (r/d-1), (b) % enhancement in $Nu_{avg}$ at (r/d-1) as compared to conventional SJ, (c) $Nu_{avg}$ at wide area cooling circle 160 mm dia. (r/d-4), (d) % enhancement in $Nu_{avg}$ at (r/d-4) compared to conventional SJ	39
4.11	Heat transfer rates of the SJ with piezoelectric flaps at different combinations of z/d and h/d value for W4 for strips at radial location R5 (a) $Nu_{avg}$ at spot cooling circle of 40mm dia. (r/d-1), (b) % enhancement in $Nu_{avg}$ at (r/d-1) as compared to conventional SJ, (c) $Nu_{avg}$ at wide area cooling circle 160 mm dia. (r/d-4), (d) % enhancement in $Nu_{avg}$ at (r/d-4) compared to conventional SJ	40
4.12	Orifice and flap (width, w=8 mm) configurations used in the current set of experiments	41
4.13	$Nu$ contours at h/d=1.5, z/d=3	42
4.14	$Nu$ contours at z/d=5	43
4.15	$Nu$ contours at z/d=7	44
4.16	$Nu$ contours at z/d=10	45
4.17	Heat transfer visualization through $Nu$ contour for different configurations at z/d-3, h/d-2 (a) without strip SJ (b) SJ with two flaps W8R5 and (c) SJ with four flaps W8R5.	46
4.18	Effect of the voltage generated from a single piezoelectric flap for different values of resistances	47
4.19	Voltage signals acquired from a piezoelectric flap at different orifice-to-flap spacings	48
4.20	Voltage, power generated, and the % of energy harvested from a single piezoelectric flap at h/d=1.5 for three radial locations of the flap	49
4.21	Effect of the input power supplied to the acoustic synthetic jet (amplitude) on the voltage generated by a single piezoelectric flap	51
4.22	A comparative analysis of voltage, power, and % energy harvested for different types of strips at all radial locations. (a) variation in $v_{rms}$ to h/d for all strips (b) variation in power to h/d for all strips (c) variation in % energy harvesting to h/d for all strips	52

## **LIST OF TABLES**

Table 3.1 Experimental uncertainties estimated in the current set of experiments	29
--	----

## NOMENCLATURE & ABBREVIATIONS

$d$	Diameter of center orifice (mm)
$h$	Distance between the orifice and piezoelectric flaps.
$f$	Diaphragm oscillation frequency (Hz)
$H$	Cavity depth (mm)
$R$	The radial distance of flap end width to the jet centerline
$S$	Distance between piezoelectric flaps and heated surface
$W$	Strip end width in (mm)
$z$	Axial distance between the heated surface and orifice plate (mm)
$z/d$	Normalized axial distance.
$r/d$	Dimensionless ratio of radius of surface cooled to orifice diameter
$T$	Period of diaphragm oscillation cycle (s)
$t$	Time (s)
$U_o$	Time-averaged jet-blowing velocity over the entire cycle (m/s)
$u$	Instantaneous jet exit velocity (m/s)
$x$	Axial coordinate measured from the orifice exit (mm)
$\nu$	Molecular kinematic viscosity (m <sup>2</sup> /s)
$T_s$	Surface temperature (°C)
$T_a$	Ambient temperature (°C)
$Nu_{avg}$	Average Nusselt number
CJ	Continuous jet
SJ	Synthetic jet
SJA	Synthetic jet actuator
HWA	Hot wire anemometer
PZT	Lead Zirconate Titanate



---

## **Introduction**

---

### **1.1 Electronic cooling**

The electronic cooling methodology is essential for maintaining the optimum temperature range for electronic components and devices. This is because electronic devices contain many resistors and transistors, generating much heat. This excessive heat generation, premature failure, and temperature fluctuations can lead to degradation in an electronic component and affect the system's reliability. The electronic chip performance decreases by 4% with a 1°C rise in temperature, and temperature changes from 10° to 20° cause electronic chip failure [1]. Electronic cooling provides numerous benefits for maximizing electronic devices' performance, reliability, and efficiency across various industries and applications. Effective cooling technology is indispensable in ensuring the optimal operation of electronic systems, from preventing damage to extending lifespan and improving energy efficiency.

Traditional cooling systems include (i) Thermosyphons- a passive heat transfer cooling technology where heat transfer occurs due to natural convection or phase change [2]. (ii) Heat pipes – consist of low boiling point working fluid that takes heat from a system and evaporates, producing cooling [3]. (iii) Electro-osmotic pump- Electro-osmotic pump devices utilize an electric field to drive the flow of liquids through porous media, such as porous membranes or microchannels [4]. (iv) Thermoelectric cooler- It worked on the Peltier effect where two dissimilar metals are joined together and current flows in a circuit; one side of the junction loses heat, and the other absorbs heat. It can effectively be used in electronic cooling [5]. (v) Jet impingement cooling for electronic devices directs a high-velocity jet of coolant fluid, such as air or mist, onto the surface of the electronic component to remove heat efficiently. A fluid jet may be steady or unsteady; an unsteady jet may be pulsating and a synthetic jet (SJ). Several studies are being done on SJs to enhance their performance at lower surface spacing. Thus, the present work aims to enhance SJ performance at lower surface spacing and harvest some power.

#### **1.1.1. Synthetic jet (SJ) impingement**

The jet impingement technique is known for its high heat transfer because of its advantages over conventional free convection heat transfer. It allows a higher heat transfer coefficient and uniform heat transfer across the surface. Further, controlled heat transfer can be

achieved by varying fluidic parameters such as jet velocity, fluid temperature and jet diameter [6]. A SJ is a net zero mass flux device with many advantages compared to steady jet impingement. It consumes less power, is compact in design, is lightweight, operates at a high modulated frequency, and quickly responds to a load change [7]. A SJ is a fluidic device that produces a pulsating jet using oscillating motion induced by the (i) piezoelectric or electromagnetic actuator. An important part of a SJ is the piezoelectric actuator. It deforms under the application of voltage, and a thin diaphragm or electromagnetic actuator magnifies its deformation and uses electromagnetic force to deflect the diaphragm, which is generated by a coil of wire and magnetic material. The actuating diaphragm is used to actuate fluid, and piezoelectric or electromagnetic actuators deflect the diaphragm. (ii) Cavity – it behaves like a cylinder of an IC engine for fluid storage during suction stroke and (iii) an orifice plate to produce a jet from the cavity. (iv) Control system- it regulates the operation of an actuator, such as amplitude and frequency. The heart of a SJ is an oscillating diaphragm that is actuated by an electric signal and during a diaphragm expansion. The actuator increases the volume of the cavity and creates low pressure, causing fluid to be drawn from the surroundings through the orifice. In the contraction phase, the actuator reverses its direction, decreasing the diaphragm volume. This contraction phase increases pressure inside the cavity, causing the fluid to come through the orifice to form a jet of fluid. The cycle occurs continuously throughout the operation. Therefore, their compact designs make SJs more advantageous than steady jets. SJ does not require any fan, compressor, or piping system for its operation, which means it has reduced mechanical complexity and lower maintenance requirements, potentially a longer lifetime. SJ can be dynamically controlled by just controlling amplitude and frequency with low energy consumption compared to conventional fluidic devices.

Fig. 1.1 shows different SJ parts. The outlet flow is divided into three different regions based on flow behaviours. The first region is a near field; this region occurs in the initial phase of the SJ flow cycle when fluid is ejected from an orifice. As the jet expands and propagates outward from the orifice, it entrains surrounding fluid in a flow field. This entrainment causes the jet to entrain surrounding fluid, decreasing heat transfer. The second region is the transition region; the SJ reaches its maximum displacement, fluid starts decelerating, and vortices begin forming from the jet's edge. These vortices are formed due to the shear stress between the jet and ambient fluid. A vortex shed also forms in this region,

enhancing mixing and entrainment. Therefore, maximum heat transfer occurs in this region.

The third is a far-field region where vortices vanish into a surrounding fluid.

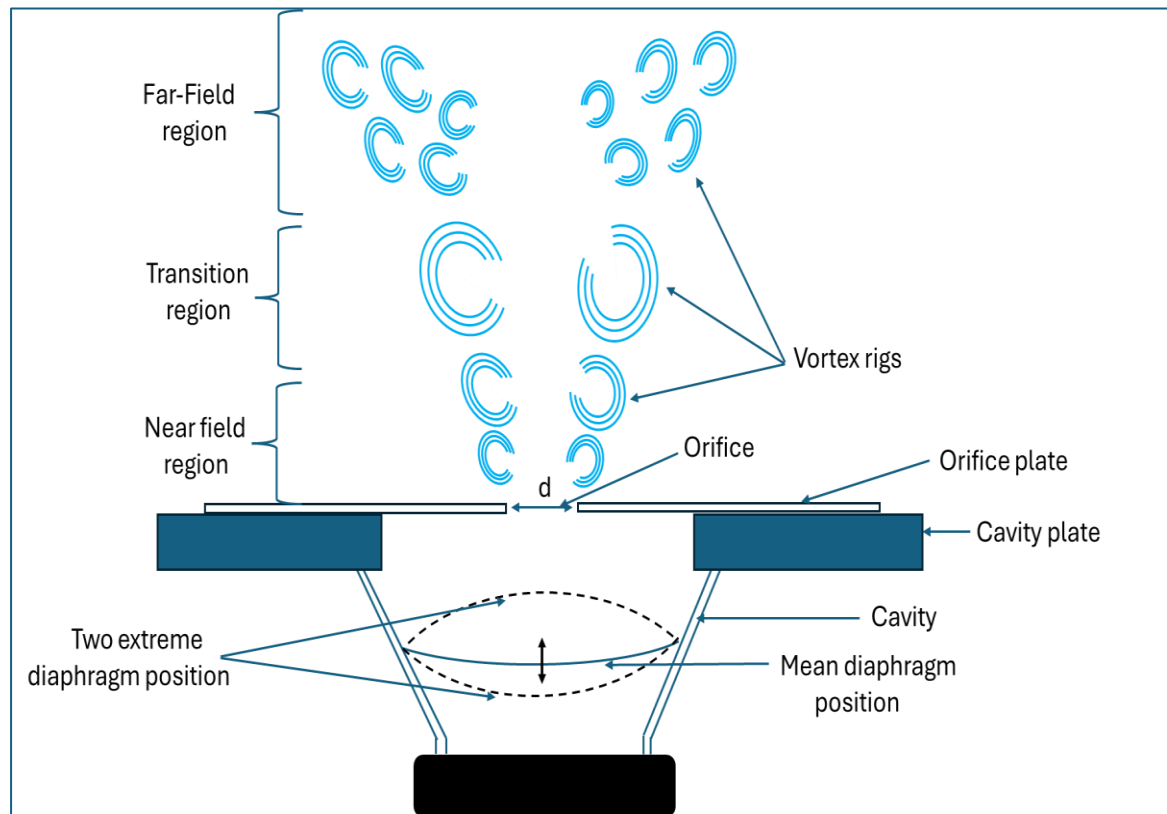


Fig. 1.1 Block diagram of SJ.

### 1.1.2. SJ parameters

A SJ parameter is crucial for optimization and performance enhancement for specific applications such as boundary layer control, fluid mixing, and flow separation control. SJ parameters are classified into actuation, geometric and fluidic. Fig. 1.2 depicted actuation parameters as frequency, which shows how fast fluid is sucked and ejected back into the surrounding, and amplitude controls the intensity of the jet. The geometric parameter is the orifice through fluid ejected and sucked. It governs the velocity profile, flow rate magnitude and direction of the jet; cavity height shows the capacity of the actuator. Fluidic parameters like temperature, mean velocity, and kinematic viscosity affect heat transfer.

### 1.1.3. Applications of SJ

SJs have a variety of applications across different areas due to their ability to produce controlled fluid flow without mechanical components like a fan or compressor. It is lightweight and cost-effective as compared to other technologies.

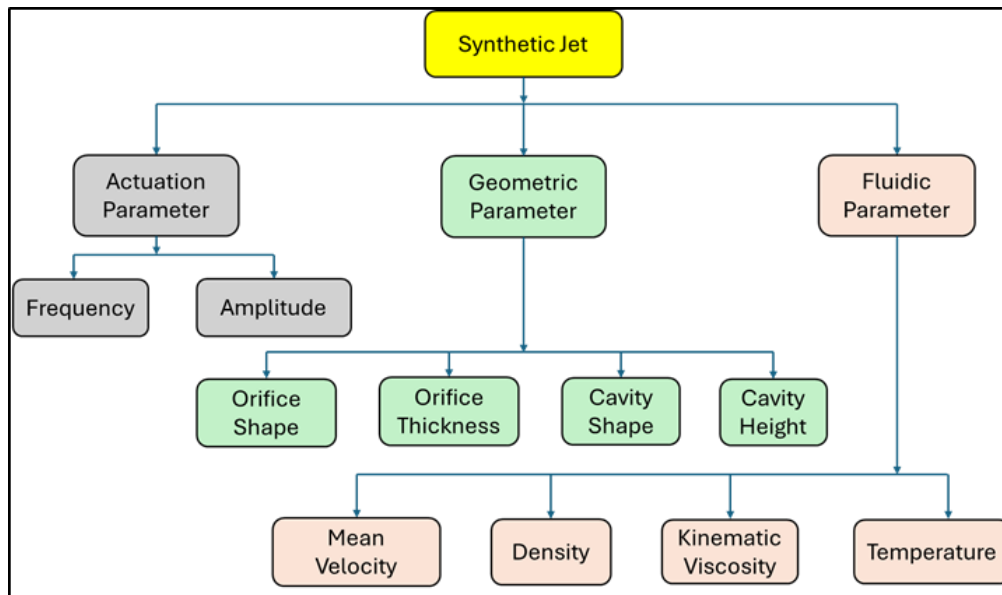


Fig. 1.2: SJ parameters [8-10].

**De-Icing over an aerofoil:** Recently, a novel SJ was introduced to remove ice from an aerofoil. With increased height from the earth's surface, temperature starts decreasing in the troposphere; when aircraft fly into this region, ice formation is possible over its aerofoil, affecting aircraft performance. This ice is continuously removed through an electrical supply. Fig. 1.3 shows the use of a SJ in a de-icing over an aerofoil. Conventionally, an electrical heater was used to de-ice over aerofoils, which consume high power.

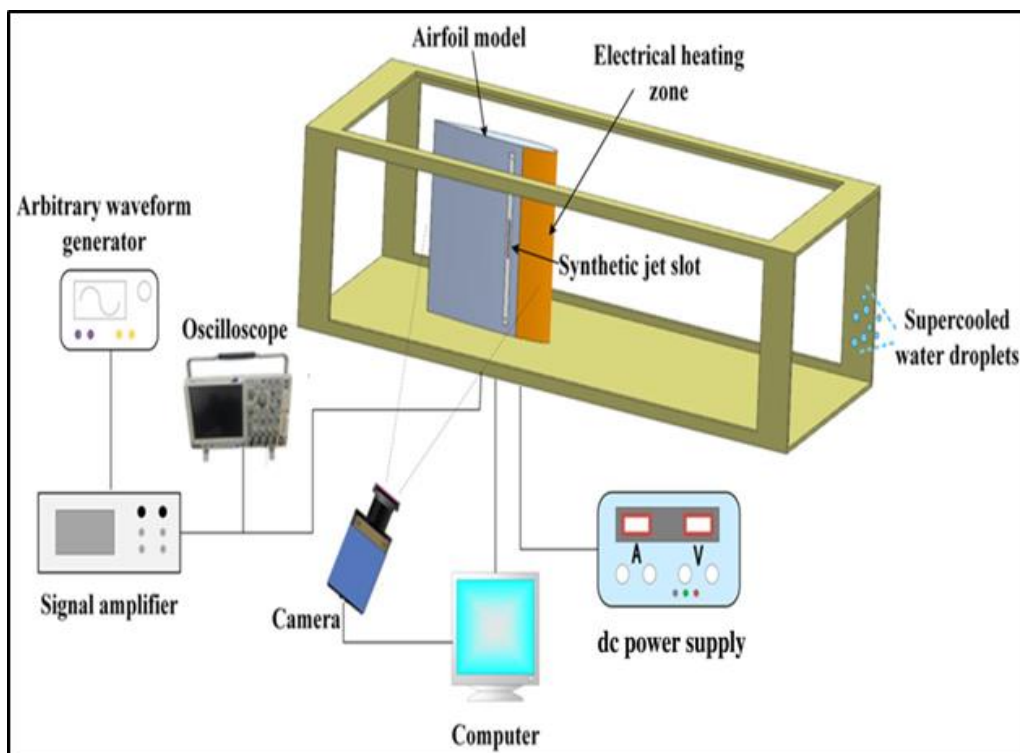


Fig. 1.3: SJ used for de-icing over an aerofoil [11].

Recently, SJs were introduced for this process. This small power heater is inside an aerofoil for just heating of air, and this heated air is circulated through the SJ in a controlled manner, removing ice from the aerofoil. Similarly, a SJ is used for jet vectoring. Boundary layer separation causes losses in a lift force; it creates unwanted vibration in the system. Boundary layer separation can be reduced by providing external energy in fluid or suction of fluid from a boundary. SJs are used to overcome the problem mentioned above. Fig. 1.4 shows the use of a SJ to control a flow separation over an aerofoil at different angles.

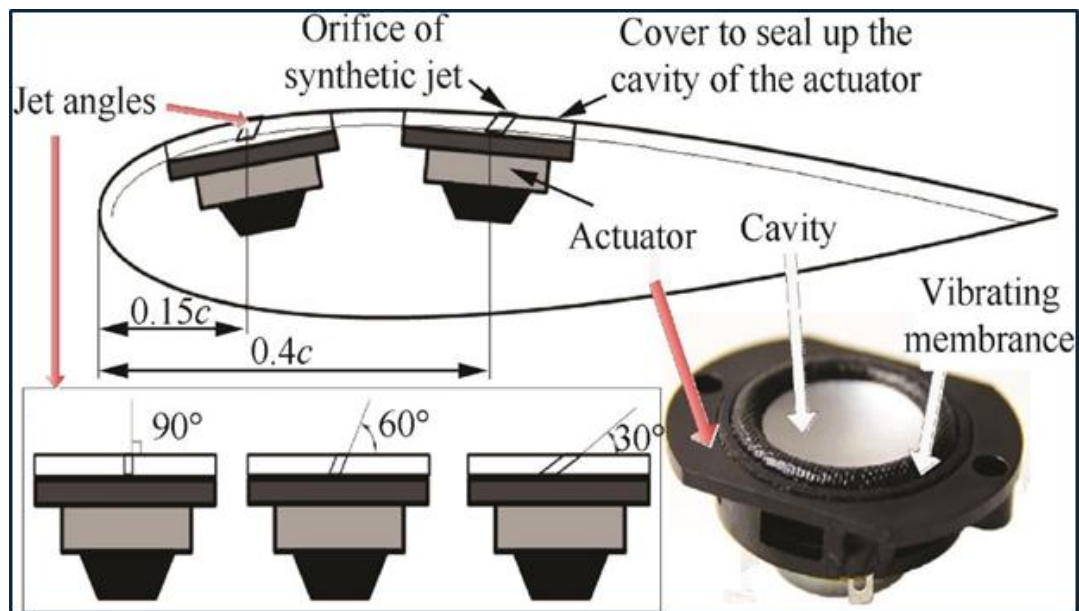


Fig. 1.4: Application of SJ for flow separation control [12].

**Electronic Cooling:** One of the primary applications of SJ cooling is in electronics cooling, particularly in compact electronic devices such as laptops, smartphones, and tablets, as shown in Fig. 1.5. These devices generate significant heat due to the high-power densities of their components. SJ cooling provides an efficient and compact solution for removing heat from electronic components, improving their performance and reliability.

## 1.2. Introduction of aeroelastic energy harvesting

Energy harvesting is the process by which light, thermal, solar, and kinetic energy can be converted to usable energy. The fluid flow has kinetic energy, and fluctuation is created in a fluid flow by external mechanism. Hence, kinetic energy is converted into mechanical strain and stresses are generated, producing electrical energy through piezoelectric material. Piezoelectric materials are the prominent mechanical energy harvesters because of their high electromechanical coupling factor (convert mechanical energy into electrical energy) and piezoelectric coefficient compared to electrostatic, electromagnetic, and triboelectric materials. Advancements in micro and nanoscale electronic devices, which

consume microwatt power, allow these devices to run through piezoelectric generators. The microwatt power can be stored in a capacitor or used to charge a small battery, along with many applications in day-to-day life [14].

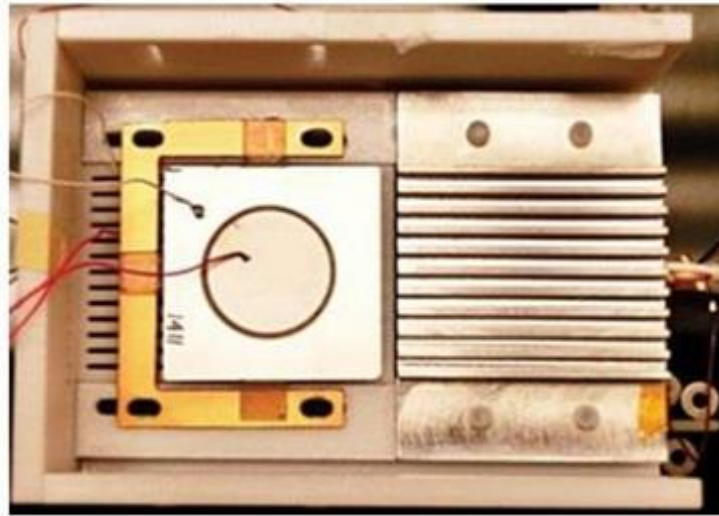


Fig. 1.5: Application of SJ in electronic cooling [13].

Figs. 1.6 and 1.7 shows a block diagram of aeroelastic energy harvesting and the mechanism of aeroelastic energy harvesting, respectively. Free-flowing fluid has kinetic energy or flow energy, and this imparted fluid over a solid structure. Fig. 1.7 shows different structural shapes like aerofoil, cylinder, rectangle, and triangle. The fluid impartment vibration develops in a structure, and the amplitude of vibration will differ for different structures, depending on the angle of attack.

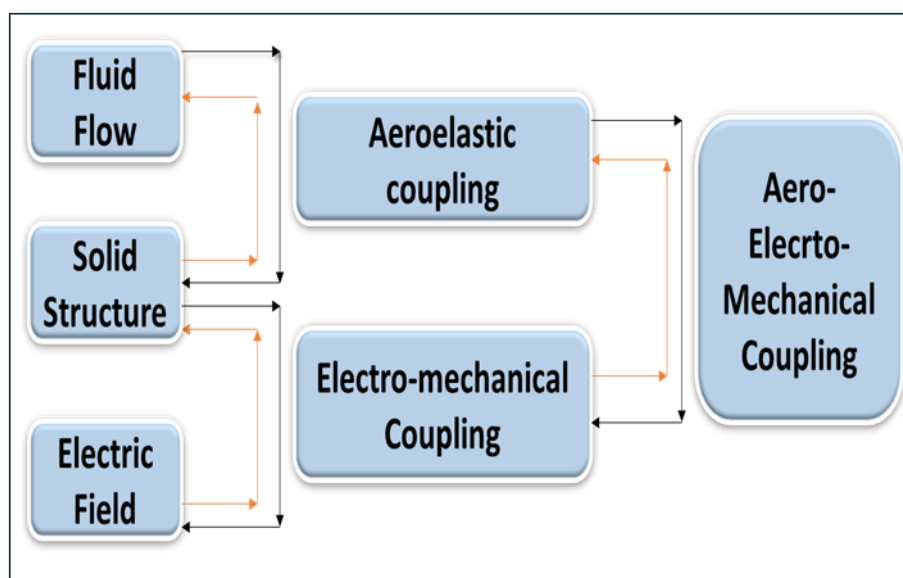


Fig. 1.6: Block Diagram of Aeroelastic Energy Harvesting [15]

Vibration causes elastic deformation in a material. This connecting process is known as aeroelastic coupling, and elastic deformation generates periodic stress in a structure over

piezoelectric material. These stresses in piezoelectric material generate an electrical field. This connecting process is known as electro-mechanical coupling and this whole connecting process is called aero-electro-mechanical coupling.

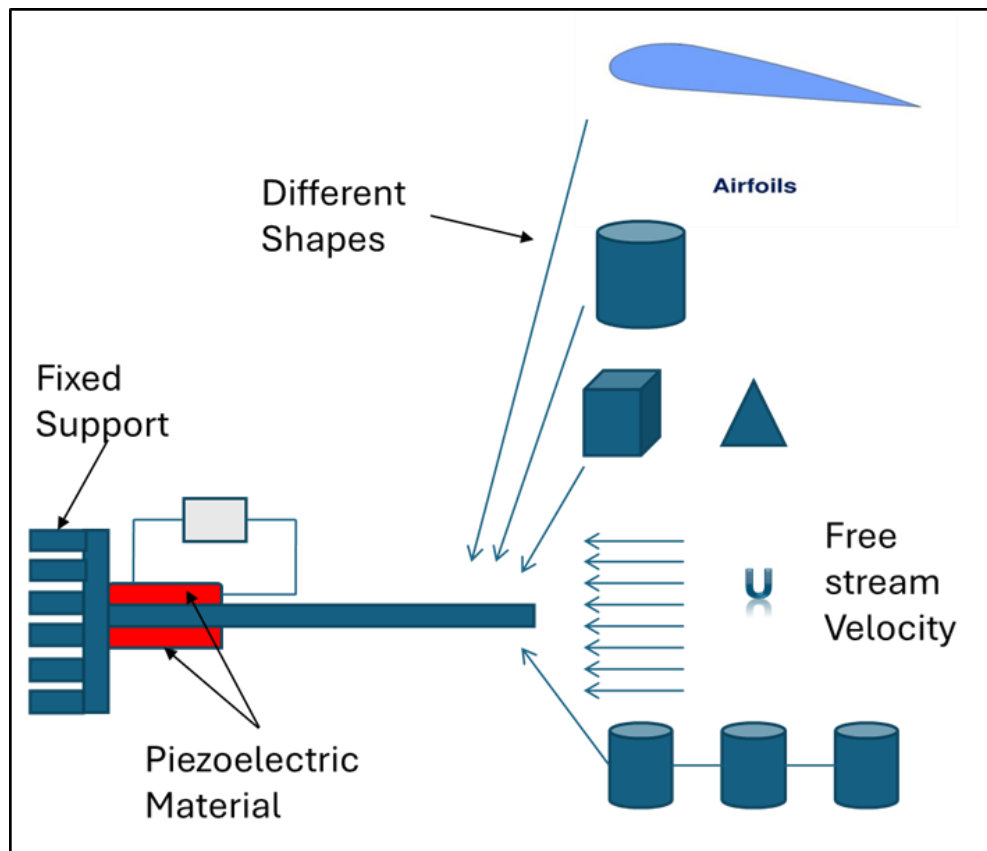


Fig. 1.7: Mechanism of Aeroelastic Energy harvesting

### 1.2.1. Piezoelectric materials

The piezoelectric effect in the material is the ability of materials to generate an electrical field in response to mechanical stress or deformation in response to an electric field; this is called the reverse piezoelectric effect. Piezoelectric material has a non-centrosymmetric crystal structure (their constituent atoms or molecules are asymmetrically arranged). This asymmetry enables the generation of an electric dipole when mechanical stress is applied. Some commonly used piezoelectric materials.

- Lead zirconate titanate. (PZT)
- Polyvinylidene fluoride. (PVDF)
- Gallium nitride. (GaN)
- Barium titanate. (BaTiO<sub>3</sub>)
- Quartz.

PZT and PVDF are commonly used materials for aeroelastic energy harvesting. PVDF is polymer-based, and PZT is a ceramic-based piezoelectric material with a higher piezoelectric and electromechanical coupling coefficient. However, the disadvantage of PZT is its higher manufacturing temperature and consists of lead, which harms human health. Piezoelectric polymers have good mechanical strength, are lightweight, have high electromechanical efficiency, are cost-effective, and easily fabricate into any shape [16].

### 1.2.2. Applications of Piezoelectric materials.

**Piezoelectric sensors:** Piezoelectric material is widely used in sensors to measure physical variables such as pressure, acceleration, flow rate, and wear detection. It converts pressure, acceleration, flow rate, etc., into a surface electrical charge (potential) that can be quickly processed, and the piezoelectric sensor can operate its developed power. Therefore, it does not need to supply any external power for operation. It has more mechanical and chemical stability, a high operating temperature range, and self-sufficiency. A significant advantage is its high sensitivity. Fig. 1.8 shows a piezoelectric sensor placed into a distinct wheel area, monitoring health, damage, and wheel displacement during the train turning. Fig. 1.9 shows next-generation wearable long-term monitoring of the human body, blood pressure and artery diameter; this replaces costly health monitoring equipment.

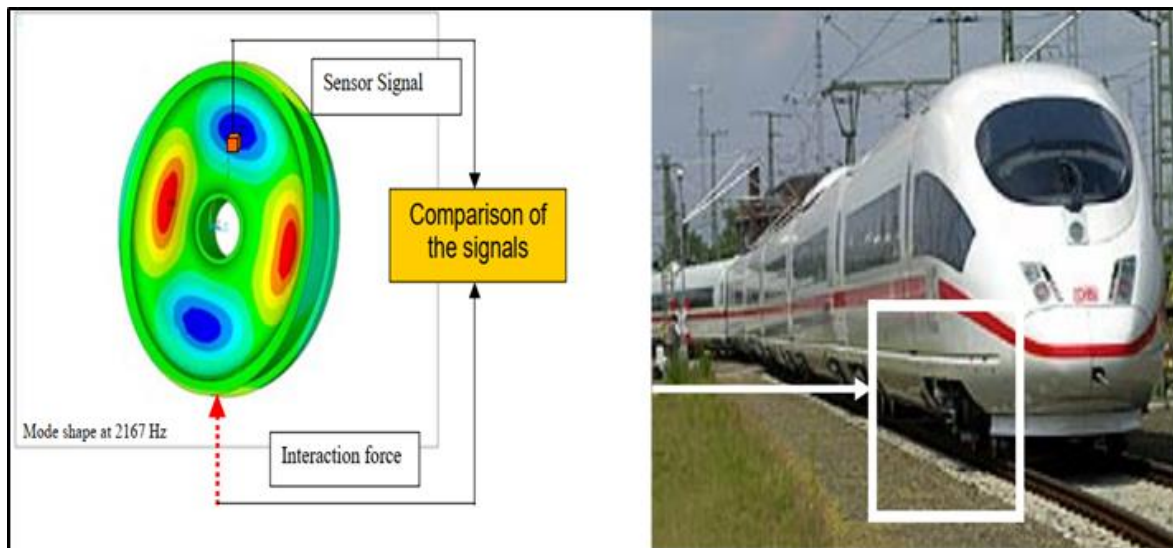


Fig. 1.8: A piezoelectric sensor detects the vibrations of the train wheel [17]

**Energy harvesting:** Piezoelectric material converts mechanical vibration, motion, and pressure fluctuation into electrical energy. This harvested energy can be used in wireless sensor networks to power small electronic devices or sensors in remote locations, as well as wearable electronic and self-powered devices for health monitoring, environmental condition monitoring, and structural health monitoring. Fig. 1.10 shows aeroelastic energy

*Synthetic jet with piezoelectric flaps mechanism for enhancement of heat transfer performance and energy harvesting*

harvesting by bimorph piezoelectric strips(effective from both sides) vibration generated by a D-section cylinder.

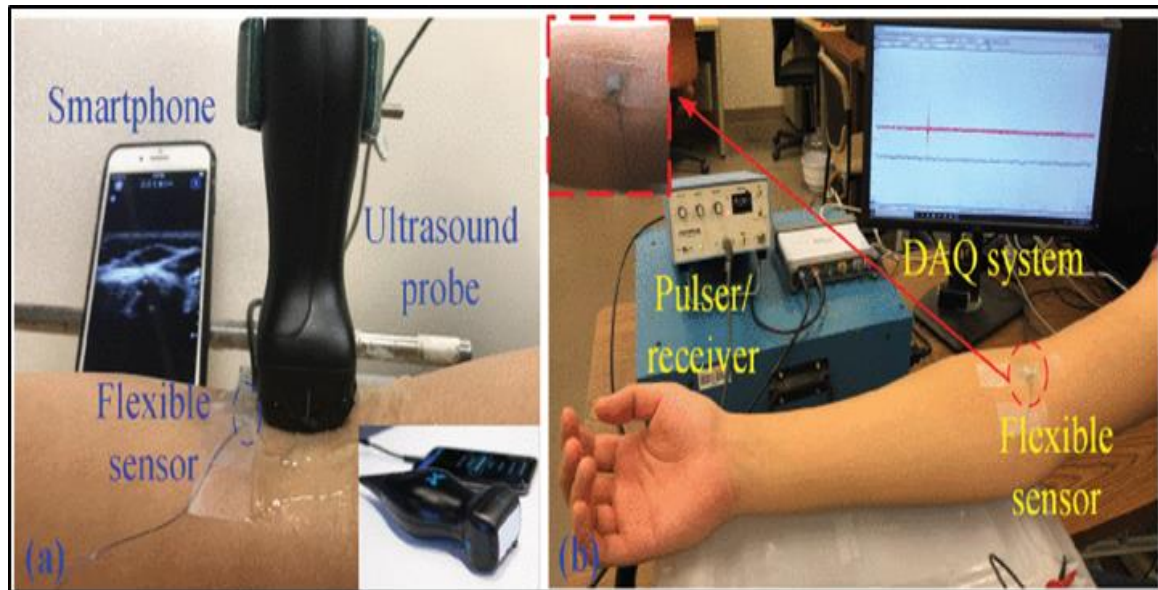


Fig. 1.9: (a) Simultaneous measurement by using flexible sensor and ultrasonic probe, (b) Blood pressure measurement overview [18]

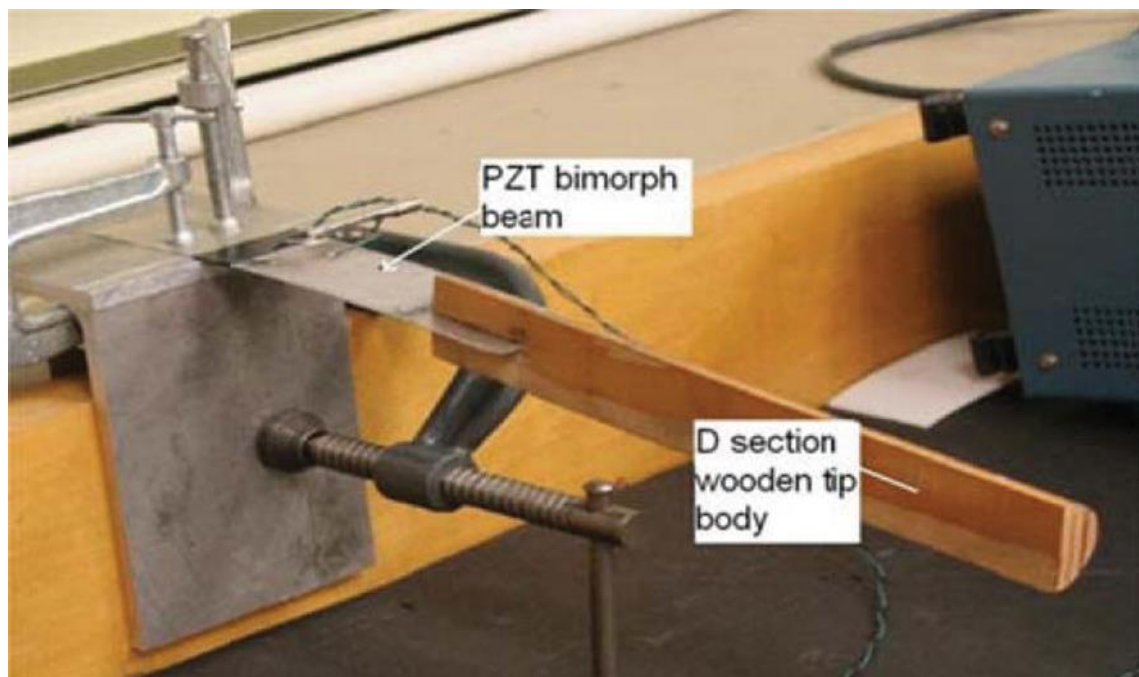


Fig. 1.10: Aeroelastic energy harvesting from D-section structure [19]

Fig. 1.11 shows piezoelectric energy harvesting from the human heart. The human heart has a pulsating suction and ejection of blood. Energy harvesting can be done through flexible piezoelectric material using this pulsating motion. Harvested energy can run different internal body parts like pacemakers, which are operated by a battery.

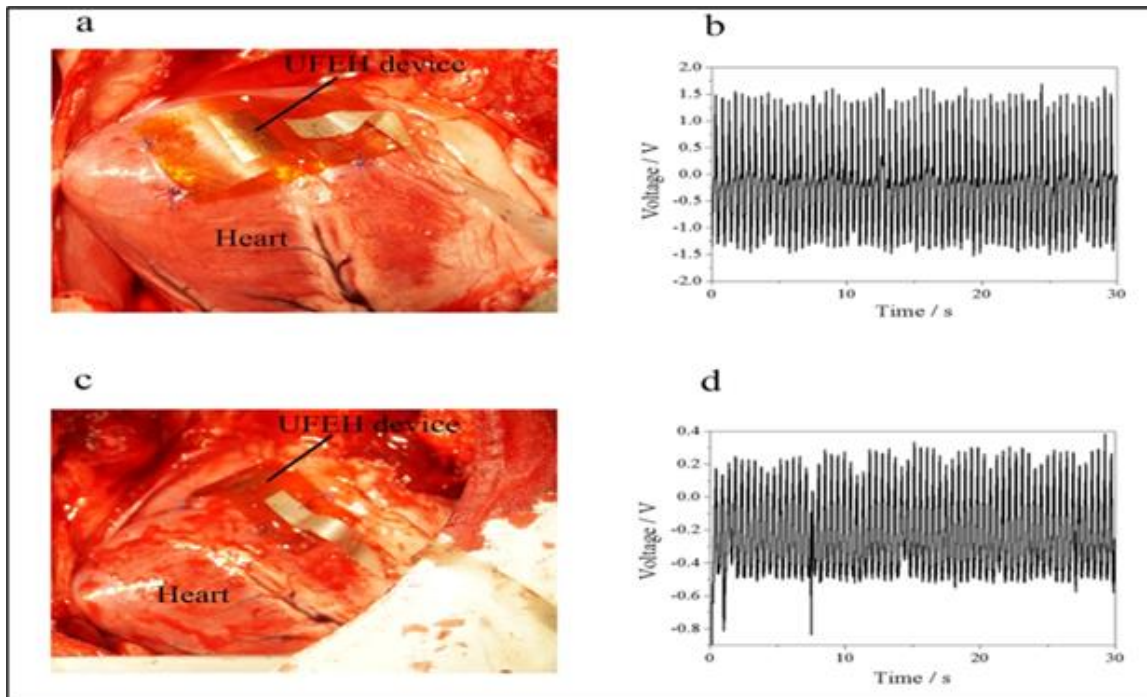


Fig. 1.11: Piezoelectric energy harvesting from the human heart.[20]

In this chapter, the applications of synthetic jet for various cooling and flow control applications have been discussed. The applications relevant to piezoelectric materials have been discussed. With an introduction to these two methodologies, we move to the next chapter which focuses on various studies from the existing literature.

## Literature review and problem formulation

### 2.1. Literature review of SJ impingement.

Smith and Glezer [21] introduced a SJ for thrust vectoring applications. They further studied the evolution of the SJ, stating that the vortices create a turbulent mixing in the radial direction, slow down, and then become a part of the mean jet flow [22]. Mallinson *et al.* [23] conducted a detailed analysis of SJ flow, showing its higher turbulent dissolution and entrainment than the steady jet. Xu *et al.* [24] showed that the entrainment mechanism of SJ differs from the continuous jet in near-field while it shows self-similarity in the far-field region. Smith and Swift [25] compared a fluidic parameter of SJ and continuous jet. Their result showed that in the far field, the SJ velocity profile resembles a continuous jet; however, a near-field SJ has more vortex pairs and more entrainment than a continuous jet. Pavlova and Amitay [26] demonstrated SJ for electronics cooling. They found that the heat transfer performance is two to three times better than continuous jets for the same Reynold numbers due to the coherent vortex rings formed in SJ. Gillespie *et al.* [27] done a study on the variation of Nu to heated surface spacing (Fig. 2.1)

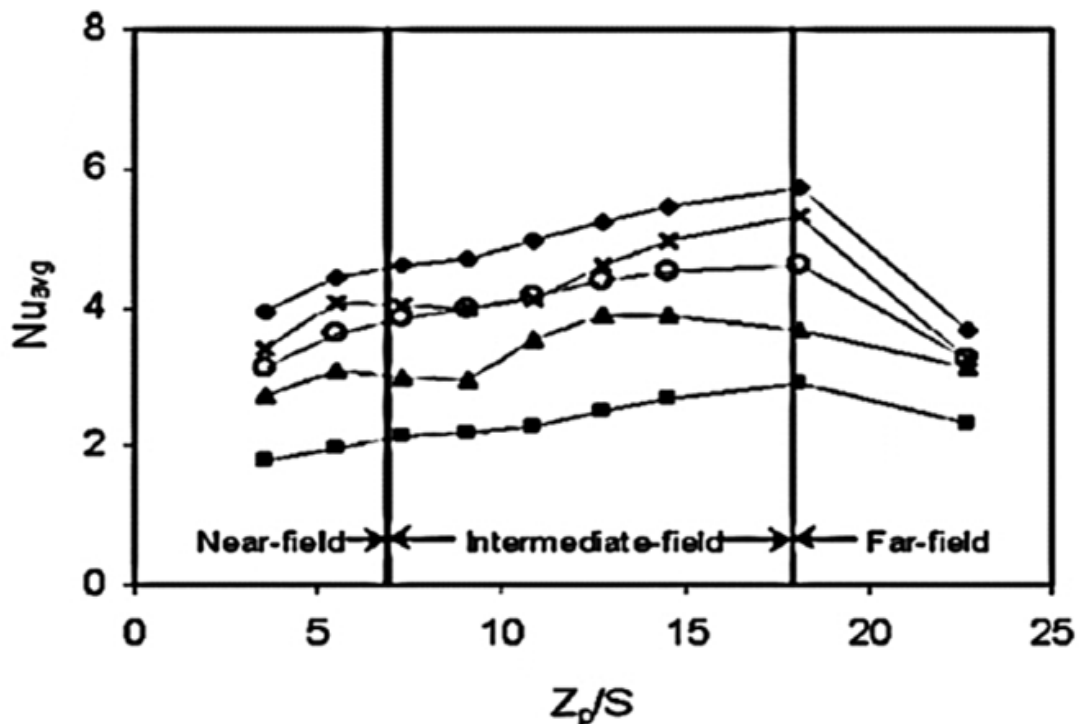


Fig. 2.1: Variation of Nu to the dimensionless ratio of the distance of the heated surface from orifice-to-orifice diameter [27]

Gillispespie et al. [27] found that low heat transfer occurs at lower surface spacing (distance between heated surface and orifice) because the jet was not appropriately developed in this region. Heated air comes in the suction of fluid, and at intermediate surface spacing, heat transfer increases. Because jet vertices are appropriately developed, more fluid entrainment occurs in this region. In the far-field region, jet fluid mixes with the surrounding fluid. Its strength decreases; hence, heat transfer again decreases in this region. Valiorgue *et al.* [28] studied the heat transfer at low values of  $z/d$  for SJ impingement and showed that the stroke length ( $L_0$ ) significantly affects the high heat transfer region. M Chaudhari [29] has extensively studied SJ in various aspects, including the frequency response of SJ cavities and its effect on flow parameters. They show that the cavity dimension affects the fluid flow parameter much less than the orifice dimension. The heat transfer characteristics of SJ found that heat transfer due to SJ is 10-11 times more than natural convection [30]. Figs. 2.2 (a) and (b) show the effect of cavity height and orifice thickness, respectively. In this case, the effect of cavity height is less than orifice thickness on heat transfer performance because of compressible fluid. The reason for the given pressure and temperature volume effect is negligible. Increase orifice thickness flow separation from orifice exit decreases; hence, turbulency decreases due to this heat transfer decreases. Fig 2.2 shows that heat transfer of SJ first increases with an increase in axial distance from the orifice to the heated surface and then decreases. This is due to lower surface spacing (distance between orifice and heated surface) and heated fluid returned into a cavity through the orifice during a suction stroke.

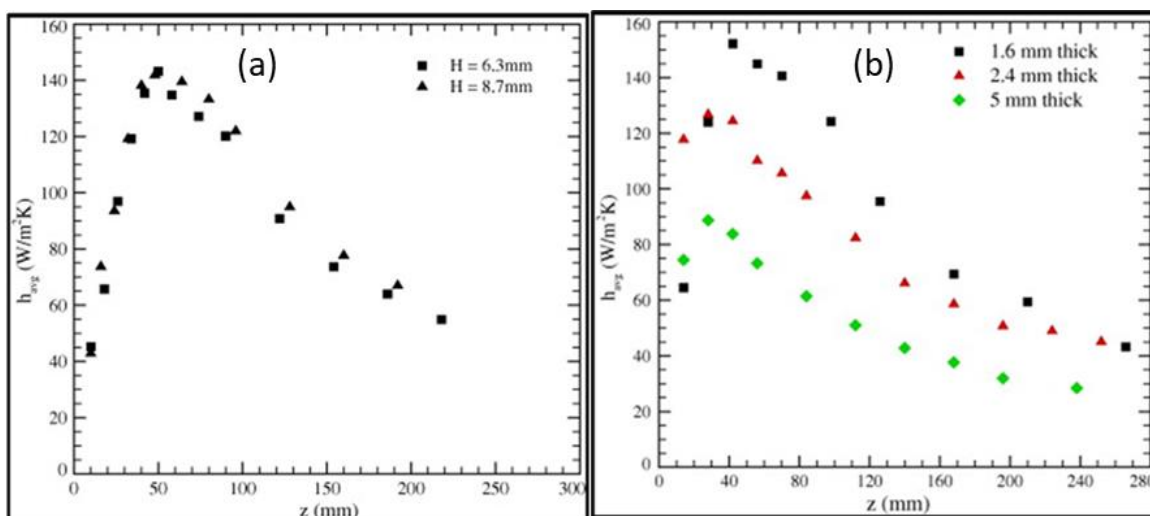


Fig. 2.2: Variation in heat transfer coefficient to (a) cavity height and (b) orifice thickness [30].

The effect of orifice shape in SJ impingement is studied [31]. They found that the heat transfer enhancement in square shape orifices was larger than in rectangular and circular shape orifices for large surface spacing, i.e.,  $Z/D > 5$ , as shown in Fig. 2.3. They also varied the aspect ratio 3-5 for rectangle shape orifices and heat performance of SJ enhanced at lower surface spacing. Gil *et al.* [32] reiterated the effect of recirculated hot air, which reduces the heat transfer potential. Thus, existing literature shows that the SJ outperforms continuous jets at higher  $z/d$ 's ( $>5$ ) but produces inferior performance at lower  $z/d$ 's ( $<5$ ). The recirculation of the heated air during the suction cycle restricts the use of SJ in confined or close-spaced settings. Therefore, researchers are working on improving the heat transfer performance of the SJ further, especially at lower spacings. Various modifications to the geometric, fluidic, and design parameters are being examined to achieve better heat transfer.

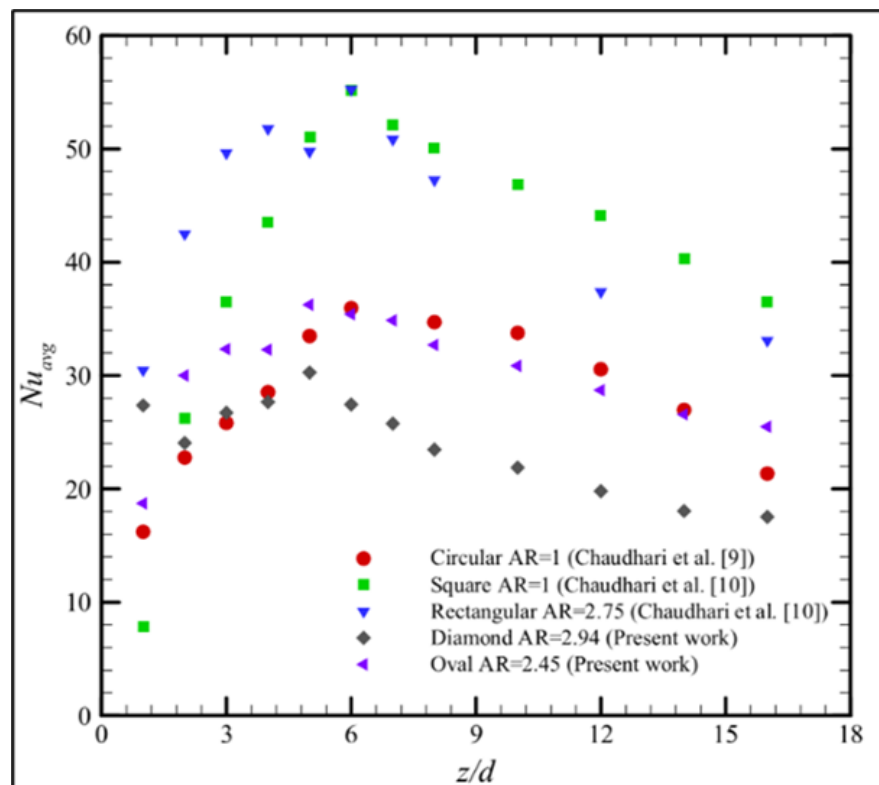


Fig. 2.3: Variation in Nu with axial distance number for different shapes of orifice [33]

Researchers have explored increasing heat transfer at lower surface spacing or suppressing the heated air from a heated surface to an orifice in a cavity. The multiple orifice configuration is studied to overcome the recirculation effect at lower  $z/d$ 's. Chaudhari [34] has done extensive work on multiple orifices. They used a central circular orifice and an adjacent multiple circular orifice (satellite orifice). The heat transfer increases by

approximately 30% compared to a conventional single circular orifice. L. magnate *et al.* [35] studied multiple orifice configurations for different shapes and found up to 75% enhancement in the heat transfer. The heat transfer enhancement was also analyzed through flow visualization techniques using particle image velocimetry (PIV), showing that the multiple orifices increase mixing, flow entrainment, and turbulence. P.K. Singh *et al.* [36] showed that the multi-orifice jet spreads more in the radial direction than the single orifice, producing up to 30% enhancement in the heat transfer.

Fig. 2.4 shows the variation of average Nu with axial distance for a multiple orifice configuration. In this, they get two peaks in Nu for a given configuration. This is because in the near field region, multiple jet mixes and entrainment increase; in the second region, forming a single coherent jet causes heat transfer again to increase. The primary peak disappears if more jets merge in a near-field region.

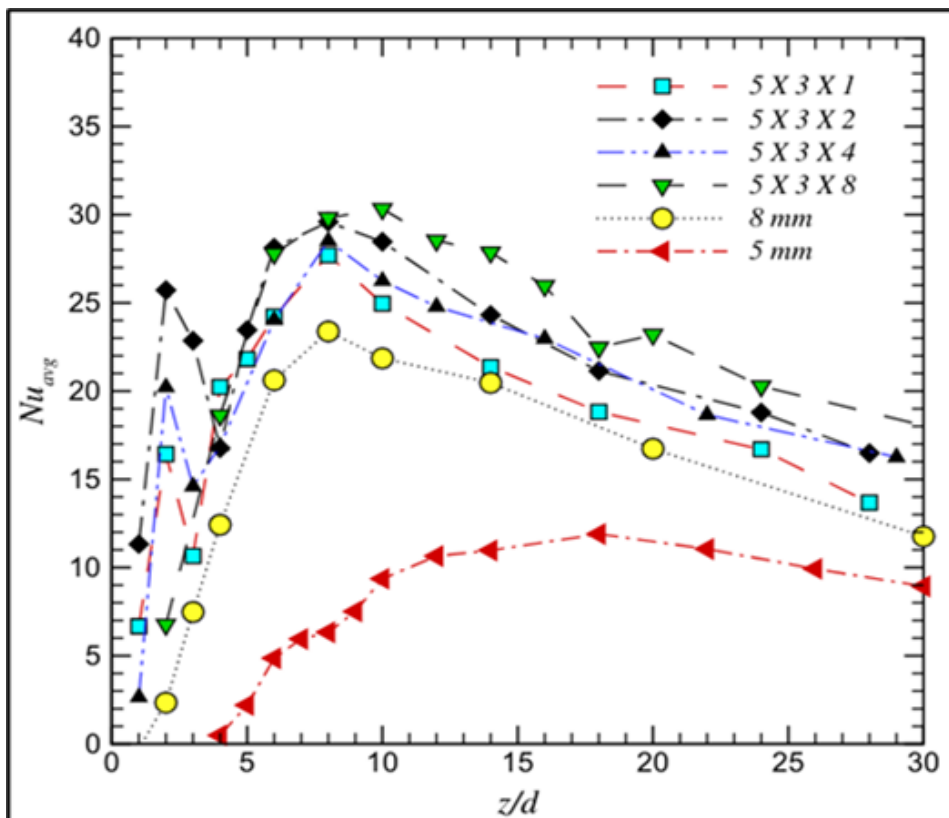


Fig. 2.4: Variation of average Nu with axial distance for a multiple orifice [34]

The above studies showed that the multi-orifice configuration could enhance thermal performance. However, Gil [37] showed that these studies did not keep the equivalent orifice diameter the same in both cases. Thus, the factor by which the improvements are quoted might differ in the actual case. Gil [37] tried to reinvestigate the multi-orifice

configuration, keeping the same area of the orifice exit, and the results showed heat transfer improvements up to  $z/d < 2$ . Because the jet coming from peripheral orifices reduces hot air recirculation during suction stroke, they also showed that the higher  $z/d$  performance of multiple orifices degrades because multiple jets merge into a single jet with less strength than a single jet. Some configurations produce stronger wall jets due to their arrangement, resulting in higher heat transfer rates [38]. The large number of satellites (number of orifices around a central orifice) creates jet entrainment along the axial direction. Another method to increase heat transfer at a lower surface is using different shapes of the orifice with axis switching phenomena, such as the elliptical shape orifice U. S. Bhapkar [39]. Another method is the coaxial shape orifice, which has higher momentum than conventional single orifice SJ, as shown in Fig. 2.5. It also shows periodic stable and unstable topological state. The recirculation region between the orifice and the annular can be effectively controlled to spread the jet. However, minimal work has been done in the literature using this method [40-42].

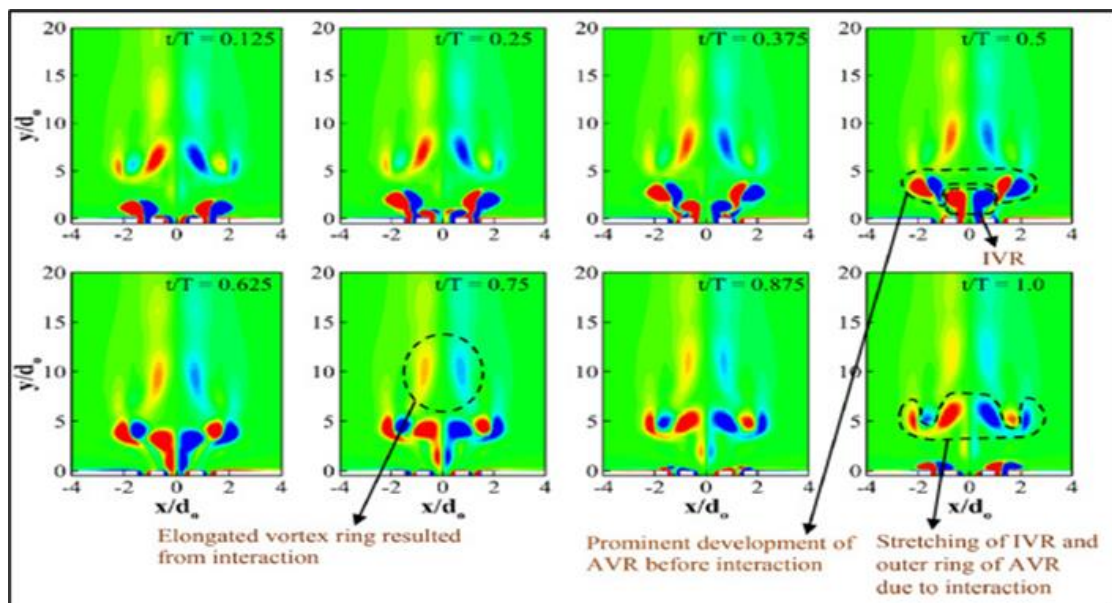


Fig. 2.5: Fluid flow behavior of coaxial SJ orifice [40]

## 2.2. Literature review of aeroelastic energy harvesting

Elahi *et al.* [43] reviewed different mechanisms of flow-induced vibration. Fig. 2.6 shows aeroelastic energy harvesting by vibration created by aerofoil (flutter). This fluid has kinetic energy, which imparts fluid over an aerofoil due to the angle of attack vibrations. These vibrations transfer into a solid structure over piezoelectric material; mechanical strain generates a voltage in a piezoelectric material. F. Petrini [44] experimentally analyses

aeroelastic energy harvesting from wake galloping and vortex-induced vibration. They used cylinders and a T-section design to create vibration in the piezoelectric material; this assembly was placed in heating, ventilation, and air conditioning HVAC ducts.

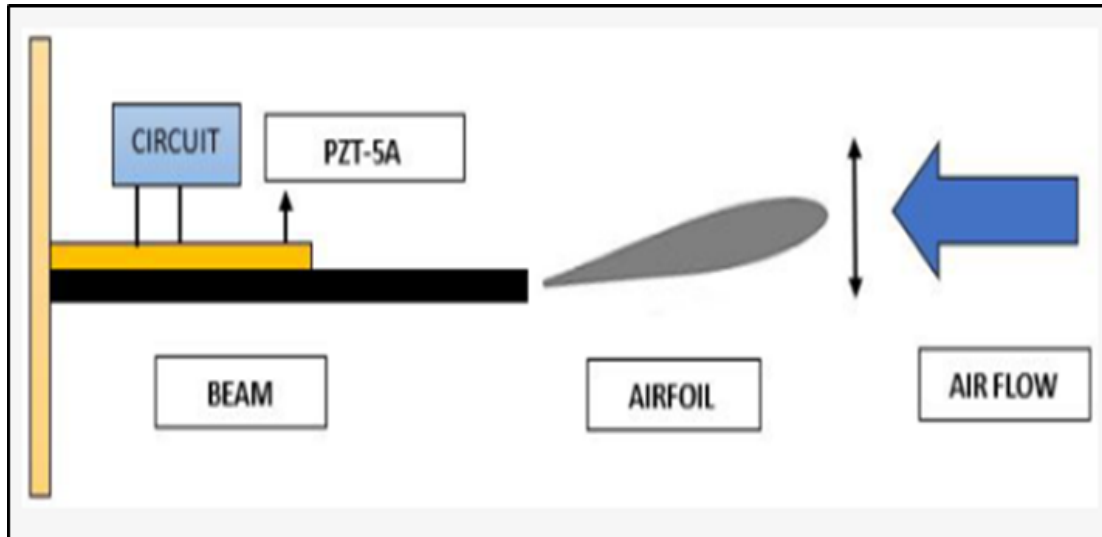


Fig. 2.6: Aeroelastic energy harvesting by vibration generated by aerofoil (flutter) [43]

As shown in Fig. 2.7, milliwatt power is generated by piezoelectric material that can run a different sensor (Temperature, Humidity, Air Quality sensor) used in HVAC ducts. Oceans have tremendous wave energy, and converting it into useful energy requires many turbines that generate large amounts of power. However, small-scale applications like warning lights and different sensors require small power; this demand can be fulfilled by piezoelectric energy harvesting.



Fig. 2.7: Aeroelastic energy harvesting from HVAC duct.[44]

*Synthetic jet with piezoelectric flaps mechanism for enhancement of heat transfer performance and energy harvesting*

X.D. Xie [45] has done a simulation of piezoelectric energy harvesting from sea waves, and they showed power obtained in 45 watts to 145 watts from different configurations. W. B. Hobbes [46], inspired by fluid flow around a tree, formed a Karman-vortex and allowed piezoelectric energy harvesting. They showed vertex strength depends on the distance between cylinders. Wang and Ko [47] utilized a similar concept to obtain peak-to-peak voltage ( $V_{pp}$ ) and instantaneous power of 2.2 V and 0.2  $\mu W$ , respectively, using pressure-induced vibrations. Akaydin *et al.* [48] found that optimal voltage is achieved by matching the dominant frequencies of fluid flow to the piezoelectric system. This is particularly effective when the system is placed at appropriate locations within a turbulent boundary layer or wake region. Vatansever *et al.* [49] have studied the behavior of polyvinylidene fluoride (PVDF) and lead zirconate titanate (PZT) when exposed to the impact of wind and water droplets, at a higher wind speed of 10 m/s, PVDF and PZT generated peak voltage of 61.6 V and 45 V, respectively. They also concluded that the voltage generated depends on the excitation methods, geometry, and the kind of films used. Fig. 2.8 shows that the PVDF piezoelectric material is suitable for energy harvesting from raindrops because it requires a lower excitation force than PZT. Sirohi and Mahadik [50] fabricated a piezoelectric device that could harvest nearly 50 mW of energy at a wind speed of 11.6 mph.

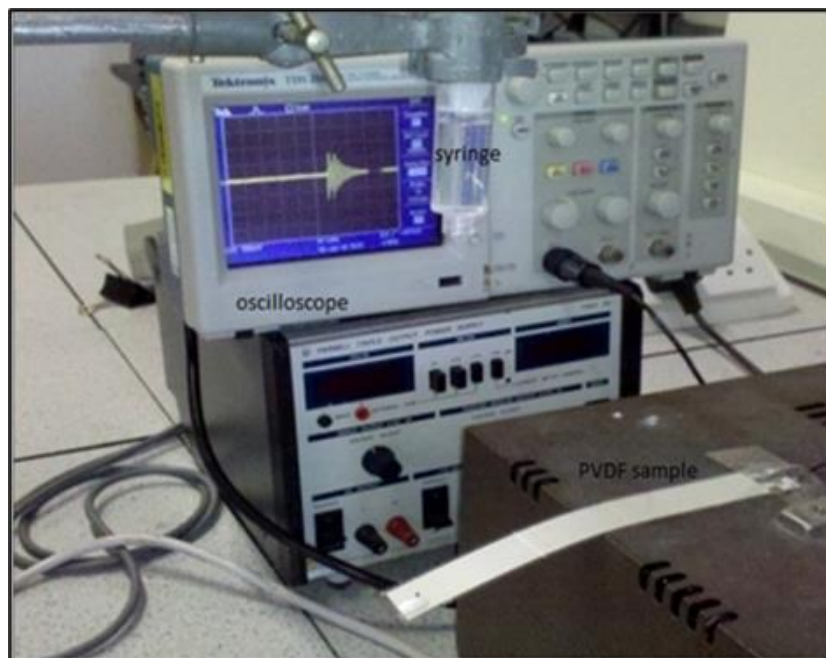


Fig. 2.8: Piezoelectric energy harvesting from raindrops [30]

They used a triangular shape in galloping-based aeroelastic energy harvesting to create a vibration. They showed that the vibration generated by this technique is larger than that generated by the existing design because the triangular shape has a higher angle of attack than other geometrical shapes. Additionally, it was demonstrated that the generated power is contingent on the resistance employed in the measuring circuit. Typically, the power reaches its maximum at a specific resistance, determined by the design of the piezoelectric device [50-51]. Zou *et al.* [51] obtained a maximum of 85 mW of power with a load resistance of 3k $\Omega$  at the highest airflow velocity tested. Arionfard and Nishi [52] experimentally assessed vortex-induced PEH and obtained a maximum power of up to 60 mW. The findings indicate that increasing the Reynolds number (Re) in the flow does not necessarily improve the power generated by PEH. Huang *et al.* [53] developed a pulsating mechanism of air jets for aeroelastic energy harvesting through piezoelectric material. They achieved a maximum open circuit voltage of 12.9 V at a jet velocity of 80 m/s. Fig. 2.9 shows the application of piezoelectric energy harvesting in sensor applications and charging small power batteries. Peak power output was observed to decrease with increased PZT strip thickness.

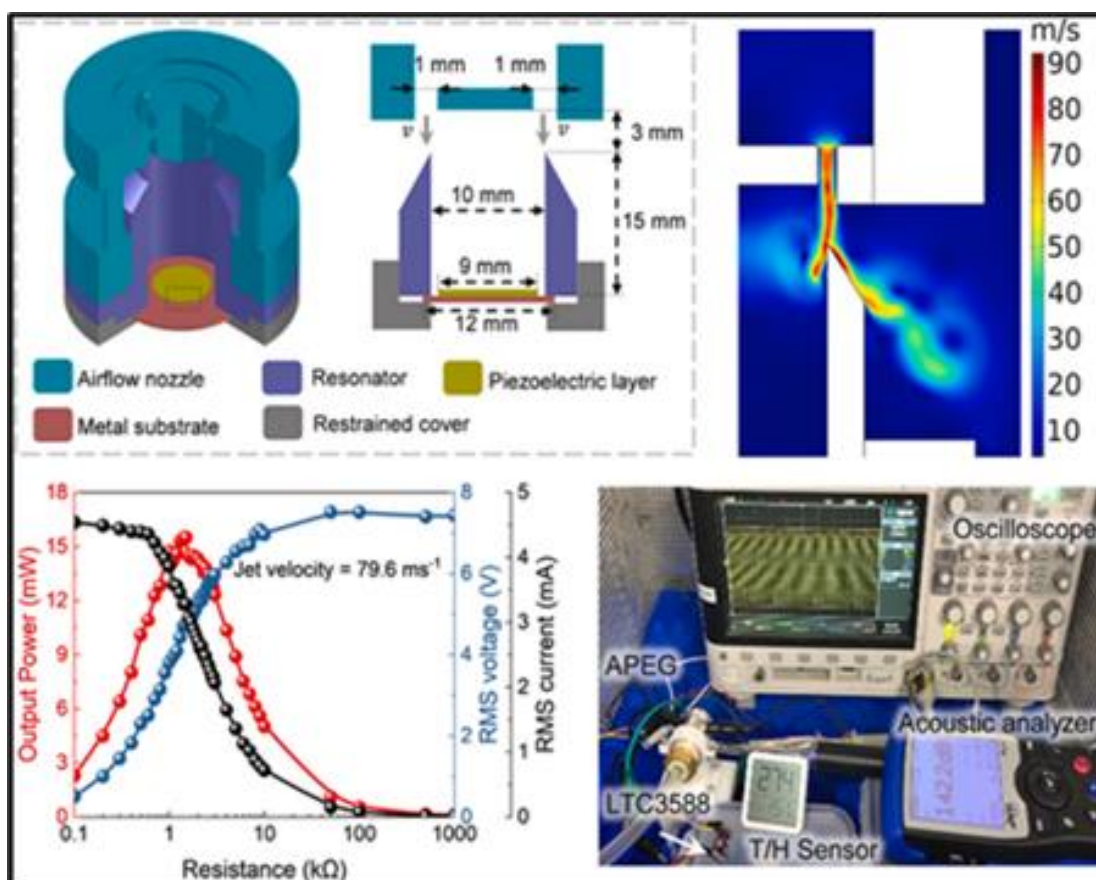


Fig. 2.9: Mechanism and application of aeroelastic energy harvesting [53]

Petrini and Gkoumas [44] used the galloping PEH method inside ducts; the experiments showed that up to 30 *mW* of power could be generated. Different shapes, materials, and techniques used in various applications are reviewed by Liu *et al.* [54]. Thus, these studies show that fluidic energy can generate milliwatts of power by adequately using the flow instabilities.

### 2.3. Gaps in literature and problem formulation.

Figs. 2.10 and 2.11 shows SJ cooling and aeroelastic energy harvesting. As already mentioned, the performance of SJs at lower surface spacing is not good because heated air from the surface comes into a cavity through the orifice during a suction stroke. Researchers have used multiple orifice techniques to solve this problem in literature, but this is less effective. This work seeks to solve this problem using a novel aeroelastic energy harvesting mechanism. After reviewing the literature, aeroelastic energy harvesting is obtained using some external mechanism to create a vibration in the structure.

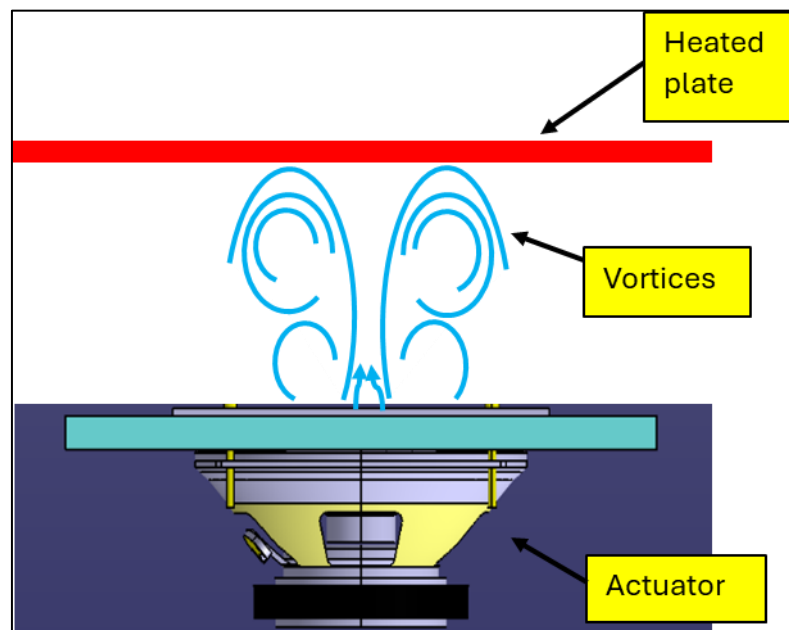


Fig. 2.10: SJ cooling

The present study introduced external mechanisms (flaps) in the fluid path of a SJ, which is expected to change the flow recirculation phenomenon. It might be changing the heat transfer and flow pattern of SJ. This mechanism contains flaps of AISI material over which piezoelectric material discs are pasted with the help of permanent adhesive. It is designed to vibrate at the same frequency as the actuator (SJ actuator) due to the suction and ejection of fluid in an SJ. This is due to vibration stresses developed in piezoelectric material and

stresses an equal number of positive and negative charges transfer to two surfaces. It creates potential differences and milliwatt power produced. Thus, piezoelectric material is used to harvest the energy from the flow and achieve heat transfer enhancement.

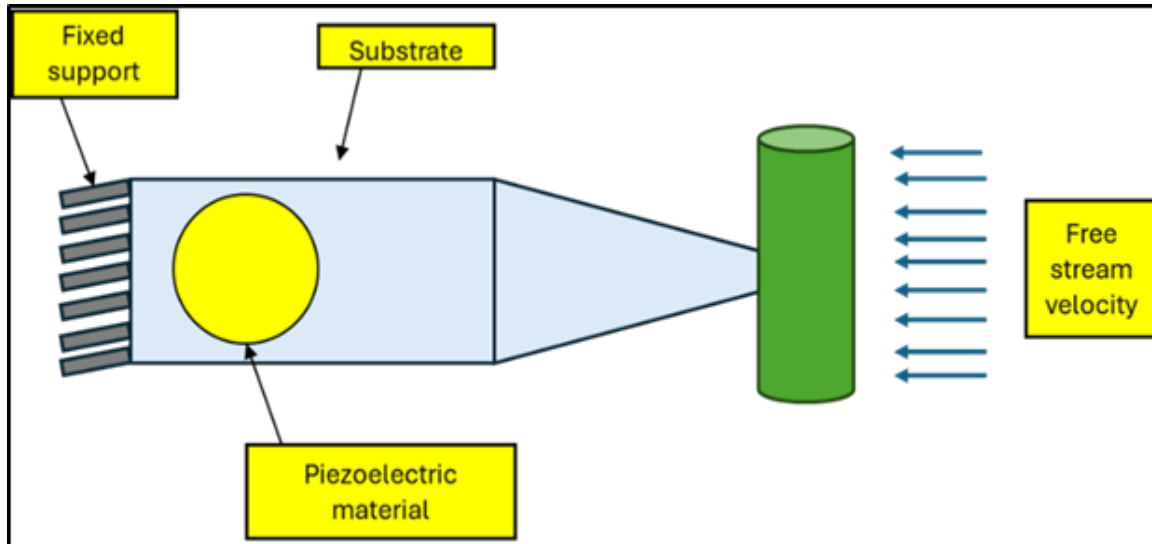


Fig. 2.11: Aeroelastic energy harvesting

The current study introduces a novel design for acoustically actuated SJs with piezoelectric flaps to enhance heat transfer and concurrently enable the harvesting of additional energy. Introducing PZT flaps is supposed to affect the recirculation of air expelled from the SJ. The effect of various surface-to-nozzle ( $z/d$ ) distances is studied on the heat transfer and the voltage generated in the piezoelectric flaps. The height at which the flaps are located from the nozzle exit is also varied to assess its effect on the thermal and electrical performance. The proposed design for the synthetic jet is anticipated to be highly valuable in future thermal management systems across a broad spectrum of critical applications.

## Experimental Methodology

### 3.1. Experimental setup

The experiments are carried out to assess the thermal performance of the proposed SJ with piezoelectric flaps design, and the results are compared with the conventional SJ. The experimental setup for heat transfer measurements is shown in Fig. 3.1. The SJ is generated from an acoustic speaker (DynaVox LW5002PPR-S), which has a diaphragm diameter of 110 mm. An acrylic plate of thickness 10 mm is attached over the open end of the diaphragm to create a cavity. The plate has a thickness of 2.5 mm and an orifice of 20 mm diameter at the center to allow the creation of the SJ. The speaker is operated with a power oscillator (Syscon SI-28DR) and a function generator (Tektronics AFG-1022). The flow in front of the orifice is sucked in and expelled out repeatedly to form a conventional SJ.

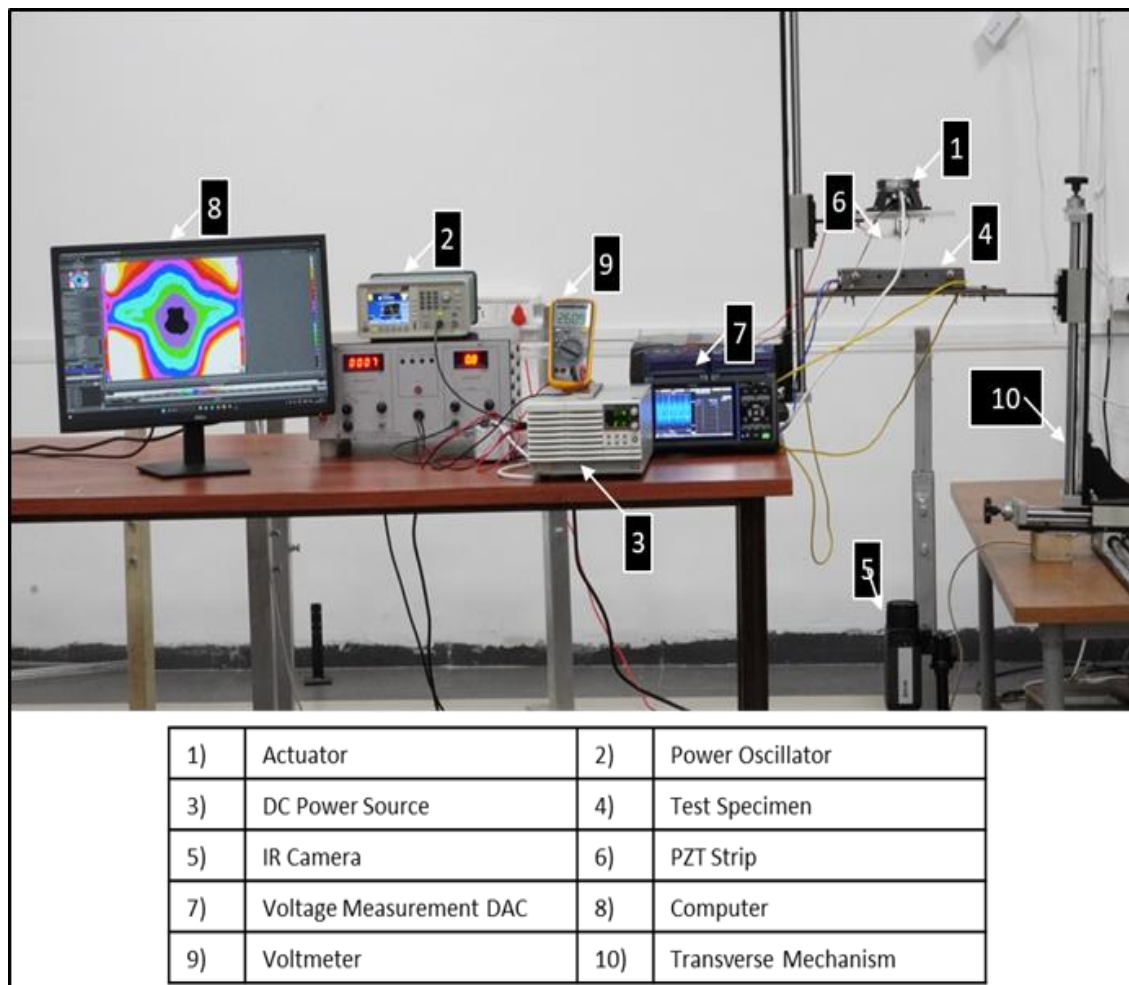


Fig. 3.1: Experimental setup

The new design under investigation has a flapping mechanism in addition to the conventional SJ, see Fig. 3.2. The flaps are mounted on the orifice plate, concentric to the jet centreline, and can move along the jet centreline. The distance between the flap and the orifice exit is referred to as  $h$ , and  $s$  is the distance between the flap and the heated surface. The flap used to have a rectangular shape at the fixed end side and a free-end trapezoidal shape, and it was made of 0.1 mm thick stainless steel (AISI 304). The leading edge of the flap has a width of 8 mm. The length of the flap is kept at least twice the size of the piezoelectric material, as suggested by Yang *et al.* [55]. The piezoelectric patch is then attached to the flap using epoxy resins. The piezoelectric patch consists of a PZT material bonded on brass material, similar to the one used by Sadikbasha *et al.* [56]. The diameter of the piezoelectric patch is 27 mm, with a PZT material diameter of 20 mm. Fig. 3.3 shows the experimental setup visualization's front view and 3D view with four strips. Fig. 3.4 presents three different types of flaps used in experiments.

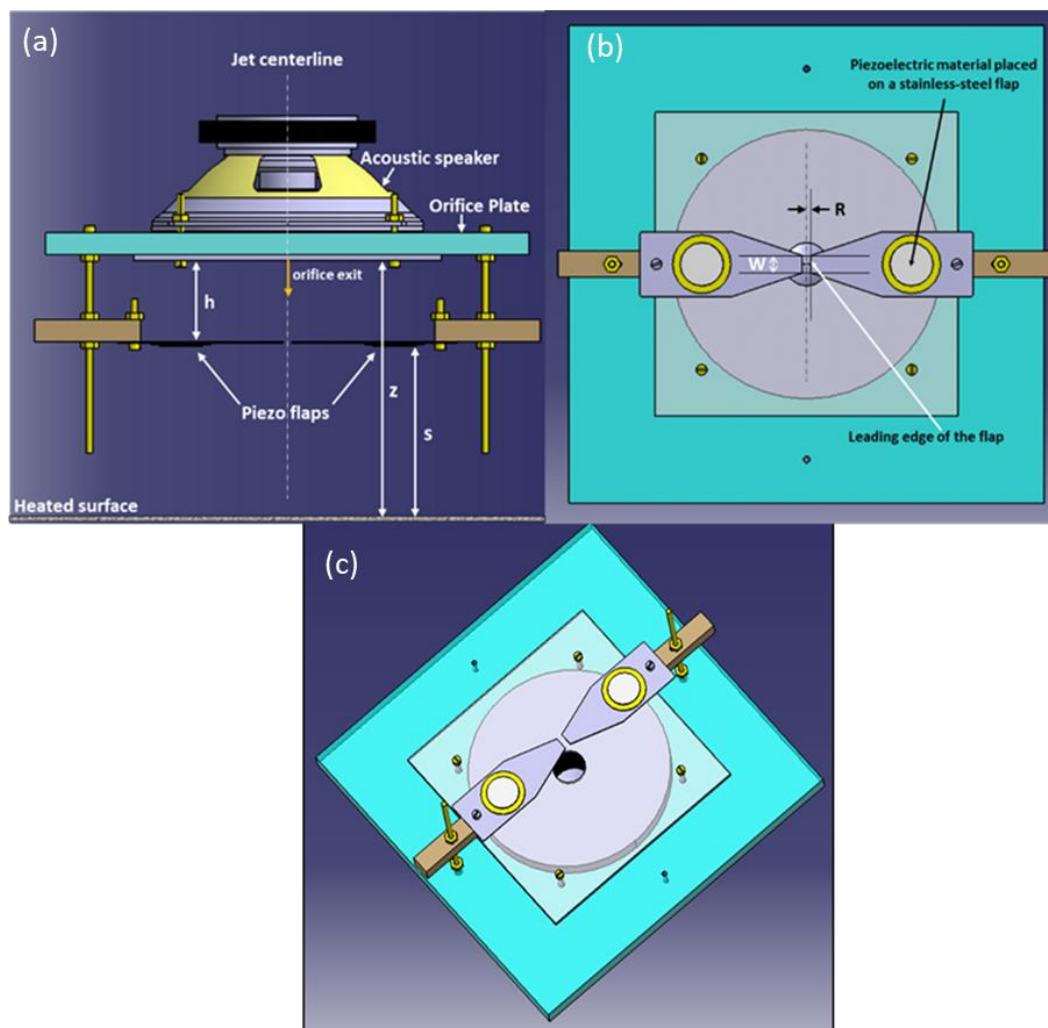


Fig. 3.2: (a) front, (b) top and (c) 3D view of the experimental setup with two flaps.

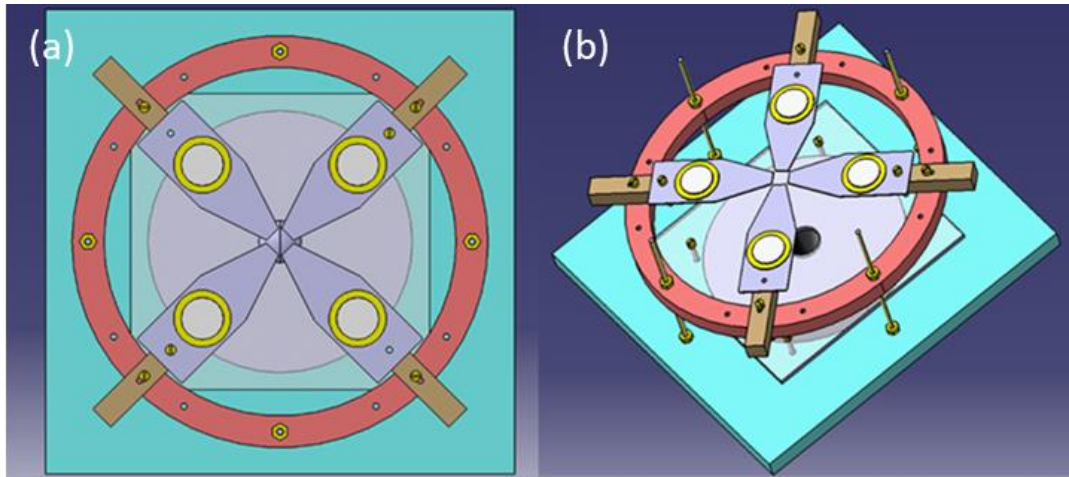


Fig. 3.3 (a) front and (b) 3D view experimental setup visualization with four strips.

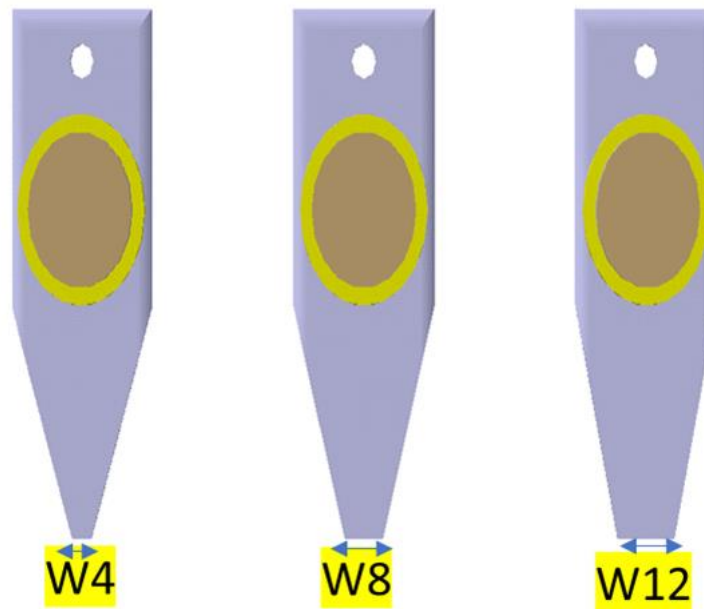


Fig. 3.4 Three different types of flaps were used in experiments.

In the first step, the frequency is obtained, where maximum voltage is achieved from the piezoelectric flap (a combination of the piezoelectric patch and the stainless-steel flap). In this regard, the piezoelectric flap is placed at  $h/d=1$  and is impinged by the acoustically actuated SJ. The frequency of the speaker actuation is adjusted such that the maximum voltage is obtained from the piezoelectric flap, referred to as the resonance frequency. In the current study stage, two piezoelectric flaps are placed opposite each other to study heat transfer from the heated surface. The SJ is operated at the resonance frequency (31 Hz) to compare the heat transfer. The voltage generated is measured across  $150 \Omega$  resistance using a data acquisition unit (HIOKI-LR8450/U8553) at various  $z/d$  and  $h/d$  combinations. The

heat transfer experiments are carried out at a constant voltage input of 10 V to the acoustic actuator. Combining all these operating parameters led to a Reynolds number (Re) and a stroke length of 13000 and 16.2, respectively. The definitions of these parameters are based on the studies carried out by Greco *et al.* [57] and Sharma *et al.* [58], thus avoided here.

The SJ cools a heated surface with a constant heat flux using a DC power source (GWInstek PSW 30-108). The distance between the jet exit and the surface is termed jet-to-surface spacing ( $z$ ). The heated surface is made of stainless-steel foil (AISI 304) with an 80-micron thickness. The foil is stretched between oppositely placed copper bus bars to reduce the temperature non-uniformity over the surface. The foil surface area is  $270 \times 250 \text{ mm}^2$ . The surface opposite to the side of air impingement is uniformly coated with black paint with high emissivity ( $\epsilon=0.97$ ). The temperature of the black surface is measured with an infrared camera (FLIR: A655sc 25°), considering minimum heat loss across the foil thickness due to conduction. The frame rate of 50 Hz is used to capture the temperature distribution over the surface. The camera's resolution is such that one pixel equals 0.33 mm. The heated surface is mounted on the linear traverse mechanism to allow movement along the jet centreline. The assembly of the heated surface and techniques to calculate the heat loss are similar to previous studies [59]. The process is briefly summarized here. The net input flux ( $q_{conv}$ ) is the heat flux supplied to the heated surface after reducing the heat losses ( $q_{loss}$ ) due to natural convection, radiation, and conduction. The total input heat flux supplied ( $q$ ) to the heated surface is calculated using the current and voltage (measured across the foil being heated) provided using the DC power source.

$$q_{conv} = q - q_{loss} \quad 3.1$$

$$q_{loss} = 14.5047 * \Delta T - 30.9431 \quad 3.2$$

where  $\Delta T$  is the difference between the surface and ambient temperatures when a steady state arrives. After finding  $q_{conv}$  at every pixel of the image the IR camera acquires, an instantaneous Nu is derived at these pixels as follows.

$$Nu(r) = \frac{q_{conv}}{\Delta T} \frac{d}{k_{air}} \quad 3.3$$

where  $d$  is the diameter of the orifice exit,  $k_{air}$  is the thermal conductivity of air. The experiments are carried out at an ambient temperature of  $26.5 \pm 1.5 \text{ }^\circ\text{C}$ . The ambient temperature is measured with a thermocouple with an associated uncertainty of 1.5 %. When the steady state arrives while the jet is impinging, images are acquired using the IR

camera at 50 Hz. These images are used to calculate the local time-averaged Nusselt number,  $Nu_{avg,r}$

$$Nu_{avg,r} = \frac{1}{T} \int_{t=0}^{t=T} Nu(r) dt \quad 3.4$$

The local-time averaged Nu is averaged over the defined circular area to find the area-averaged  $Nu_{avg}$

$$Nu_{avg} = \frac{1}{r} \int_0^r \frac{1}{T} \int_{t=0}^{t=T} (Nu_{avg,r}) dt dr \quad 3.5$$

The area over the Nu is averaged is decided keeping in mind the different types of applications. For spot cooling, a circle with a 40 mm diameter is used, whereas a 160 mm diameter circle is used for wide area cooling. For calculating the time-averaged Nu, the values are averaged over at least 50 actuation cycles of the SJ. The measurement uncertainties of various major parameters are given in Table 3.1.

Table 3.1 Experimental uncertainties estimated in the current set of experiments.

<b>Parameter</b>	<b>% Uncertainty</b>
Reynolds number (Re)	4.34
Net input heat flux ( $q_{conv}$ )	6.0
Average Nu ( $Nu_{avg}$ )	6.33

### **3.2 Validation of the measurement techniques**

The heat transfer results obtained with the current measurement techniques are compared with the existing data in the literature. Using different actuation mechanisms changes the stroke length of the SJ with the same operating flow conditions. Thus, it is difficult to reproduce the results of different SJ setups using the current setup of SJ generation. Hence, two sub-methods are deployed to ensure the validity of the measurements. First, the heat transfer results for the steady jet impingement are compared with Lee and Lee [60] (Fig. 3.5), and the SJ is compared with Greco *et al.* [57] (Fig. 3.6). The Figs. 3.5 and 3.6 show that the results obtained from the heat transfer measurement techniques employed in the current set of experiments closely match the existing literature data. Therefore, the same techniques are used to measure the heat transfer rates in further investigation.

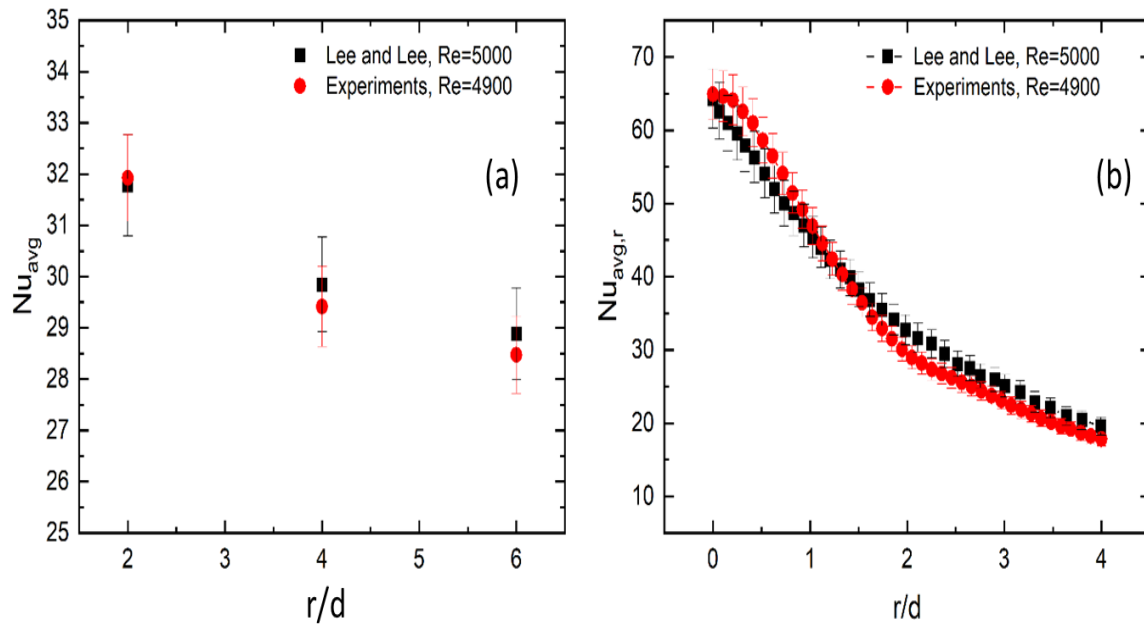


Fig. 3.5: Validation of heat transfer measurement technique in the present experimental setup spacing for steady jet impingement with Lee and Lee for (a) average  $Nu$  and (b) local  $Nu$  at  $r/d=6$  [60]

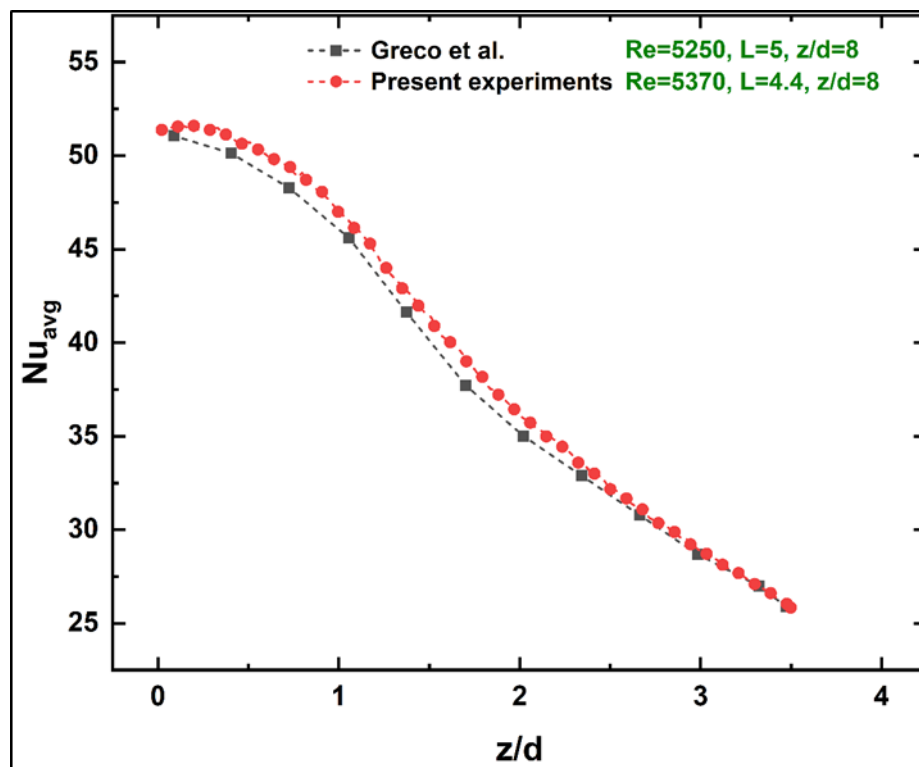


Fig. 3.6: Validation of heat transfer measurement technique in the present experimental setup spacings for SJ impingement with Greco *et al.* [57]

---

## **Results and Discussions**

---

This chapter discussed experimental results and understood the flow and heat transfer behavior of the SJ impingement with piezoelectric flaps. The performance of conventional SJs at different combinations of  $z/d$  and  $h/d$  spacings is analyzed. The voltage generated from the energy harvested due to the flow impinging on the piezoelectric flaps is analyzed. The improvements in the novel SJ with piezoelectric flaps design are compared to the conventional SJ.

### **4.1. Heat transfer performance.**

The low heat transfer rates achieved at low jet-to-surface spacings ( $z/d < 5$ ) are a concern in the conventional SJ methods due to the recirculation of the heated air towards the orifice during the suction stroke. The same heated air is again impinged in expulsion stroke, reducing the heat transfer potential. The addition of the piezoelectric flaps is expected to alter the recirculation patterns of the air thus significantly affecting the heat transfer rates at lower  $z/d$ 's.

#### **4.1.1. The conventional SJ.**

The average heat transfer rates over the surface are represented by  $Nu_{avg}$  distribution. Fig. 4.1 shows the thermal behavior of the SJ at different  $z/d$  values over different surface areas when the acoustic speaker is operating at  $Re=13000$ . The area  $r/d=1$  gives an idea for spot cooling, where the heat transfer is calculated over a circle of 40 mm ( $r/d=1$ ) diameter centered around the stagnation point. Similarly,  $r/d=4$  gives insights into heat transfer rates over a wider circular area with a diameter of 160 mm ( $r/d=4$ ). It is observed that the average heat transfer rate is low in confined spaces ( $z/d \leq 4$ ), reaches a peak value near  $z/d \sim 7$ , and starts increasing with increased jet-to-surface spacing. After  $z/d=8$ , the decrement is observed. The trend of  $Nu_{avg}$  with  $z/d$  for the conventional SJ follows well with the available results in the existing literature [29, 61-62]. Fig. 4.2 shows the average  $Nu$  variation with  $z/d$  for the synthetic and steady jets. Here, both jets' diameter and centreline velocity are kept constant. It is seen that the steady jet performs better than the SJ when the  $z/d$  value is less than 4.5, but the SJ dominates beyond that point. The inferior performance of the SJ at lower  $z/d$  is attributed to the recirculation of heated air at low orifice-to-surface spacings [29, 61].

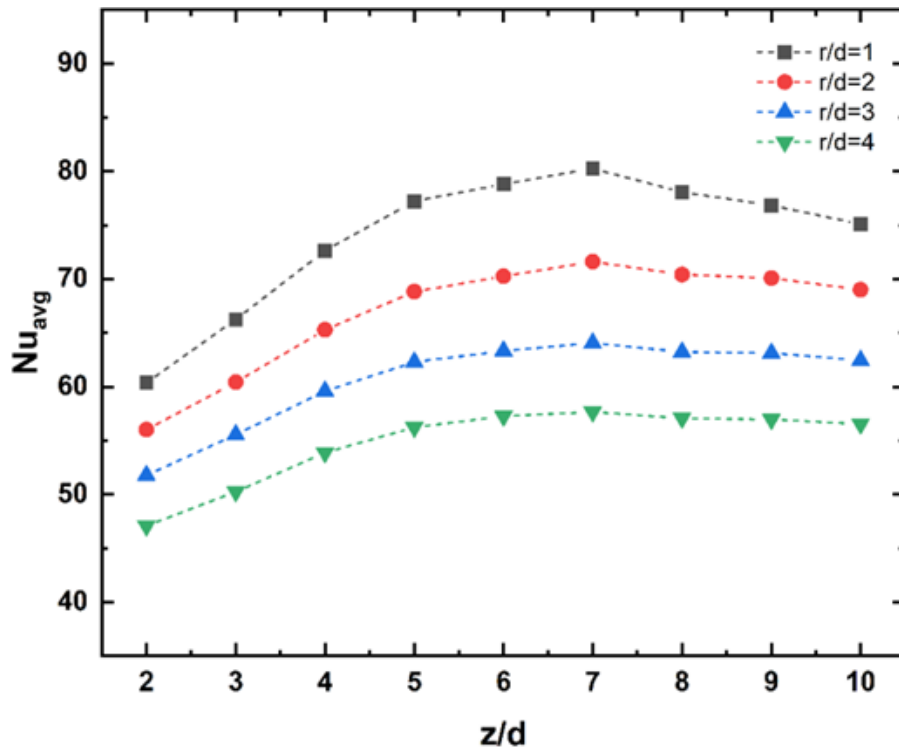


Fig. 4.1: Conventional SJ area-averaged heat transfer over different surface areas at various axial distances.

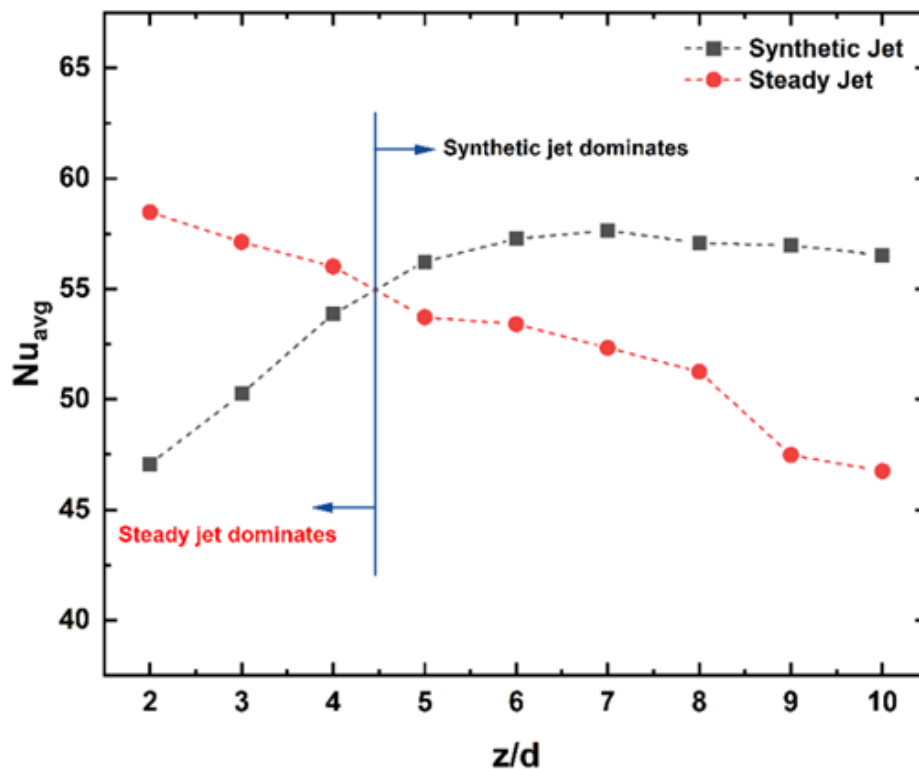


Fig. 4.2: Heat transfer performance (wide area cooling,  $r/d=4$ ) of the steady jet vs. SJ at various  $z/d$  values.

At lower  $z/d$  values, the hot air is drawn inside the cavity during the suction stroke, and the same fluid is expelled out in the expansion stroke. Therefore, relatively heated air is impinged on the heated surface, thus reducing the heat removal potential, which is not the case after  $z/d=5$ . As the SJ travels streamwise, it interacts with the surrounding fluid and carries the entrained ambient air toward the surface to be cooled. Thus, flow spreads in the radial direction, causing a reduction in the axial velocity and effectively enhancing the heat transfer away from the stagnation point. The reduction in  $Nu_{avg}$  starts after  $z/d=7$  due to a significant reduction in the momentum of the jet flow; the additional entrained air cannot compensate for it. Thus, a performance improvement is required to enhance the usefulness of the SJ in thermal management in confined spaces. The subsequent section discusses how the SJ with piezoelectric flaps will affect heat transfer in confined spaces.

#### **4.1.2. The SJ with two piezoelectric flaps.**

The thermal performance of the SJ piezoelectric flaps is compared with conventional SJs in two different surface areas. First, the  $Nu$  is averaged over a circle of 40 mm diameter ( $r/d=1$ ), referred to as spot cooling. After that, the  $Nu$  averaged over a circle of 160 mm diameter ( $r/d=4$ ), termed wide area cooling, and the region  $r/d=2$  and  $r/d=3$  lies between them. The enhancements obtained in the new SJ design are discussed along with plausible reasons. Fig. 3.4 shows different types of strips used in the experiment. These are W8, W12, and W4. Here,  $W$  is the strip end width in mm. The aim of using three different types of strips is to vary the area of the strip in a fluid path, which changes the pressure and turbulence. Initially, two strips are used, and changes in radial locations R2, R3.5, and R5 (distance from the center of the orifice to strip end width) Fig. 3.2 radial location change aims to change an area of fluid flow. Fig. 3.3 shows four strips; the number of strips aims to increase turbulence in a fluid path. Two flaps (opposite each other) are placed in the path of the jet travel, which is expected to alter the flow behavior of the jet impingement. The location of the flaps is varied along the jet centreline at different  $z/d$  values to analyze its effect. The radial location of the flap is also changed to see how the heat is affected.

Fig. 4.3 shows the heat transfer characteristics of the SJ with piezoelectric flaps located at different  $h/d$  values for a W8 strip and radial location R5. R5 indicates that the leading edge of the piezoelectric flap is 5 mm away from the centreline of the jet impingement. Figs. 4.3 (a) and 4.3 (b) display the  $Nu_{avg}$  magnitude and the percentage change observed for spot cooling, respectively, compared to the conventional SJ across various combinations of  $z/d$  and  $h/d$  values. The maximum value of  $Nu_{avg}$  goes up to 100 at  $h/d=3$ ,  $z/d=4$  and  $h/d=3.5$ ,

$z/d=4.5$ . The percentage enhancement in the magnitude of  $Nu_{avg}$  up to 36% using piezoelectric flaps. Figs. 4.3 (c) and 4.3 (d) display the  $Nu_{avg}$  magnitude and the percentage change observed for wide area cooling, respectively, compared to the conventional SJ across various combinations of  $z/d$  and  $h/d$  values. The maximum  $Nu_{avg}$  65 and percentage enhancement up to 20 % can be obtained. The degradation in heat transfer characteristics is observed after  $z/d=6$  for both the areas considered for cooling for the tested set of parameters.

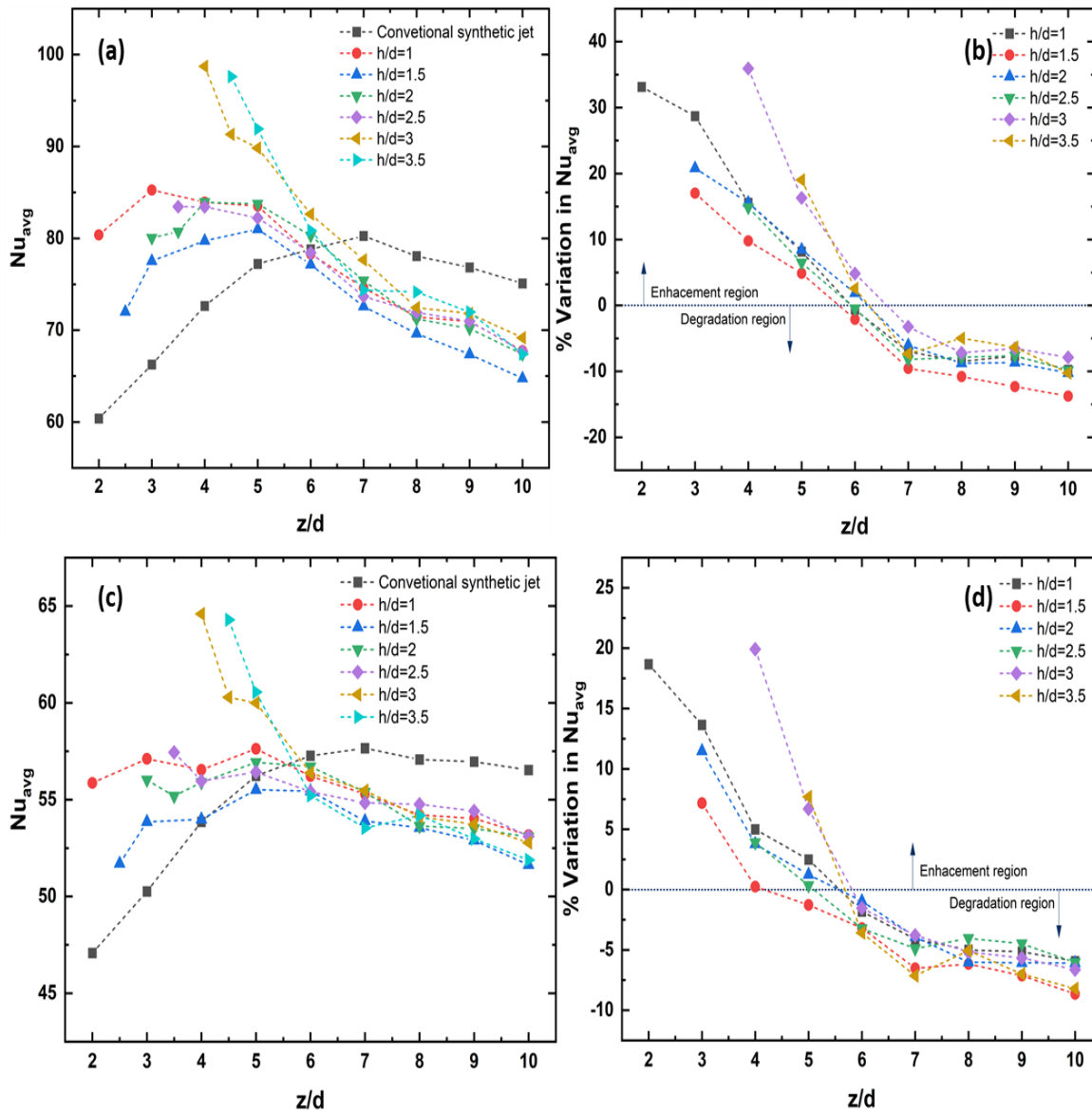


Fig. 4.3: Heat transfer rates of the SJ with piezoelectric flaps at different combinations of  $z/d$  and  $h/d$  value for W8 two strips at radial location R5  $Nu_{avg}$  at spot cooling circle of (a) 40 mm dia ( $r/d=1$ ) and wide area cooling (c) 160 mm dia ( $r/d=4$ ); % enhancement in  $Nu_{avg}$  at (c) ( $r/d=1$ ) and (d) ( $r/d=4$ ) compared to conventional SJ.

There are two prominent reasons behind the increased heat transfer rates for  $z/d < 6$ . First, including two piezoelectric flaps boosts convective heat transfer at the surface by augmenting turbulence levels attributed to the vibrating motion of the flaps. The second reason is that the recirculation of the heated air is mitigated in these cases. The hot air that usually goes towards the orifice during the suction stroke of the conventional SJ cannot go back that effectively due to intense mixing by the flapping motion of the piezoelectric flaps. Combining these two factors enhances the  $Nu_{avg}$  for  $z/d < 6$ . For  $z/d > 6$ , the degradation is observed for the tested  $h/d$  values. The SJ spread is faster in the near-field region, enabling enhanced spread in the radial direction and velocity decay in the axial direction [24]. With an increased value of  $z/d$ , the velocity of the SJ impinging on the flap reduces, thus reducing the amplitude of the flapping. This results in lower turbulence levels between the flaps and the heated surface. A degradation of up to 15% is observed after tested combinations of the  $z/d$  and  $h/d$  values.

Fig. 4.4 shows heat transfer attributes when the two flaps are located at R3.5. Figs. 4.4(a) and 4.4(b) illustrate the magnitude of  $Nu_{avg}$  and the percentage change observed in spot cooling, respectively, compared to the conventional SJ across different combinations of  $z/d$  and  $h/d$  values. The maximum value of  $Nu_{avg}$  goes up to 98 at  $h/d=3.5$ ,  $z/d=4.5$  and a maximum enhancement in the  $Nu_{avg}$  is 28% at  $h/d=2$ ,  $z/d=3$ ; again, the difference between  $h/d$  and  $z/d$  is 1 at optimum heat transfer conditions. Figs. 4.4(c) and 4.4(d) depict the magnitude of  $Nu_{avg}$  and the percentage change observed in wide-area cooling, respectively, compared to the conventional SJ across various combinations of  $z/d$  and  $h/d$  values. It follows a similar trend to the R5 case, where the percentage enhancement or degradation levels are reduced compared to spot cooling. A maximum  $Nu_{avg}$  of 63 is obtained, with the highest improvement being 11%. A degradation of up to 26% is observed for local cooling when the  $s/d$  value is maximum. With an increased  $s/d$  value, the degradation in  $Nu_{avg}$  increases, as the SJ flow field is disturbed by the presence of the flaps, and all the jet flow momentum cannot reach the target surface. Also, as the flap is farther from the plate, the turbulence induced by the vibrating flaps cannot significantly affect the heat transfer at the surface positively.

Fig. 4.5 displays heat transfer characteristics when the two flaps are at R2. Figs. 4.5(a) and 4.5(b) show the magnitude of  $Nu_{avg}$  and the percentage change observed in spot cooling, respectively, compared to the conventional SJ across different combinations of  $z/d$  and  $h/d$  values. A maximum  $Nu_{avg}$  value near 97 is obtained at  $h/d=2.5$ ,  $z/d=3.5$  and  $h/d=1.5$ ,

$z/d=2.5, 3$ . A maximum enhancement of 46% compared to the conventional SJ is found at  $h/d=1.5, z/d=3$ . Relatively

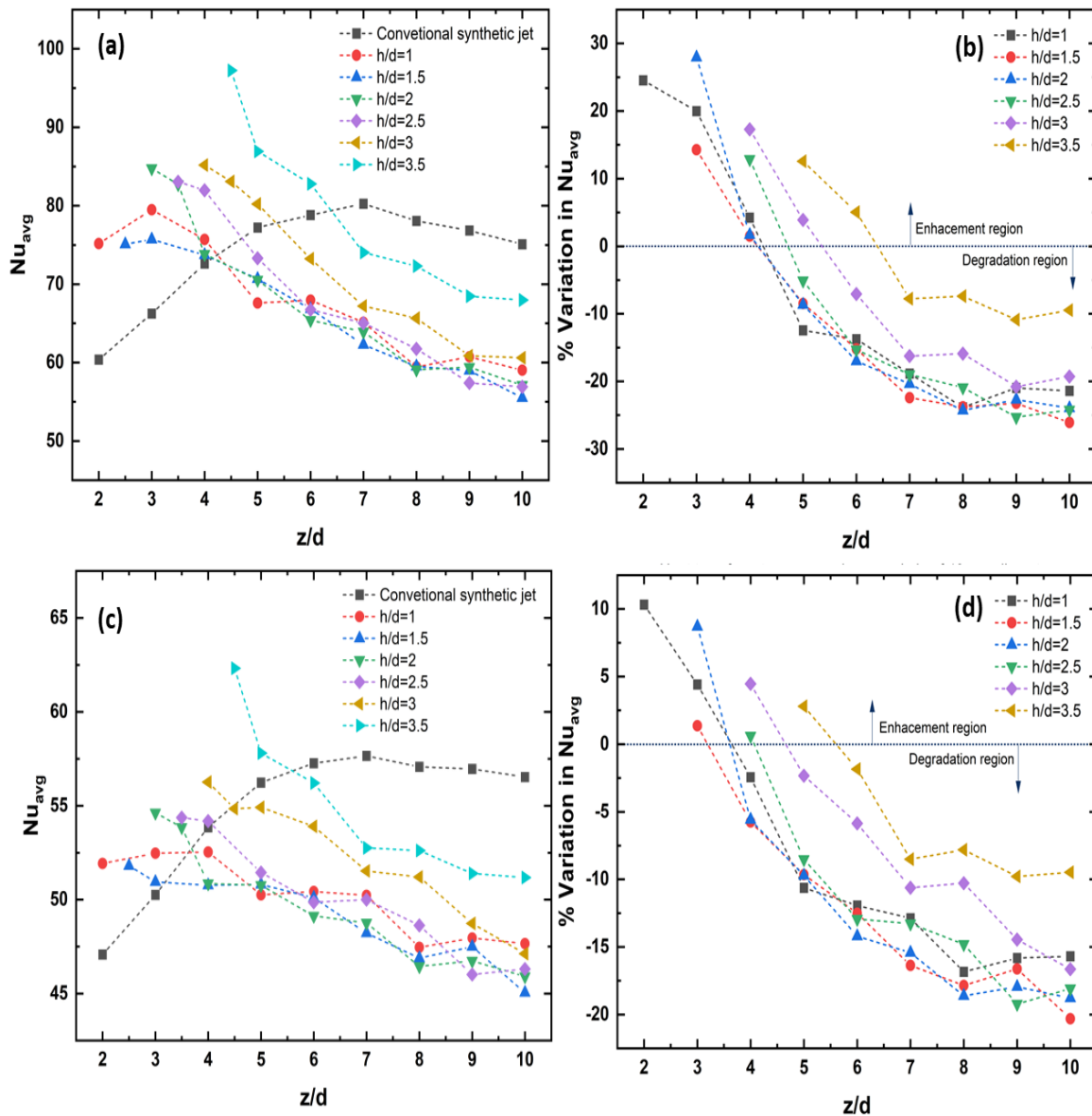


Fig. 4.4: Heat transfer rates of the SJ with piezoelectric flaps at different combinations of  $z/d$  and  $h/d$  value for W8 two strips at radial location R3.5  $Nu_{avg}$  at spot cooling circle of (a) 40mm dia ( $r/d=1$ ) and wide area cooling (c) 160 mm dia. ( $r/d=4$ ), % enhancement in  $Nu_{avg}$  at (b) ( $r/d=1$ ) and (d) ( $r/d=4$ ) compared to conventional SJ.

higher enhancements in  $Nu_{avg}$  are found at lower  $z/d$  ( $<4$ ) than R3.5 and R5 cases. A possible reason is that the flaps are relatively close to the jet centreline and can produce larger vibration amplitudes, improving the connection between the flaps and the surface. Figs. 4.5(c) and 4.5(d) illustrate the  $Nu_{avg}$  magnitude and the percentage change observed for wide area cooling, respectively, compared to the conventional SJ across various

combinations of  $z/d$  and  $h/d$  values. The R2 case exhibits the most improvement (up to 23%) in  $Nu_{avg}$  for a wider area than the other two. Additionally, the largest deterioration in  $Nu_{avg}$  occurs with increased obstruction to the SJ, as seen in the R2 case. The heat transfer's degradation ( $\sim 30\%$ ) is observed at  $h/d=2, 2.5, 3$ , and  $z/d=10$  for spot cooling.

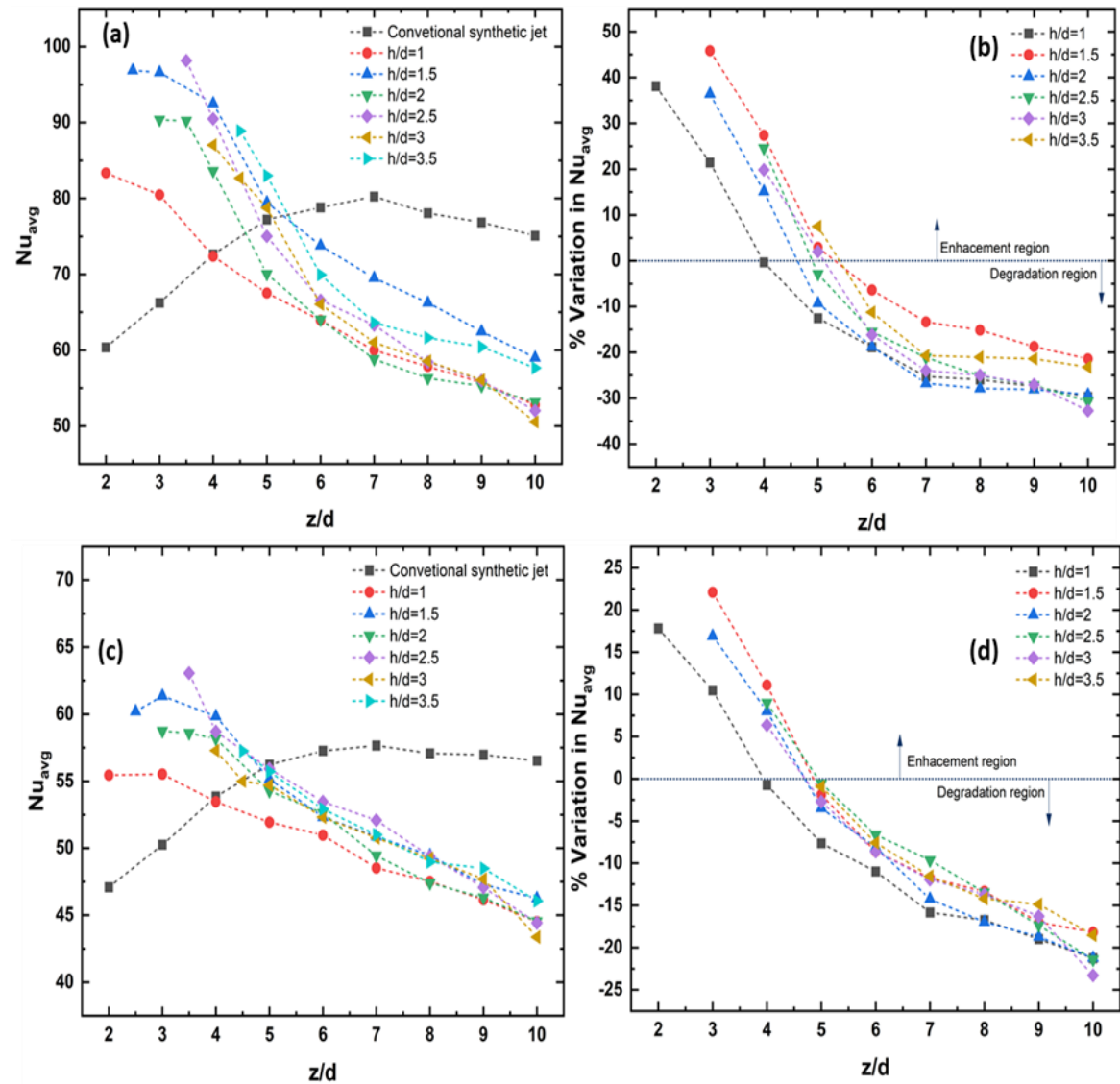


Fig. 4.5: SJ with piezoelectric flaps heat transfer at various combinations of  $z/d$  and  $h/d$  for W8 two strips at radial location R2  $Nu_{avg}$  at (a) spot cooling circle of 40 mm dia ( $r/d=1$ ) and (c) wide area cooling circle 160 mm dia. ( $r/d=4$ ), % enhancement in  $Nu_{avg}$  at (b) ( $r/d=1$ ) and (d) ( $r/d=4$ ) as compared to conventional SJ

Interestingly, a maximum enhancement at a particular  $z/d$  ( $< 6$ ) value is observed when the  $s/d$  value is between 1 and 1.5. Thus, when the flaps and the heated surface are close to each other, the vibrating motion of the flaps improves the forced convection heat transfer with higher mixing and imparts a sudden movement over a heated plate, which removes

heated air from a heated surface. As the gap between these two increases to a higher value, the turbulence levels near the heated surface decrease, reducing the heat transfer. Thus, the turbulence induced by the fluctuating motion of the flaps positively impacts the heat transfer rates when the flaps and the surface are closely spaced. Maximum vibrations in the flaps are assumed to be produced when the highest force is pointed towards the leading-edge area, resulting in a higher bending moment. When the flaps are at R5, they are relatively far away from the jet centreline compared to R3.5 and R2 cases. Hence, when the flap placement ( $h/d$ ) is farther from the jet orifice, the R5 produces the highest values of heat transfer. It happens as the jet spreads wider in the radial direction, imparting a higher force when the flaps are farther away from the centreline. However, in R5, we get maximum heat transfer at higher  $z/d$  than in R2. The reason is the opening of the orifice 10 mm, supported by a conventional SJ at higher  $z/d$  and strip movement. This shows that if we increase the radial distance from the centreline of the jet, the orifice opens more, and the result shows a trend like a conventional SJ but with an increment in heat transfer. At lower values of  $h/d$ , the maximum values are obtained for R2, as the jet has yet to spread radially and has a stronger flow structure near the jet centreline area.

Fig. 4.6 displays heat transfer characteristics when the two flaps are W4 and located at R2. Figs. 4.6(a) and 4.6(b) show the magnitude of  $Nu_{avg}$  and the percentage change observed in spot cooling, respectively, compared to the conventional SJ across different combinations of  $z/d$  and  $h/d$  values. A maximum  $Nu_{avg}$  value near 95 is obtained at  $h/d=1.5$ ,  $z/d=2.5$  and  $h/d=2.5$ ,  $z/d=3.5$ , 3. A maximum enhancement of 41% compared to the conventional SJ is found at  $h/d=1.5$ ,  $z/d=3$ . Figs. 4.6(c) and 4.6(d) illustrate the  $Nu_{avg}$  magnitude and the percentage change observed for wide area cooling, respectively, compared to the conventional SJ across various combinations of  $z/d$  and  $h/d$  values. The R2 case exhibits the most improvement (up to 23%) in  $Nu_{avg}$  for a wider area than the other two. Additionally, the largest deterioration in  $Nu_{avg}$  occurs with increased obstruction to the SJ, as seen in the R2 case. The heat transfer's degradation (~30%) is observed at  $h/d=2$ , 2.5, 3, and  $z/d=10$  for spot cooling.

Fig. 4.7 displays heat transfer characteristics when the two flaps are W4 at R5. Figs. 4.7(a) and 4.7(b) show the magnitude of  $Nu_{avg}$  and the percentage change observed in spot cooling, respectively, compared to the conventional SJ across different combinations of  $z/d$  and  $h/d$  values. A maximum  $Nu_{avg}$  value near 90 is obtained at  $h/d=3.5$ ,  $z/d=4.5$ . A maximum enhancement of 21% compared to the conventional SJ is found at  $h/d=3.5$ ,

$z/d=4.5$ . Figs. 4.7(c) and 4.7(d) illustrate the  $Nu_{avg}$  magnitude and the percentage change observed for wide area cooling, respectively, compared to the conventional SJ across various combinations of  $z/d$  and  $h/d$  values. The R5 case exhibits an improvement of up to 10%, which is a minimal improvement compared to other strips. In this case, the orifice opens more because the W4 strip at radial location R5 occupies a minimal area over an orifice. Additionally, the least deterioration in  $Nu_{avg}$  occurs with decreased obstruction to the SJ, as seen in the R5 case. The heat transfer's degradation ( $\sim 15\%$ ) is observed at  $h/d=2, 2.5, 3$ , and  $z/d=10$  for spot cooling.

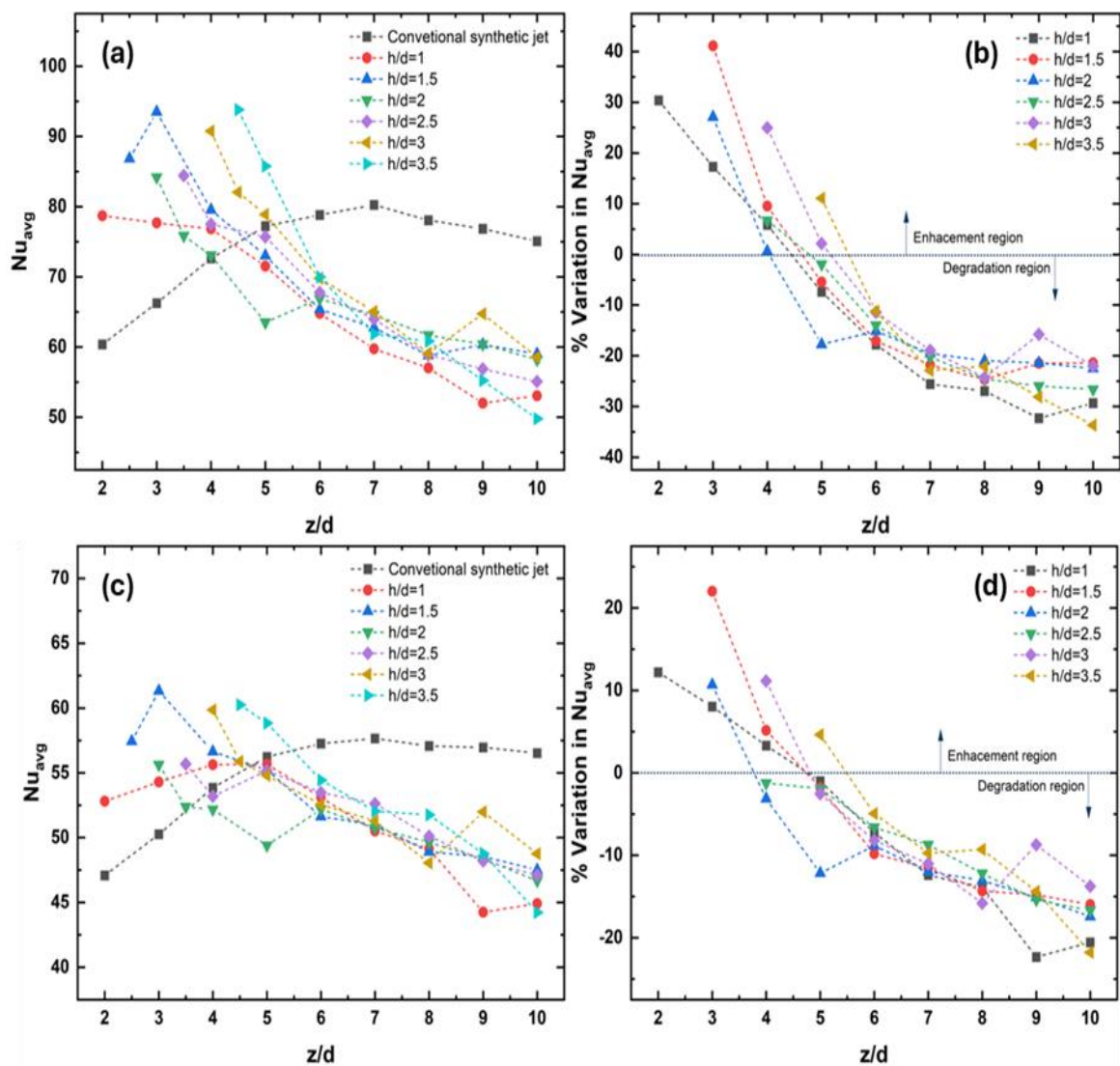


Fig. 4.6: SJ with piezoelectric flaps heat transfer at various combinations of  $z/d$  and  $h/d$  for W4 two strips at radial location R2  $Nu_{avg}$  at (a) spot cooling circle of 40 mm dia ( $r/d=1$ ) and (c) wide area cooling circle 160 mm dia. ( $r/d=4$ ), % enhancement in  $Nu_{avg}$  at (b) ( $r/d=1$ ) and (d) ( $r/d=4$ ) as compared to conventional SJ.

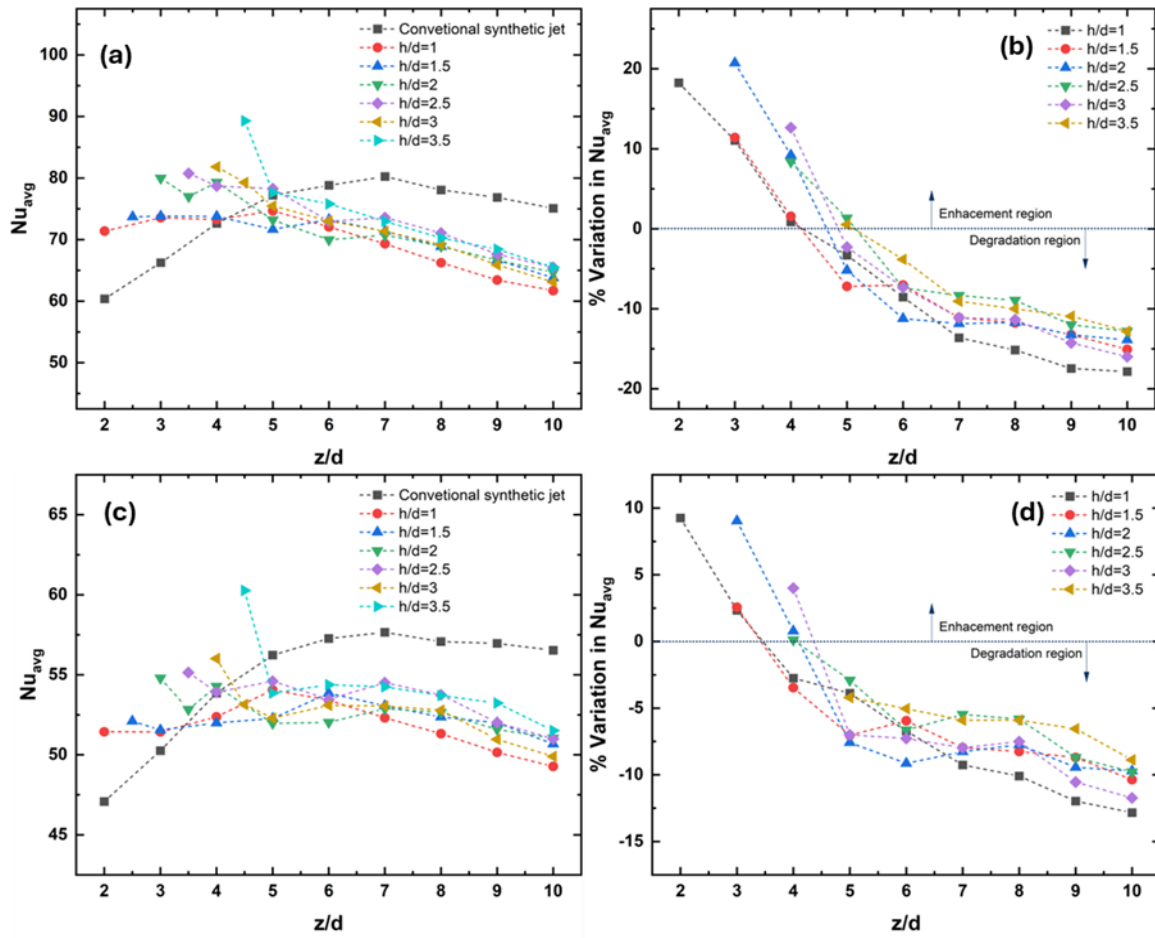


Fig. 4.7: SJ having two piezoelectric flaps heat transfer rates at various  $z/d$  and  $h/d$  combinations for W4 at radial location R5  $Nu_{avg}$  at (a) spot cooling circle of 40mm dia. ( $r/d=1$ ) and (c) wide area cooling circle 160 mm dia. ( $r/d=4$ ), % enhancement in  $Nu_{avg}$  at (b) ( $r/d=1$ ) and (d) ( $r/d=4$ ) than conventional SJ.

Fig. 4.8 displays heat transfer characteristics when the flaps are W12 and located at R5. Figs. 4.8(a) and 4.8(b) show the magnitude of  $Nu_{avg}$  and the percentage change observed in spot cooling, respectively, compared to the conventional SJ across different combinations of  $z/d$  and  $h/d$  values. A maximum  $Nu_{avg}$  value near 98 is obtained at  $h/d=3.5$ ,  $z/d=4.5$ . A maximum enhancement of 32% compared to the conventional SJ is found at  $h/d=3.5$ ,  $z/d=4.5$ . Figs. 4.8(c) and 4.8(d) illustrate the  $Nu_{avg}$  magnitude and the percentage change observed for wide area cooling, respectively, compared to the conventional SJ across various combinations of  $z/d$  and  $h/d$  values. The R5 case exhibits an improvement of up to 17%. For the W12 strip and radial location R5, this flap arrangement for a rectangle orifice  $12 \times 10$  at  $h/d=1$  shows heat transfer characteristics as shown in the literature [50], like a conventional SJ with a rectangle orifice but improved heat transfer characteristics.

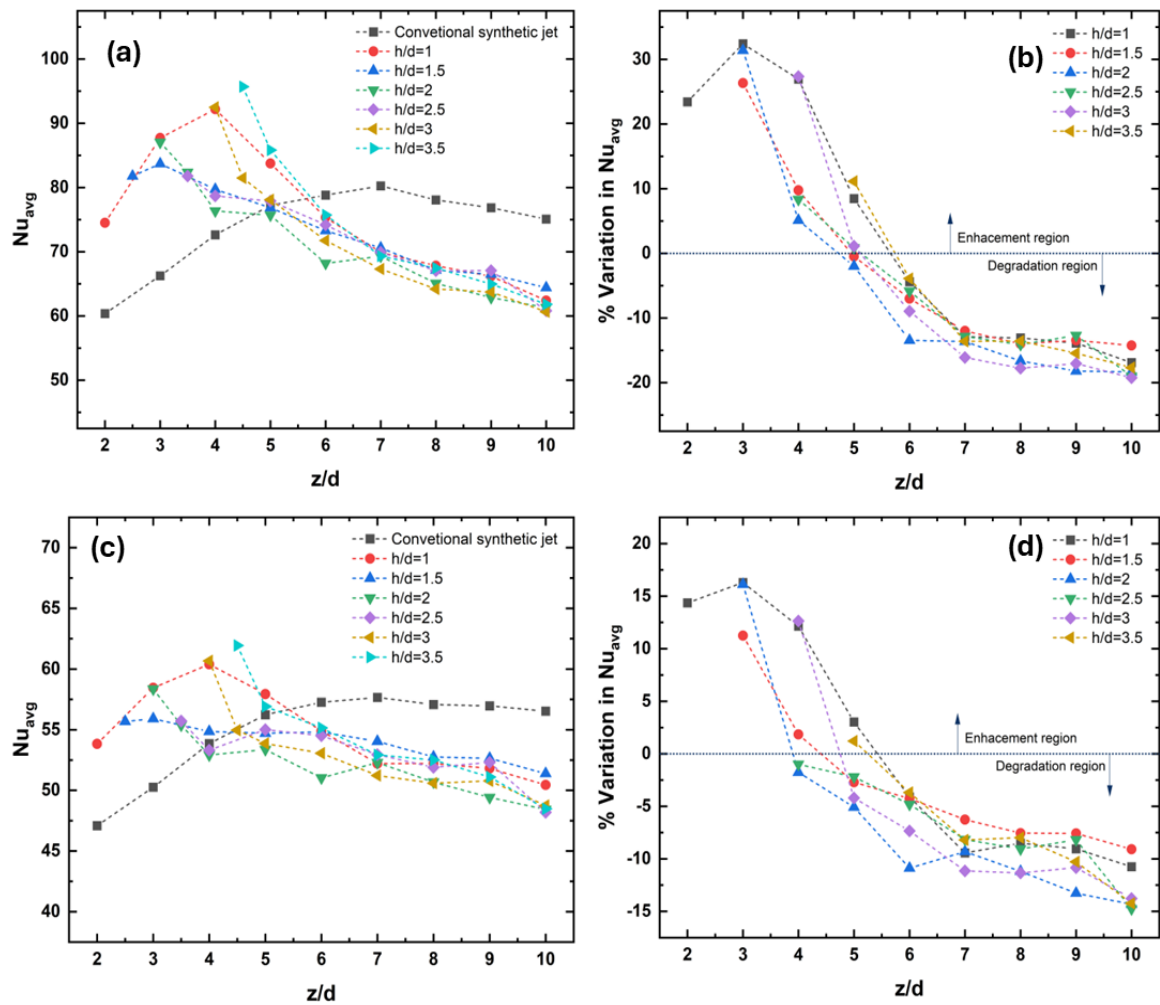


Fig. 4.8: SJ having two piezoelectric flaps heat transfer rates at various  $z/d$  and  $h/d$  combinations for W12 at radial location R5  $Nu_{avg}$  at (a) spot cooling circle of 40mm dia. ( $r/d=1$ ) and (c) wide area cooling circle 160 mm dia. ( $r/d=4$ ), % enhancement in  $Nu_{avg}$  at (b) ( $r/d=1$ ) and (d) ( $r/d=4$ ) than conventional SJ.

Fig. 4.9 displays heat transfer characteristics when the flaps are W12 and located at R2. Figs. 4.9(a) and 4.9(b) show the magnitude of  $Nu_{avg}$  and the percentage change observed in spot cooling, respectively, compared to the conventional SJ across different combinations of  $z/d$  and  $h/d$  values. A maximum  $Nu_{avg}$  value near 102 is obtained at  $h/d=3$ ,  $z/d=4$ . A maximum enhancement of 41% compared to the conventional SJ is found at  $h/d=3$ ,  $z/d=4$ . Figs. 4.9(c) and 4.9(d) illustrate the  $Nu_{avg}$  magnitude and the percentage change observed for wide area cooling, respectively, compared to the conventional SJ across various combinations of  $z/d$  and  $h/d$  values. The R2 case exhibits an improvement of up to 22%. At  $h/d=3$ , the value of the Nu is around 102, and its nearby value is around 90. This might be considered uncertain in the experiment because, at the W12 strip and

radial location R2, most of the orifice is covered by a strip; that is the reason heat transfer may be decreased.

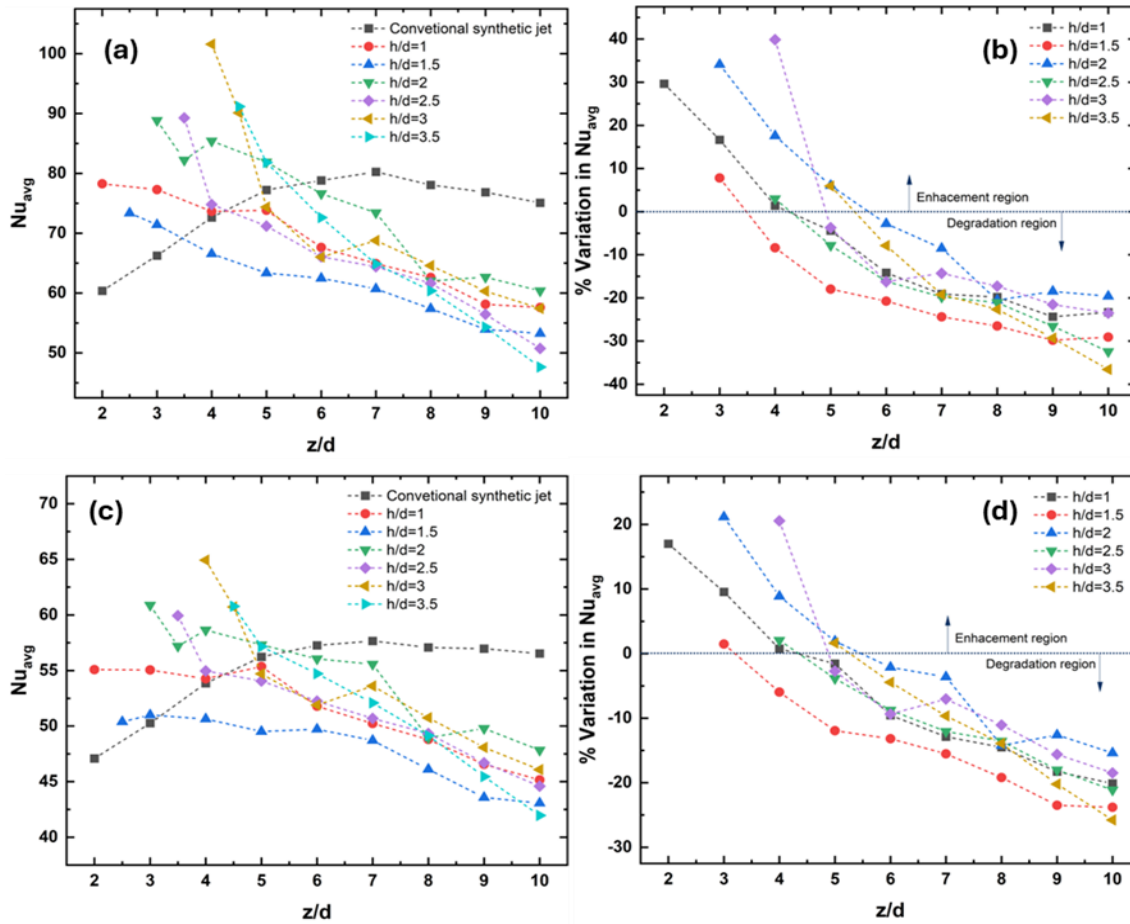


Fig. 4.9: Heat transfer rates of SJ consist of two piezoelectric flaps at different  $z/d$  and  $h/d$  values for W12 at radial location R2  $Nu_{avg}$  at (a) spot cooling circle of 40 mm dia ( $r/d=1$ ) and (c) wide area cooling circle 160 mm dia ( $r/d=4$ ); % enhancement in  $Nu_{avg}$  at (b) ( $r/d=1$ ) and (d) ( $r/d=4$ ) than conventional SJ.

#### 4.1.3. The SJ with four piezoelectric flaps.

SJ with piezoelectric flaps: Throughout the experiment, we use a circular orifice with a diameter of 20mm; as per the orifice opening, only W8 and W4 strips are arranged at radial locations R5 in four strip configurations. Fig. 4.10 displays heat transfer characteristics for four flaps of W8, and it is located at R5. Figs. 4.10(a) and 4.10(b) show the magnitude of  $Nu_{avg}$  and the percentage change observed in spot cooling, respectively, compared to the conventional SJ across different combinations of  $z/d$  and  $h/d$  values. A maximum  $Nu_{avg}$  value near 98 is obtained at  $h/d=1.5, 2, 2.5, z/d=2.5, 3, 3.5$ . A maximum enhancement of 48% compared to the conventional SJ is found at  $h/d=2.5, z/d=3.5$ . Figs. 4.10(c) and 4.10(d)

illustrate the  $Nu_{avg}$  magnitude and the percentage change observed for wide area cooling, respectively, compared to the conventional SJ across various combinations of  $z/d$  and  $h/d$  values. The R5 case exhibits an improvement of up to 15%. At  $h/d=3$ . In four four-strip configurations, most enhancement in heat transfer was obtained at  $r/d=1$  because the influence of four strips in this region is very high. At  $r/d=4$ , heat transfer enhancement is very low because most of the fluid is blocked by four strips.

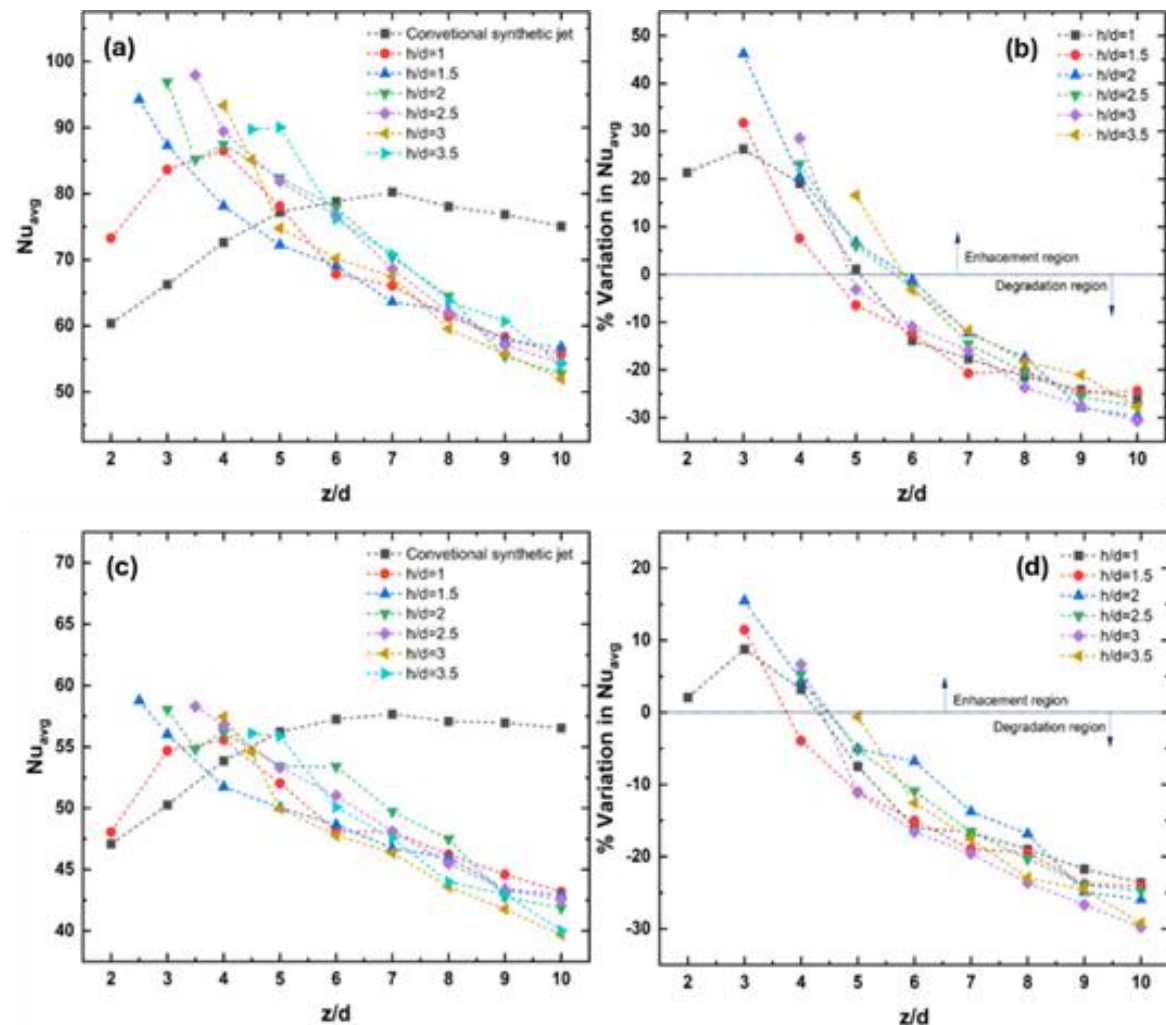


Fig. 4.10: Heat transfer rates of SJ consist of four piezoelectric flaps at different  $z/d$  and  $h/d$  values for W8 at radial location R5  $Nu_{avg}$  at (a) spot cooling circle of 40 mm dia ( $r/d=1$ ) and (c) wide area cooling circle 160 mm dia ( $r/d=4$ ); % enhancement in  $Nu_{avg}$  at (b) ( $r/d=1$ ) and (d) ( $r/d=4$ ) than conventional SJ.

Fig. 4.11 displays heat transfer characteristics for four flaps of W4, and it is located at R5. Figs. 4.11(a) and 4.11(b) show the magnitude of  $Nu_{avg}$  and the percentage change observed in spot cooling, respectively, compared to the conventional SJ across different combinations of  $z/d$  and  $h/d$  values. A maximum  $Nu_{avg}$  value near 100 is obtained at

$h/d=3.5$ ,  $z/d=4.5$ . A maximum enhancement of 34% compared to the conventional SJ is found at  $h/d=3.5$ ,  $z/d=4.5$ . Figs. 4.11(c) and 4.11(d) illustrate the  $Nu_{avg}$  magnitude and the percentage change observed for wide area cooling, respectively, compared to the conventional SJ across various combinations of  $z/d$  and  $h/d$  values. The R5 case exhibits an improvement of up to 8% at  $h/d=3.5$ . In the four-strip configuration, most enhancement in heat transfer is obtained at  $r/d=1$  because the influence of four strips in this region is very high. At  $r/d=4$ , heat transfer enhancement is very low because most of the fluid is blocked by four strips. If we compare the four strips, W8 and W4, heat transfer enhancement in the W8 strip at lower  $h/d$ , but in the W4 strip, heat transfer enhancement is achieved at higher  $h/d$ . Because the orifice opens more in the W4 strip, and the result shifted toward a conventional SJ.

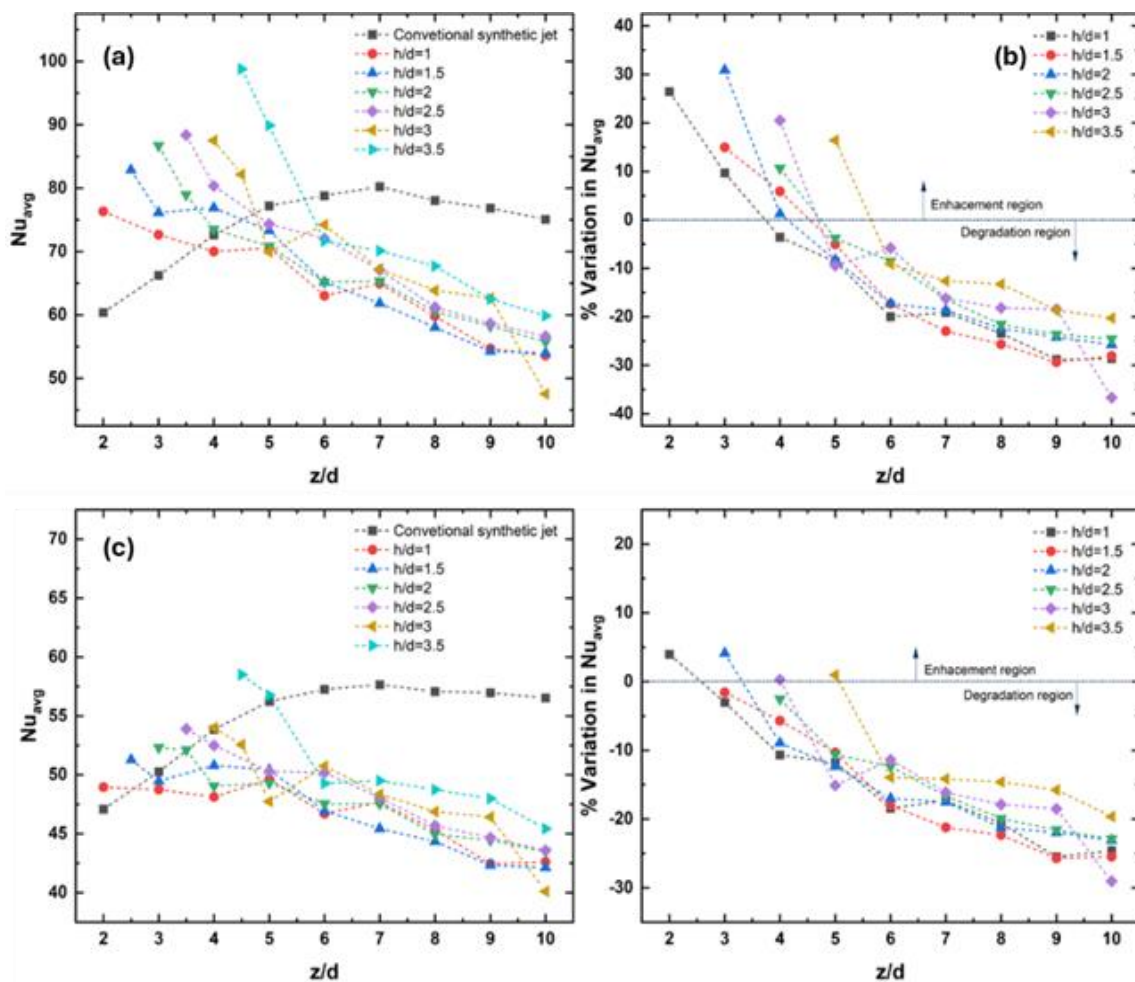


Fig. 4.11: Heat transfer rates of SJ consist of four piezoelectric flaps at different  $z/d$  and  $h/d$  values for W4 at radial location R5  $Nu_{avg}$  at (a) spot cooling circle of 40 mm dia ( $r/d=1$ ) and (c) wide area cooling circle 160 mm dia ( $r/d=4$ ); % enhancement in  $Nu_{avg}$  at (b) ( $r/d=1$ ) and (d) ( $r/d=4$ ) than conventional SJ.

#### 4.1.4. Nu contours

The Nu variation over the heated surface is shown here to obtain more insights into the thermal performance. The radial location of the flaps has a vital effect on the Nu distribution over the surface. The gap between the two flaps makes an orifice-like structure called a secondary orifice. For the R5 case, the gap is 10 mm, and the flap's leading edge is 8 mm. Thus, it creates a rectangular opening with an aspect ratio of 1.25. The aspect ratio is the ratio of the length of the major axis to the minor axis. The aspect ratio for R3.5 and R2 cases is 1.14 and 2, respectively (refer to Fig. 4.12). Thus, the SJ passing through this opening creates a different flow structure from the circular orifice. The difference between  $z/d$  and  $h/d$  (the distance between the flaps and the target plate) is referred to here as  $s/d$ .

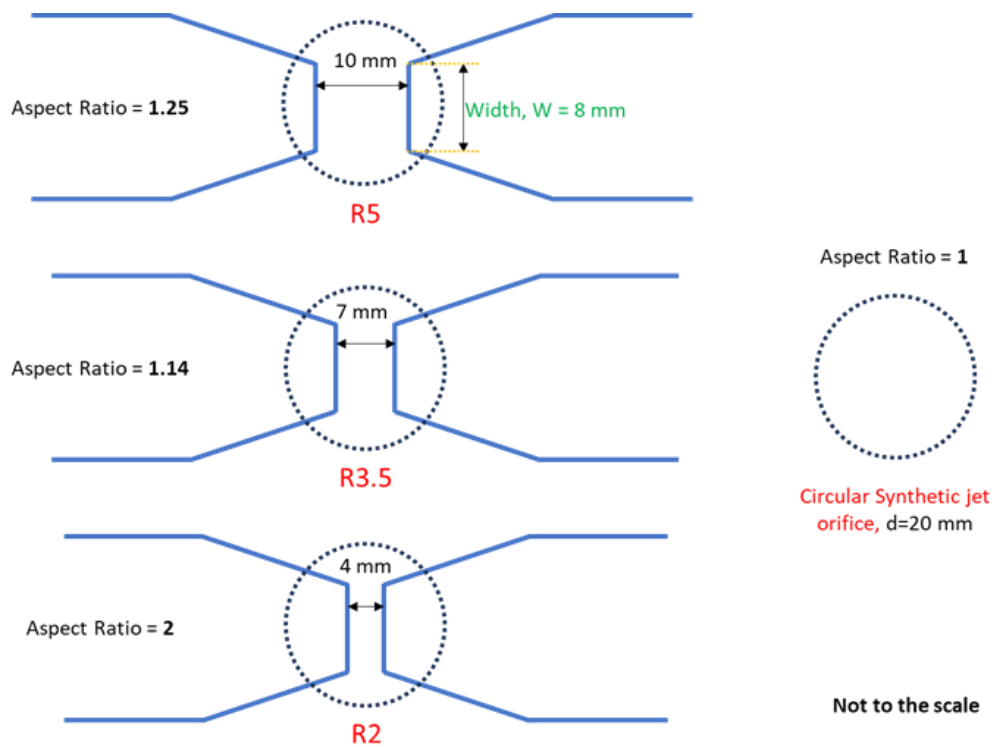


Fig. 4.12: Orifice and flap (width,  $w=8$  mm) configurations used in the current set of experiments

Fig. 4.13 shows Nu contours at  $s/d=1.5$  at a relatively lower  $z/d=3$ . The R2 case with a higher aspect ratio provides better stagnation region heat transfer characteristics, followed by the R5 and R3.5 cases. Because of the opening shape between the flaps, the contour of the Nu takes on a rectangular form around the stagnation region in the flap case, in contrast to the conventional SJ. The SJ with piezoelectric flaps performs better than the conventional one for all radial locations. However, the maximum increase in heat transfer with

piezoelectric flaps occurs at different  $h/d$  for the R2 radial location, with the maximum increase in heat transfer at lower  $h/d$  and R5 at higher  $h/d$ .

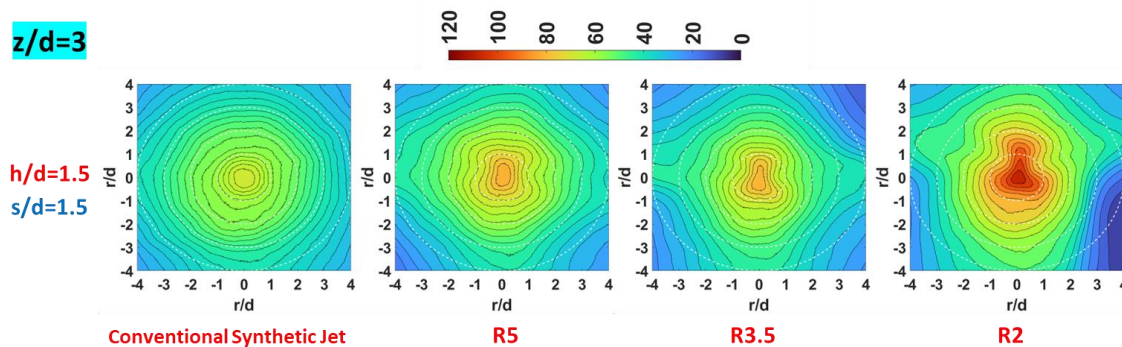


Fig. 4.13: The Nu contours at  $h/d=1.5$  and  $z/d=3$

At an intermediate  $z/d=5$  and  $7$ , the variation to different  $h/d$  values is shown in Fig. 4.14. The rectangular shape of the Nu contours is still evident at all  $s/d$  values. The R2 case creates distinct peaks away from the stagnation point due to the higher aspect ratio. The stagnation point Nu is lower at  $z/d=7$  compared to  $z/d=5$ , but the average Nu is high. It happens due to increased heat transfer in the wall jet region (away from the stagnation point) due to higher mass impingement due to enhanced entrainment. It overpowers the reduction in the stagnation region, resulting in overall better  $Nu_{avg}$  at  $z/d=7$ .

At a greater orifice-to-surface spacing,  $z/d=10$ , the stagnation point Nu decreases compared to others due to a notable decline in the centreline velocity of the impinging jet (shown in Figs. 4.15 and 4.16). Although heat transfer in the wall jet region is enhanced, it is insufficient to overcome the reduction in the stagnation region, resulting in a lower  $Nu_{avg}$  at  $z/d=10$  than at  $z/d=7$ . Additionally, the secondary peaks disappear as  $z/d$  increases, attributed to reduced turbulence induced by the vibrating flaps. At  $z/d=10$ , the highest degradation in Nu with piezoelectric flap, as shown in Fig. 4.17. The reason is that SJ gives their moment to piezoelectric flaps and high-momentum piezoelectric flaps vibrate near the heated surface. Which removes heated air from a surface, but for  $z/d=10$ , these piezoelectric flaps are far from a heated surface, so jet movement does not reach that location. At lower  $z/d$  values, the heat transfer does not start decreasing even if a flap is far from the jet centerline, as the jet is still in the potential core region, retaining the maximum momentum. At higher  $z/d$ , the jet has already somewhat decayed; thus, the heat transfer starts decreasing even if the flap is away.

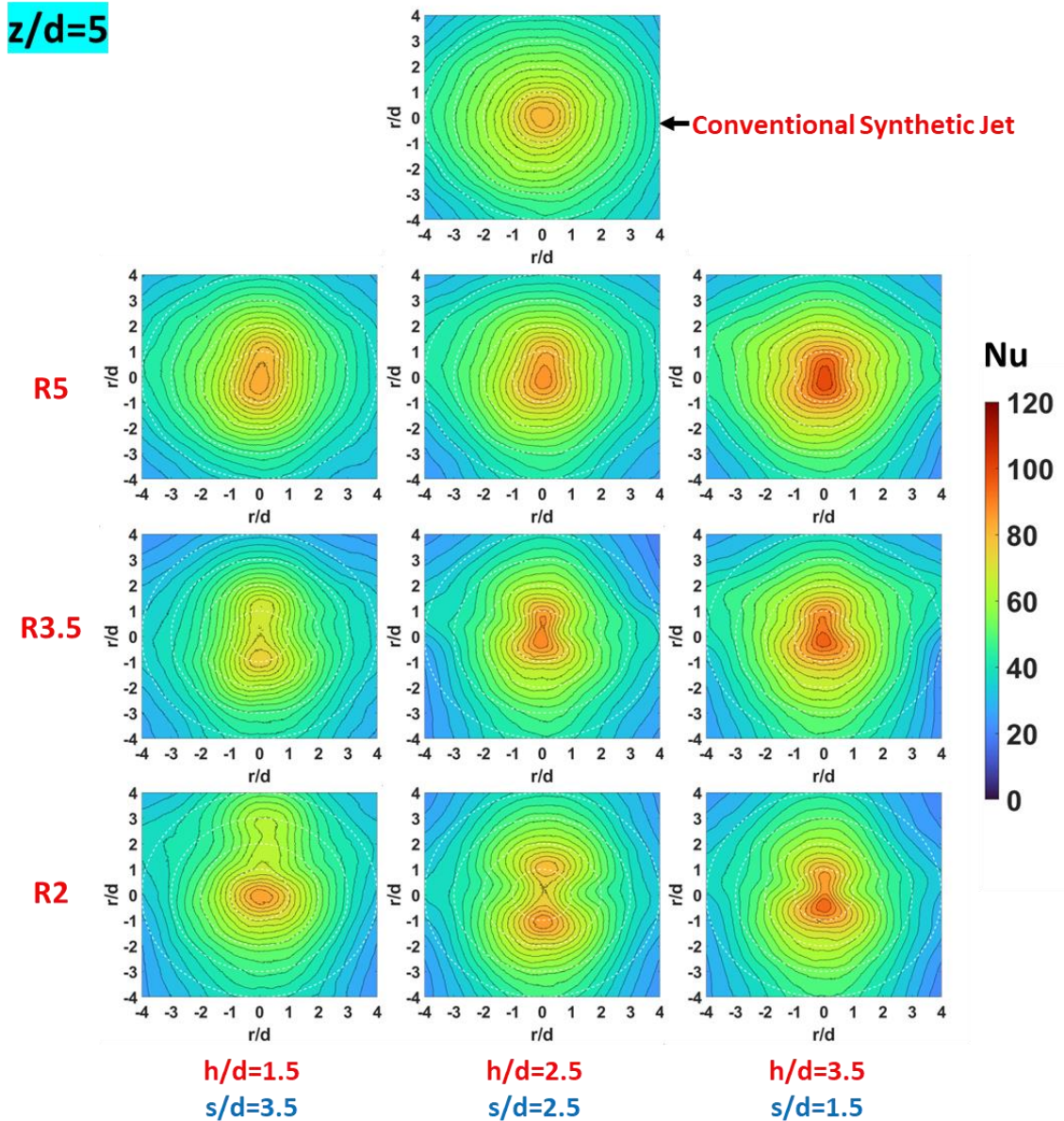


Fig. 4.14: The Nu contours at  $z/d=5$

Thus, by changing the radial position of the flaps, the heat transfer rates for various combinations of  $h/d$  and  $z/d$  values are found. The behavior of the  $Nu_{avg}$  depends on the difference between  $h/d$  and  $z/d$  values and the radial location of the flaps from the center. Up to 46% enhancement for the spot cooling and up to 22% for wide area cooling is achieved by incorporating the flaps for the W8 flap at radial location R8.

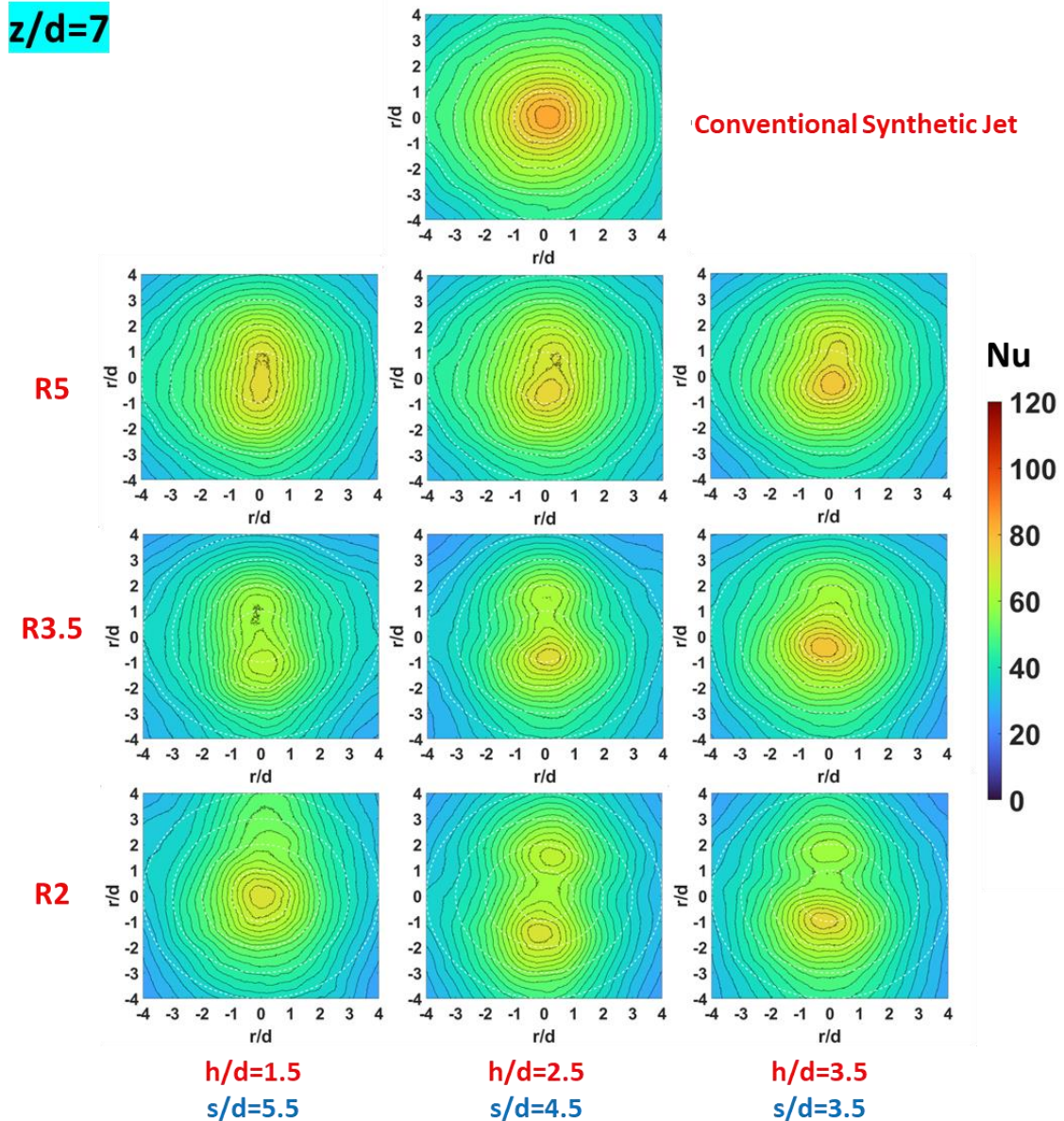


Fig. 4.15: Contours plots at  $z/d=7$  for Nu.

Fig. 4.17 shows a heat transfer visualization through Nu contour for different configurations; in these, for the same  $z/d$  and same  $h/d$ , the value of Nu is higher for the SJs with piezoelectric flaps as compared to piezoelectric flaps, the reason already discussed above paragraphs. If we compare two strips and four strips at  $r/d=1$  region, higher heat transfer is achieved for the strips configuration because four strips impart higher movement over a heated surface as compared to two flaps, but for  $r/d=4$  region, higher heat transfer is achieved through two strip configurations because higher space available between a strip to reach a fluid in  $r/d=4$  region as compared to four strips.

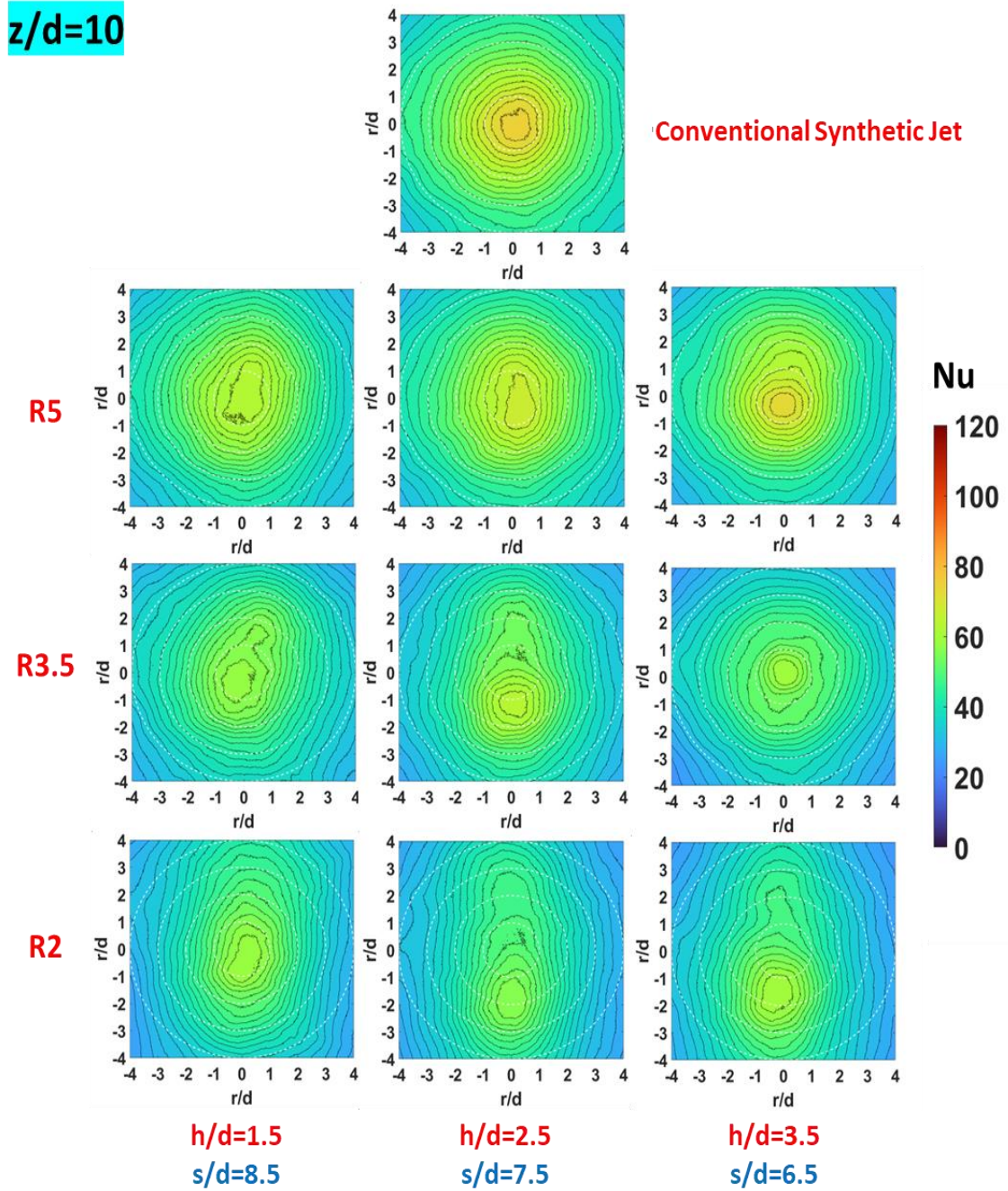


Fig. 4.16: Contours plots at  $z/d=10$  for Nu.

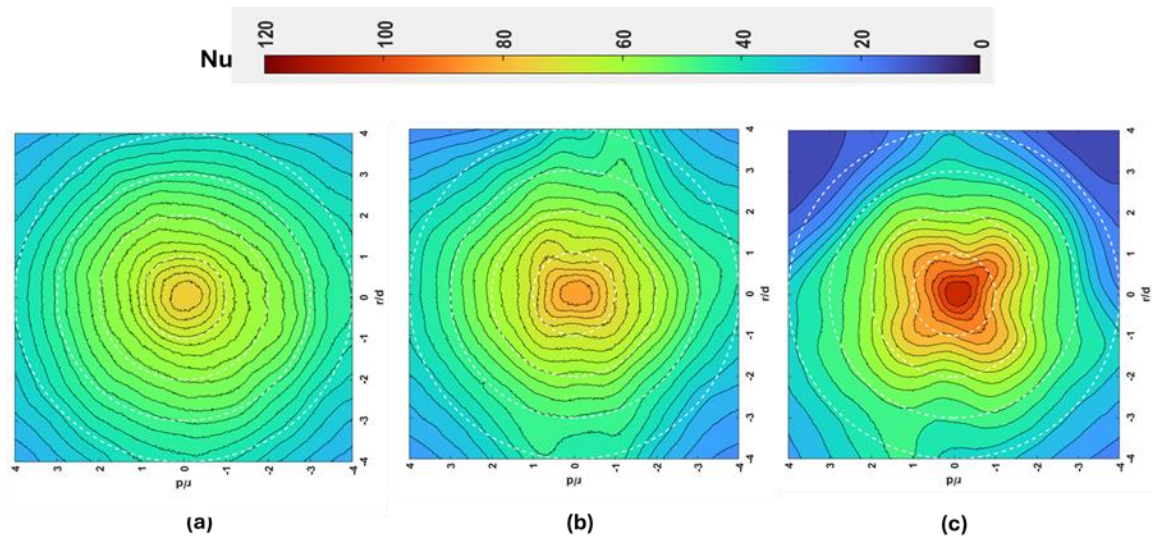


Fig. 4.17: Heat transfer visualization through Nu contour for different configurations at  $z/d=3$ ,  $h/d=2$  (a) without strip SJ (b) SJ with two flaps W8R5 (c) SJ with four flaps W8R5

## 4.2. Energy harvesting using SJ with piezoelectric flaps.

In the preceding section, we observed that utilizing synthetic flaps with flaps improved heat transfer rates. Additionally, we could harness voltage by incorporating piezoelectric material onto these flaps. As the SJ flow interacts with the flap, it induces vibrations, and piezoelectric material enables voltage generation through the piezoelectric effect.

### 4.2.1 Effect of the resistance for the voltage ( $V_{rms}$ ) measurement.

The value of the voltage measured varies with the value of the resistance connected in a circuit. The voltage is measured from the vibrating piezoelectric flap across the various resistance values (0.15-33 k $\Omega$ ) when placed at  $h/d=2$  to obtain optimum energy levels. The root mean square value of the voltage ( $V_{rms}$ ) is calculated from the signal acquired using data acquisition systems. A sampling rate of 1 ms is used while acquiring the voltage data. The impedance value of the piezoelectric material, as per the manufacturer, is near 200  $\Omega$ . We have obtained similar results as the resistance value changes, as shown in Fig. 4.18. The  $V_{rms}$  value decreases as we move away from the given impedance value of 200  $\Omega$ ; thus, 150  $\Omega$  resistance is used for further voltage measurement.

$$V_{rms} = \sqrt{\frac{\sum V_i^2}{N}} \quad i = 1 \text{ to } N \quad 4.1$$

Where  $V_i$  is the instantaneous voltage generated by the piezoelectric voltage,  $N$  is the number of data points acquired during the voltage measurement across 150  $\Omega$  resistance.

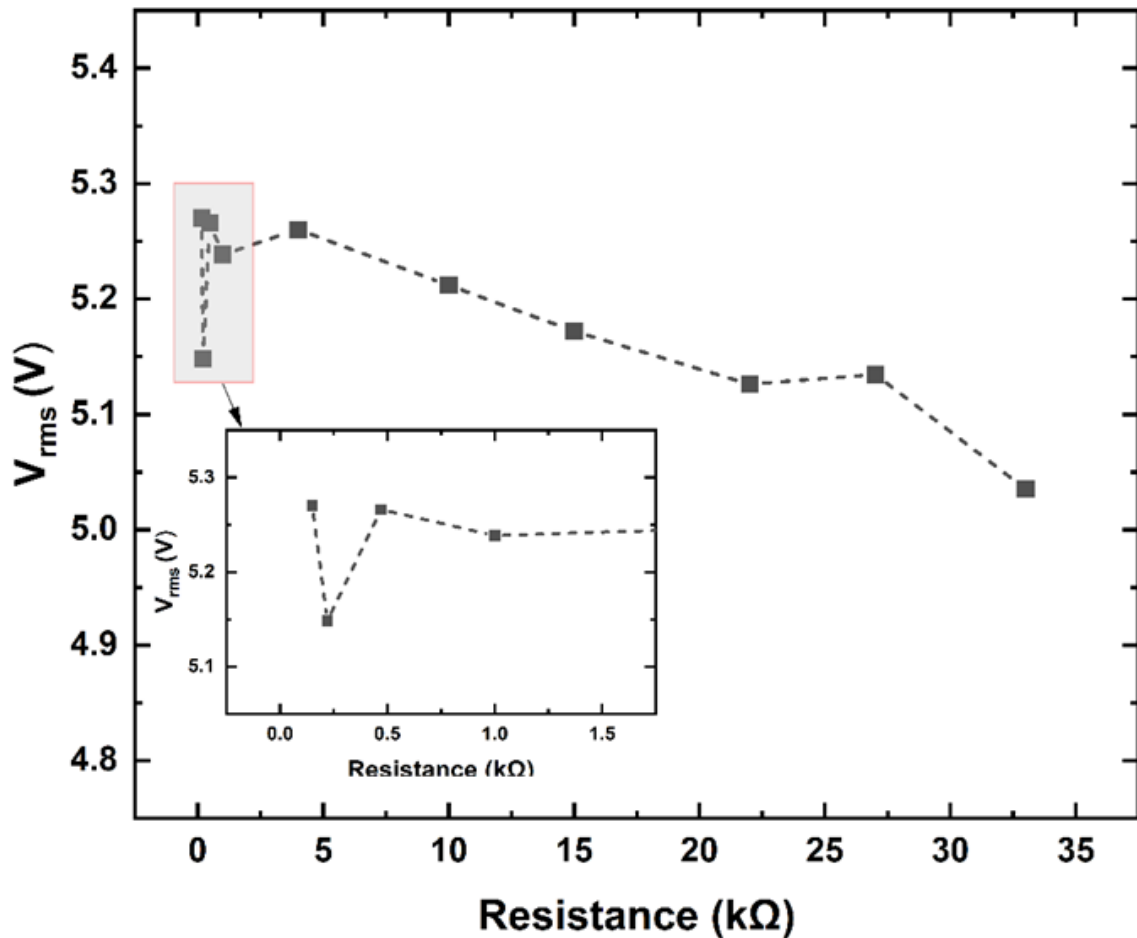


Fig. 4.18: Effect of the voltage generated from a single piezoelectric flap for different values of resistances.

#### 4.2.2 Effect of the orifice-to-flap spacing ( $h/d$ ) on the voltage ( $V_{rms}$ ) measurement.

With the change in the distance between the orifice exit and the flap, the pressure force applied on the flap differs, significantly affecting the voltage generation due to the piezoelectric effect. Fig. 4.19 shows the voltage signals acquired across  $150 \Omega$  resistance at different values of orifice-to-flap spacings ( $h/d$ ) for the R5 case. With the increase in the  $h/d$  value (like  $h/d=3.5$ ), the SJ has already spread in the radial direction with associated centreline velocity decay. Thus, the force applied by the impinging fluid on the leading edge of the flap reduces, thus generating a lower reaction force at the fixed end where the piezoelectric material is placed. It effectively reduces the voltage generated due to piezoelectricity. The peak-to-peak voltage decreases with increased  $h/d$  value. The effect of the radial location of the leading edge of the piezoelectric flap and the  $h/d$  values is discussed further.

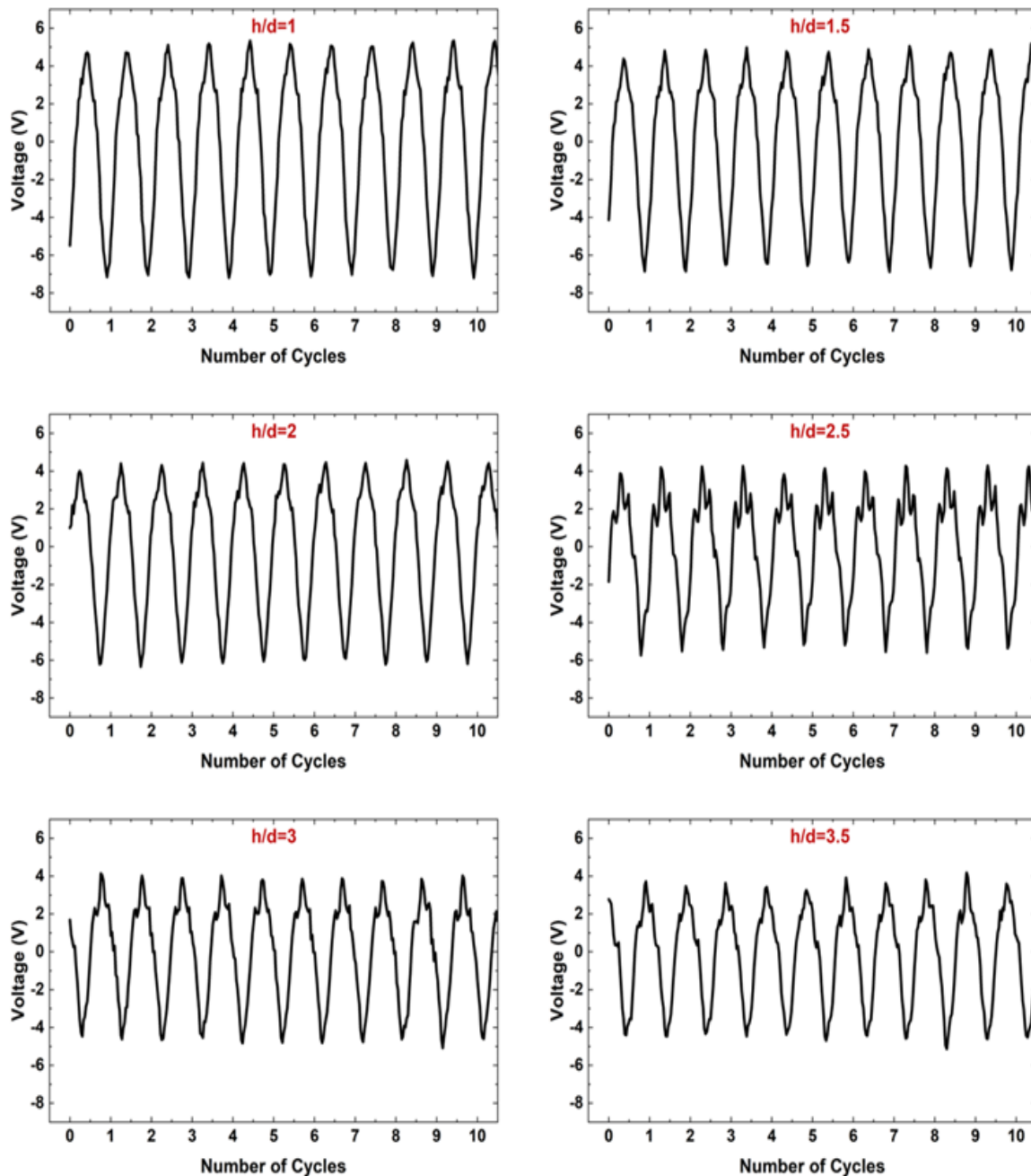


Fig. 4.19 Voltage signals acquired from a piezoelectric flap at different orifice-to-flap spacing.

#### 4.2.3 Effect of the radial location ( $R$ ) on the voltage ( $V_{\text{rms}}$ ) measurement

The radial location of the leading edge of the flaps is changed to see its effect on the heat transfer in the previous section. Here, the corresponding voltage generated at each measured condition is discussed. Fig. 4.20 illustrates  $V_{\text{rms}}$  and power ( $P$ ) and the percentage of energy harvested relative to the supplied power to the SJ actuator.

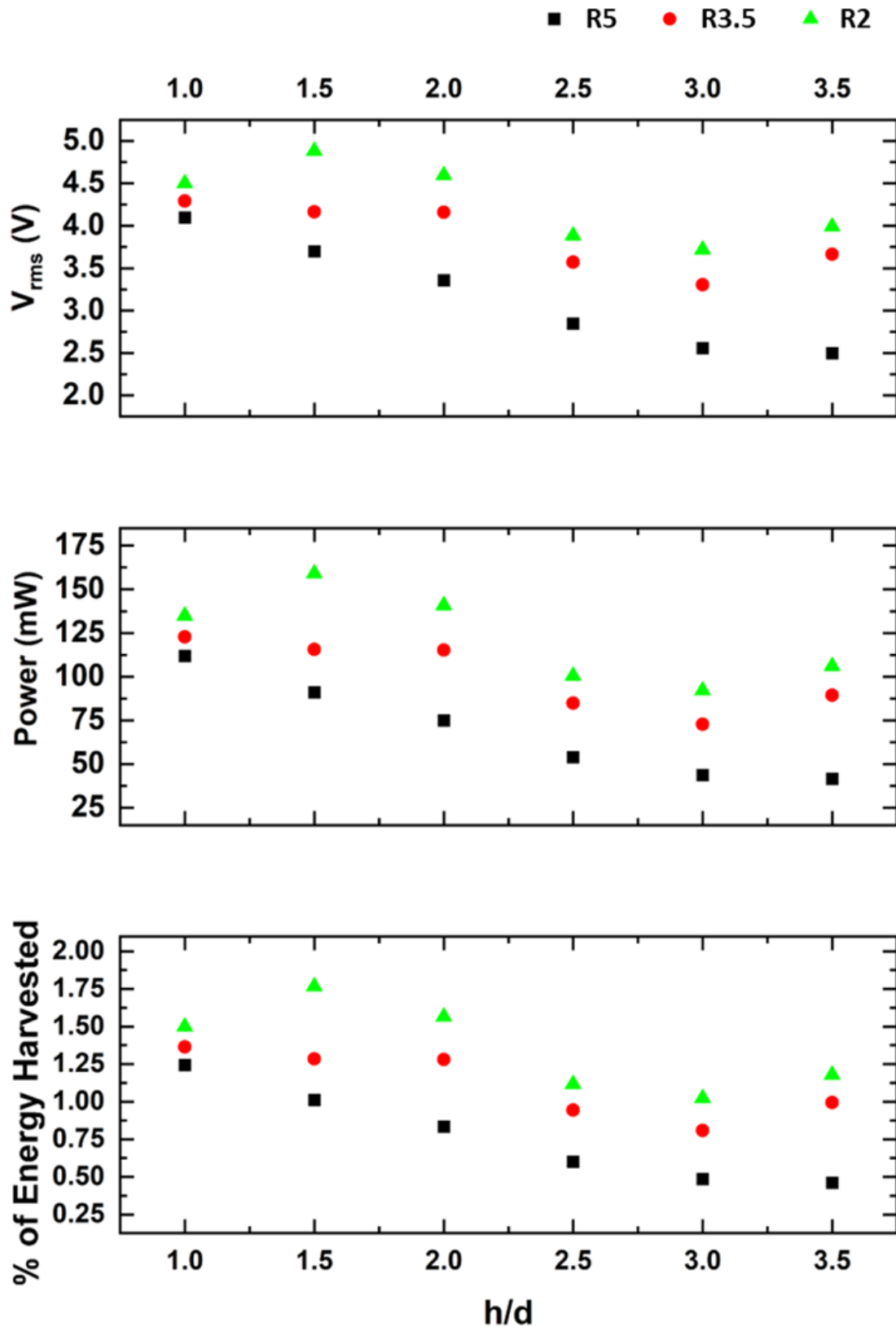


Fig. 4.20 Voltage, power generated, and the % of energy harvested from a single piezoelectric flap at  $h/d=1.5$  for three radial locations of the flap

These values are derived from a single piezoelectric flap, considering different radial locations of the flaps and orifice-to-flap spacings. The power generated from a single piezoelectric flap is calculated as follows:

$$\text{generated power from a single piezoelectric flap, } P = \frac{V_{rms}^2}{R} \quad 4.2$$

R is the resistance across which the voltage is measured, which has a magnitude of 150  $\Omega$ . The input provided to actuate the SJ acoustically is 10 V at 0.9 A, resulting in an input power ( $P_{in}$ ) of 9 W. The percentage of energy harvested is calculated based on the input power.

$$\% \text{ of energy harvested} = \frac{P}{P_{in}} \quad 4.3$$

For the R2 case, the  $V_{rms}$  value first reaches a peak at  $h/d=1.5$ , after that decreases with increasing  $h/d$  value, and again increases a little after  $h/d=3$ . The reason is that at higher  $h/d$ , large vortices hit piezoelectric flaps at radial location R2, and the space between a flap is much less than R5. The flaps are closer to the jet centreline; thus, a relatively large portion of the flap is directly under the influence of the potential core of the SJ. The centreline velocity increases more than the orifice exit velocity in the case of a SJ near 1.5 times the orifice diameter [63-64]; thus, it increases the voltage at  $h/d=1.5$ . For the other two cases, the flaps are farther from the jet centreline; thus, the same effect is not observed. As the flaps move further away from the orifice exit, the  $V_{rms}$  decrease with the decrease in the centreline velocity. The jet spreads quickly in the initial region [6], thus imparting enough momentum so that a little increase is observed for R2 and R3.5 cases, while it is not observed in R5 as it is farther away from that location. The reason is that R5 is sufficient between a strip, so large vortices escape from that space. However, in the R2 case, large vortices hit a flap due to less space, and voltage increases slightly. The  $V_{rms}$  value monotonically reduces for the R5 case for the abovementioned reasons.

#### **4.2.4. Effect of the supplied voltage to the SJ actuator on the voltage ( $V_{rms}$ ) measurement**

The Reynolds number ( $Re$ ) is fixed for the abovementioned experiments by fixing the operating frequency (31 Hz) and the voltage ( $V_{ac}=10$  V) supplied to the acoustic speaker at  $Re$  13000. The effect of the change in  $V_{ac}$  on the  $V_{rms}$  generation from a single piezoelectric flap is shown in 4.21. The experiments are carried out for R6.5 and  $h/d=1.5$ . Initially, when the supplied  $V_{ac}$  is low ( $<4$  V), the force of impinging SJ is not significant. Thus, the  $V_{rms}$

levels are on a very small scale. From that point onwards, the  $V_{rms}$  increase exponentially with an increasing  $V_{ac}$  value. However, the increment is reduced with equal enhancement in the supplied  $V_{ac}$ . The  $Re$  is a function of operating frequency and the amplitude provided to the acoustic actuator. Changing the  $Re$  changes the velocity at which the vortices are convected along the jet centerline. With increased amplitude value, the structure of the vortices produced from the synthetic differ [65], thus the force imparted by them.

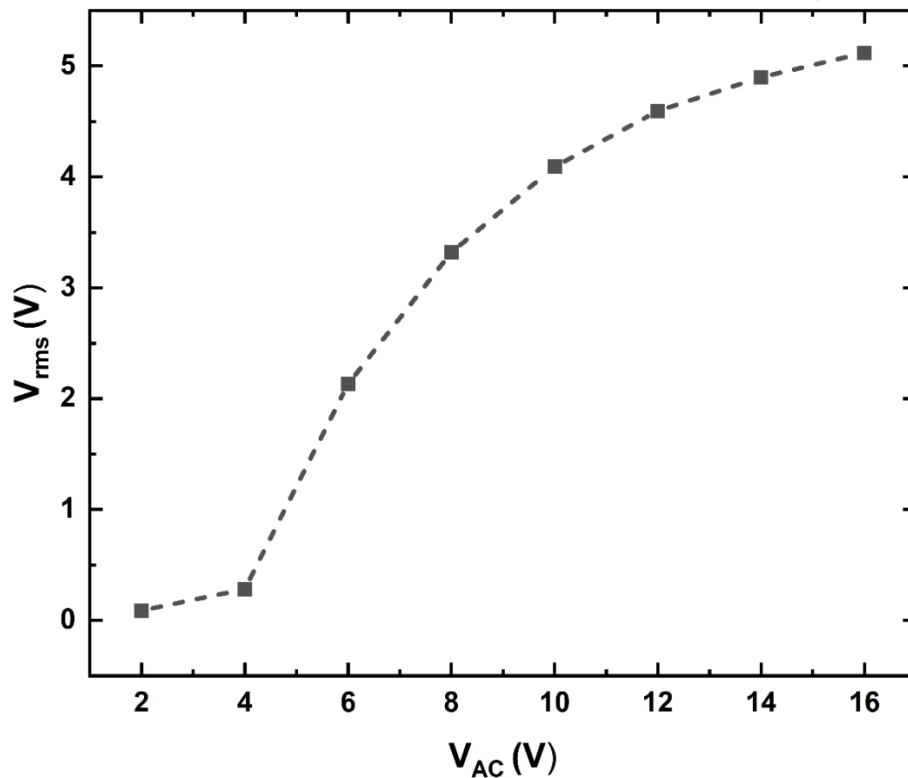


Fig. 4.21: Effect of the input power supplied to the acoustic SJ (amplitude) on the voltage generated by a single piezoelectric flap for  $R3.5$  and  $h/d=1.5$

Fig. 4.22 shows a comparative analysis of voltage, power, and % energy harvesting for different types of strips at all radial locations. If we compare strip widths  $W4$ ,  $W8$ , and  $W12$ , maximum power is obtained by  $W12$ . This is because of its large area in a fluid path due to this higher-pressure force exerted over the strip, and stresses are very high, especially for radial location  $R2$ . Maximum power produced  $195$  mW and  $2.2\%$  energy harvested from a single strip. Voltage develops for the  $W12$  strip and increases with increased  $h/d$  because vertices sufficiently develop and hit the flap, but at lower  $h/d$ , the jet comes from an orifice in the form of a jet nozzle; pressure force is not efficiently distributed. The least power developed from a  $W4$  strip is because of its low area in a fluid path, and power data are very uncertain due to uncertainty in vibration. Similarly, area-wise maximum radial

location R8 produced maximum compared to R5 radial location whereas W8 strip lies between W12 and W4.

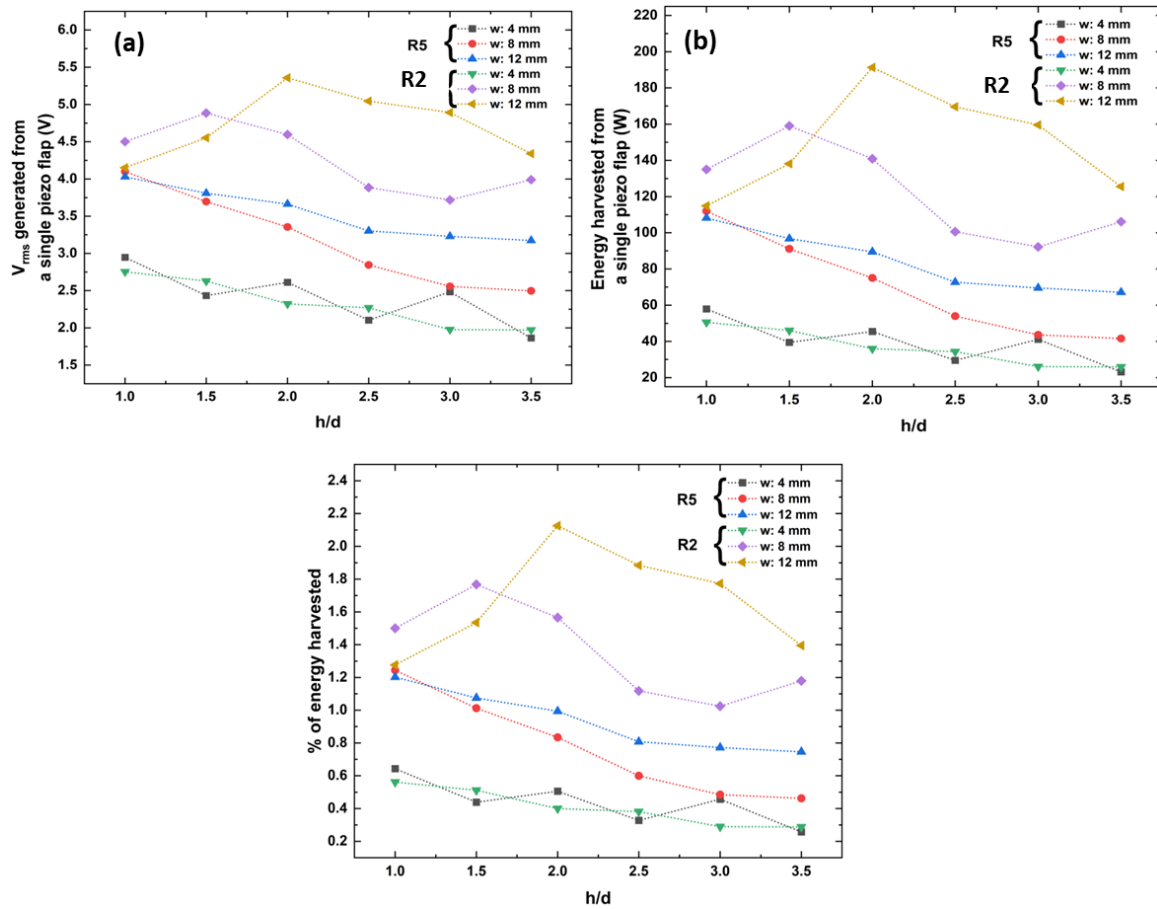


Fig. 4.22: A comparative analysis of voltage, power, and % energy harvested for different types of strips at all radial locations. (a) Variation in  $V_{rms}$  to  $h/d$  for all strips (b) Variation in power to  $h/d$  for all strips (c) Variation in % energy harvesting to  $h/d$  for all strips.

---

## **Conclusions and Scope for Future Work**

---

### **5.1 Conclusions**

An experimental investigation of heat transfer and energy harvesting characteristics for the newly proposed design of the SJ with piezoelectric flaps is carried out. The experiments are conducted for  $Re=13000$ ,  $L=16.2$  at different  $h/d$  and  $z/d$  value combinations. The effect of the power input on the  $V_{rms}$  generated from the piezoelectric flap is studied. The results have shown a significant improvement in heat transfer while harvesting some input energy due to flow-induced vibrations. The following conclusions are drawn from the study.

- SJs with flaps can overcome the reduced heat transfer rates at lower  $z/d$  values. The fluctuating flaps induce higher turbulence levels between the flap and the surface, increasing the convective heat transfer. Also, the minimized recirculation of hot air due to flapping motion aids enhances the heat transfer.
- The maximum improvement over the conventional SJ observed is up to 46% and 22% for spot and wide area cooling, respectively. Optimum enhancements are found when the difference between the  $h/d$  and  $z/d$  values is less than 2.
- The heat transfer performance of the SJ with flaps deteriorates after  $z/d=6$  for the tested  $h/d$  values. It happens due to a combination of two reasons. First, spreading the SJ before the flap reduces the imparted force. Secondly, the presence of flaps restricts the natural momentum of the SJ, and the turbulence induced owing to their flapping motion cannot influence the heated surface at a larger distance.
- With the addition of the piezoelectric (PZT) flaps, we can improve the system's operating efficiency. Up to 195 mW of the power can be harvested from a single piezoelectric flap, corresponding to 2.2% of the input energy to the SJ actuator, which can be harvested at different combinations of  $h/d$  and  $z/d$  values.
- The voltage generated from a single piezoelectric flap increases with an increment in the amplitude ( $V_{ac}$ ) supplied to the SJ actuator. The increment in the  $V_{rms}$  decreases with an equal increase in the supplied voltage.
- Milliwatt power developed by a piezoelectric flap can run different milliwatt-powered sensors like temperature and humidity.

The heat transfer enhancement is evident with the usage of the flaps, as well as the harvested energy from flow-induced fluctuations. The current study presented a

preliminary concept of the design and results. Further investigation is needed to optimize geometrical, material, and fluidic operating conditions, which are currently under investigation.

## 5.2 Scope of future work

This work guides the future scope of energy harvesting from an unsteady cooling jet and using specific mechanisms in a fluid path to increase turbulence intensity in a fluid.

- Different types of flap materials and their effectiveness on the heat transfer and energy harvesting can be studied.
- The aeroelastic energy mechanism can be tested for different orifices shapes and geometries.
- Effect of actuation frequency on the flapping mechanism can be tested at lower orifice-to-plate spacings ( $z/d < 2$ ).
- The shape of the flap can be optimized to improve the heat transfer rates and aeroelastic energy harvesting.
- Application of machine learning techniques to optimize fluidic and geometrical parameters can be done.

## References

---

- [1] W.L. Cheng, N. Liu and W.F. Wu, Studies on thermal properties and thermal control effectiveness of a new shape-stabilized phase change material with high thermal conductivity, *Appl. Therm. Eng.* 36 (2012), pp. 345–352.
- [2] Liu, Qiusheng, Katsuya Fukuda, and Purwono F. Sutopo. "Experimental study on thermosyphon for shipboard high-power electronics cooling system." *Heat transfer engineering* 35.11-12 (2014): 1077-1083.
- [3] Tang, Heng, et al. "Review of applications and developments of ultra-thin micro heat pipes for electronic cooling." *Applied energy* 223 (2018): 383-400.
- [4] Berrouche, Youcef, et al. "Design of a porous electroosmotic pump used in power Electronic cooling." *IEEE transactions on industry applications* 45.6 (2009): 2073-2079.
- [5] Chein, Reiyu, and Guanming Huang. "Thermoelectric cooler application in electronic cooling." *Applied thermal engineering* 24.14-15 (2004): 2207-2217.
- [6] Wu, Ruikang, et al. "Thermal modeling and comparative analysis of jet impingement liquid cooling for high power electronics." *International Journal of Heat and Mass Transfer* 137 (2019): 42-51.
- [7] He, Xin, et al. "Heat transfer characteristics of impinging steady and synthetic jets over vertical flat surface." *International Journal of Heat and Mass Transfer* 80 (2015): 825-834.
- [8] S.G. Mallinson, G. Hong and J.A. Reizes, *Some characteristics of synthetic jets*, 30th Fluid Dyn. Conf. (1999).
- [9] S.G. Mallinson, C.Y. Kwok and J.A. Reizes, *Numerical simulation of micro-fabricated zero mass-flux jet actuators*, *Sensors Actuators, A Phys.* 105 (2003), pp. 229–236.
- [10] S. Mallinson and J. Reizes, *Numerical Simulation of Membrane Forcing Effects On Synthetic Jet Actuator Flows*, 14th Australas. FluidMechanics Conf. (2001), pp. 757–760.
- [11] Yang, Shengke, et al. "Novel hybrid ice protection system combining thermoelectric system and synthetic jet actuator." *AIAA Journal* 59.4 (2021): 1496-1500.
- [12] Zhao, Guoqing, et al. "Experimental investigations for parametric effects of dual synthetic jets on delaying stall of a thick airfoil." *Chinese Journal of Aeronautics* 29.2 (2016): 346-357.

- [13] C. SINGH, D. Manani, K. Mathiyazhagan, P. Sharma and F. Hakkak, Department of Mechanical Engineering, Technology 169 (2010), pp. 178.
- [14] N. Sezer and M. Koç, "A comprehensive review on the state-of-the-art of piezoelectric energy harvesting," *Nano Energy*, vol. 80. Elsevier Ltd, Feb. 01, 2021. doi: 10.1016/j.nanoen.2020.105567.
- [15] Akaydin, H. D., N. Elvin, and Y. Andreopoulos. "The performance of a self-excited fluidic energy harvester." *Smart materials and Structures* 21.2 (2012): 025007.
- [16] Wang D, Chen JS. Progress on the Applications of Piezoelectric Materials in Sensors. *MSF* 2016;848:749–56. <https://doi.org/10.4028/www.scientific.net/msf.848.749>
- [17] Nuffer, Jurgen, and Thilo Bein. "Application of piezoelectric materials in transportation industry." *Global symposium on innovative solutions for the advancement of the transport industry*. Vol. 4. No. 6. 2006.
- [18] C. Peng, M. Chen, H. K. Sim, Y. Zhu and X. Jiang, "Noninvasive and Nonocclusive Blood Pressure Monitoring via a Flexible Piezo-Composite Ultrasonic Sensor," in *IEEE Sensors Journal*, vol. 21, no. 3, pp. 2642-2650, 1 Feb.1, 2021, doi: 10.1109/JSEN.2020.3021923.
- [19] Sirohi, Jayant, and Rohan Mahadik. "Harvesting wind energy using a galloping piezoelectric beam." (2012): 011009.
- [20] Lu, B. et al. Ultra-flexible Piezoelectric Devices Integrated with Heart to Harvest the Biomechanical Energy. *Sci. Rep.* 5, 16065; doi: 10.1038/srep16065 (2015).
- [21] B. L. Smith and A. Glezer, "Vectoring and Small-Scale Motions Effectuated in Free Shear Flows Using Synthetic Jet Actuators," 1997.
- [22] B. L. Smith and A. Glezer, "The formation and evolution of synthetic jets," *Physics Fluids*, vol. 10, no. 9, pp. 2281–2297, 1998, doi: 10.1063/1.869828.
- [23] S. G. Mallinson, J. A. Reizes, and G. Hong, "An experimental and numerical study of synthetic jet flow," 2001
- [24] C. Xu, Y. Long, and J. Wang, "Entrainment mechanism of turbulent synthetic jet flow," *J Fluid Mech*, vol. 958, Mar. 2023, doi: 10.1017/jfm.2023.102.
- [25] B. L. Smith and G. W. Swift, "A comparison between synthetic jets and continuous jets," *Exp Fluids*, vol. 34, no. 4, pp. 467–472, 2003, doi: 10.1007/s00348-002-0577-6.
- [26] A. Pavlova and M. Amitay, "Electronic cooling using synthetic jet impingement," *J Heat Transfer*, vol. 128, no. 9, pp. 897–907, Sep. 2006, doi: 10.1115/1.2241889.

- [27] Gillespie MB, Black WZ, Rinehart C, Glezer A (2006) Local convective heat transfer from a constant heat flux flat plate cooled by synthetic air jets. *J Heat Transfer* 128:990–1000. [https://doi.org/ 10.1115/1.2345423](https://doi.org/10.1115/1.2345423).
- [28] P. Valiorgue, T. Persoons, A. McGuinn, and D. B. Murray, “Heat transfer mechanisms in an impinging synthetic jet for a small jet-to-surface spacing,” *Exp Therm Fluid Sci*, vol. 33, no. 4, pp. 597–603, Apr. 2009, doi: 10.1016/j.expthermflusci.2008.1
- [29] M. Chaudhari, G. Verma, B. Puranik, and A. Agrawal, “Frequency response of a synthetic jet cavity,” *Exp Therm Fluid Sci*, vol. 33, no. 3, pp. 439–448, Mar. 2009, doi: 10.1016/j.expthermflusci.2008.10.008.
- [30] M. Chaudhari, B. Puranik, and A. Agrawal, “Heat transfer characteristics of synthetic jet impingement cooling,” *Int J Heat Mass Transf*, vol. 53, no. 5–6, pp. 1057–1069, Feb.2010, doi: 10.1016/j.ijheatmasstransfer.2009.11.005.
- [31] M. Chaudhari, B. Puranik, and A. Agrawal, “Effect of orifice shape in synthetic jet based impingement cooling,” *Exp Therm Fluid Sci*, vol. 34, no. 2, pp. 246–256, Feb. 2010, doi: 10.1016/j.expthermflusci.2009.11.001.
- [32] P. Gil, J. Wilk, R. Smusz, and R. Gałek, “Centerline heat transfer coefficient distributions of synthetic jets impingement cooling,” *Int J Heat Mass Transf*, vol. 160, Oct. 2020, doi: 10.1016/j.ijheatmasstransfer.2020.120147.
- [33] Mangate, Laxmikant D., and Mangesh B. Chaudhari. "Heat transfer and acoustic study of impinging synthetic jet using diamond and oval shape orifice." *International Journal of Thermal Sciences* 89 (2015): 100-109.
- [34] M. Chaudhari, B. Puranik, and A. Agrawal, “Multiple orifice synthetic jet for improvement in impingement heat transfer,” *Int J Heat Mass Transf*, vol. 54, no. 9–10, pp. 2056–2065, Apr. 2011, doi: 10.1016/j.ijheatmasstransfer.2010.12.023.
- [35] L. Mangate, H. Yadav, A. Agrawal, and M. Chaudhari, “Experimental investigation on thermal and flow characteristics of synthetic jet with multiple-orifice of different shapes,” *International Journal of Thermal Sciences*, vol. 140, pp. 344–357, Jun. 2019, doi: 10.1016/j.ijthermalsci.2019.02.036.
- [36] P. K. Singh, A. K. Shah, S. N. Tripathi, H. Yadav, P. K. Upadhyay, and S. K. Sahu, “Numerical investigation of the flow and thermal behavior of impinging single and multi-orifice synthetic jets with different waveforms,” *Numeri Heat Transf A Appl*, vol. 83, no. 6, pp. 573–593, 2022, doi: 10.1080/10407782.2022.2101808.

- [37] P. Gil, "Flow and heat transfer characteristics of single and multiple synthetic jets impingement cooling," *Int J Heat Mass Transf*, vol. 201, Feb. 2023, doi: 10.1016/j.ijheatmasstransfer.2022.123590.
- [38] H. Yadav, A. Joshi, M. Chaudhari, and A. Agrawal, "An experimental study of a multi-orifice synthetic jet with application to cooling of compact devices," *AIP Adv*, vol. 9, no. 12, Dec. 2019, doi: 10.1063/1.5128776.
- [39] U. S. Bhapkar, A. Srivastava, and A. Agrawal, "Acoustic and heat transfer characteristics of an impinging elliptical synthetic jet generated by acoustic actuator," *Int J Heat Mass Transf*, vol. 79, pp. 12–23, 2014, doi: 10.1016/j.ijheatmasstransfer.2014.07.083.
- [40] A. Ahmed and Z. A. Bangash, "Experimental investigation of axisymmetric coaxial synthetic jets," *Exp Therm Fluid Sci*, vol. 33, no. 8, pp. 1142–1148, Nov. 2009, doi: 10.1016/j.expthermflusci.2009.07.003.
- [41] B. Zhang, H. Liu, Y. Li, H. Liu, and J. Dong, "Experimental study of coaxial jets mixing enhancement using synthetic jets," *Applied Sciences (Switzerland)*, vol. 11, no. 2, pp. 1–13, Jan. 2021, doi: 10.3390/app11020803.
- [42] S. Panda, T. B. Gohil, and V. Arumuru, "Evolution of flow structure from a coaxial synthetic jet," *Int J Mech Sci*, vol. 231, Oct. 2022, doi: 10.1016/j.ijmecsci.2022.107588.
- [43] H. Elahi, M. Eugeni, and P. Gaudenzi, "A review on mechanisms for piezoelectric-based energy harvesters," *Energies*, vol. 11, no. 7. MDPI AG, 2018. doi: 10.3390/en11071850.
- [44] F. Petrini and K. Gkoumas, "Piezoelectric energy harvesting from vortex shedding and galloping induced vibrations inside HVAC ducts," *Energy Build*, vol. 158, pp. 371–383, Jan. 2018, doi: 10.1016/j.enbuild.2017.09.099.
- [45] Xie, X. D., Q. Wang, and N. Wu. "Potential of a piezoelectric energy harvester from sea waves." *Journal of Sound and Vibration* 333.5 (2014): 1421-1429.
- [46] Hobbs, William B., and David L. Hu. "Tree-inspired piezoelectric energy harvesting." *Journal of fluids and Structures* 28 (2012): 103-114.
- [47] D. A. Wang and H. H. Ko, "Piezoelectric energy harvesting from flow-induced vibration," *Journal of Micromechanics and Microengineering*, vol. 20, no. 2, 2010, doi: 10.1088/0960-1317/20/2/025019.
- [48] H. D. Akaydin, N. Elvin, and Y. Andreopoulos, "Energy harvesting from highly unsteady fluid flows using piezoelectric materials," in *Journal of Intelligent Material Systems and Structures*, Sep. 2010, pp. 1263–1278. doi: 10.1177/1045389X10366317.

- [49] D. Vatansever, R. L. Hadimani, T. Shah, and E. Siores, “An investigation of energy harvesting from renewable sources with PVDF and PZT,” *Smart Mater Struct*, vol. 20, no. 5, May 2011, doi: 10.1088/0964-1726/20/5/055019.
- [50] J. Sirohi and R. Mahadik, “Piezoelectric wind energy harvester for low-power sensors,” *J Intell Mater Syst Struct*, vol. 22, no. 18, pp. 2215–2228, Dec. 2011, doi: 10.1177/1045389X11428366.
- [51] H. Zou, H. Chen, and X. Zhu, “Piezoelectric energy harvesting from vibrations induced by jet-resonator system,” *Mechatronics*, vol. 26, pp. 29–35, Mar. 2015, doi: 10.1016/j.mechatronics.2015.01.002.
- [52] H. Arionfard and Y. Nishi, “Experimental investigation of a drag assisted vortex-induced vibration energy converter,” *J Fluids Struct*, vol. 68, pp. 48–57, Jan. 2017, doi: 10.1016/j.jfluidstructs.2016.10.002.
- [53] Y. Huang et al., “Aeroacoustics-driven jet-stream wind energy harvester induced by jet-edge-resonator,” *Nano Energy*, vol. 89, Nov. 2021, doi: 10.1016/j.nanoen.2021.106441.
- [54] H. Liu, J. Zhong, C. Lee, S. W. Lee, and L. Lin, “A comprehensive review on piezoelectric energy harvesting technology: Materials, mechanisms, and applications,” *Applied Physics Reviews*, vol. 5, no. 4. American Institute of Physics Inc., Dec. 01, 2018. doi: 10.1063/1.5074184.
- [55] Z. Yang, S. Zhou, J. Zu, and D. Inman, “High-Performance Piezoelectric Energy Harvesters and Their Applications,” *Joule*, vol. 2, no. 4. Cell Press, pp. 642–697, Apr. 18, 2018. doi: 10.1016/j.joule.2018.03.011.
- [56] S. Sadikbasha, B. Radhika, and V. Pandurangan, “Auxetic hexachiral cantilever beams for piezoelectric vibration energy harvesting,” *Smart Mater Struct*, vol. 31, no. 10, Oct. 2022, doi: 10.1088/1361-665X/ac8d3e.
- [57] C. S. Greco, G. Paolillo, A. Ianiro, G. Cardone, and L. de Luca, “Effects of the stroke length and nozzle-to-plate distance on synthetic jet impingement heat transfer,” *Int J Heat Mass Transf*, vol. 117, pp. 1019–1031, Feb. 2018, doi: 10.1016/j.ijheatmasstransfer.2017.09.118.
- [58] P. Sharma, S. K. Sahu, and H. Yadav, “Experimental investigation of flow and thermal characteristics of synthetic jet issuing from sharp-edged orifices,” *Experimental Heat Transfer*, 2022, doi: 10.1080/08916152.2022.2105449.

- [59] P. Sharma, S. K. Sahu, and H. Yadav, "The flow and heat transfer behavior of synthetic jets with star shaped orifice of different lobes," *International Journal of Thermal Sciences*, vol. 193, Nov. 2023, doi: 10.1016/j.ijthermalsci.2023.108523.
- [60] J. Lee and S. J. Lee, "Stagnation region heat transfer of a turbulent axisymmetric jet impingement," *Experimental Heat Transfer*, vol. 12, no. 2, pp. 137–156, 1999, doi: 10.1080/089161599269753.
- [61] P. Gil and J. Wilk, "Heat transfer coefficients during the impingement cooling with the use of synthetic jet," *International Journal of Thermal Sciences*, vol. 147, Jan. 2020, doi: 10.1016/j.ijthermalsci.2019.106132.
- [62] P. K. Singh, M. Renganathan, H. Yadav, S. K. Sahu, P. K. Upadhyay, and A. Agrawal, "An experimental investigation of the flow-field and thermal characteristics of synthetic jet impingement with different waveforms," *Int J Heat Mass Transf*, vol. 187, May 2022, doi: 10.1016/j.ijheatmasstransfer.2022.122534.
- [63] Glezer, Ari, and Michael Amitay. "Synthetic jets." *Annual review of fluid mechanics* 34.1 (2002): 503-529.
- [64] C. S. Greco, A. Ianiro, T. Astarita, and G. Cardone, "On the near field of single and twin circular synthetic air jets," *Int J Heat Fluid Flow*, vol. 44, pp. 41–52, Dec. 2013, doi: 10.1016/j.ijheatfluidflow.2013.03.018.
- [65] Z. Trávníček, Z. Broučková, J. Kordík, and T. Vít, "Visualization of synthetic jet formation in air," *J Vis (Tokyo)*, vol. 18, no. 4, pp. 595–609, Nov. 2015, doi: 10.1007/s12650-015-0273-2.